NTNU – Trondheim
Norwegian University of
Science and Technology

Wave Conditions for Offshore Wind Turbine Foundations in Intermediate Water Depths

Espen André Engebretsen

Marine Technology
Submission date: June 2012
Supervisor: Dag Myrhaug, IMT
Co-supervisor: Sverre K Haver, IMT

Norwegian University of Science and Technology
Department of Marine Technology

Abstract

In this thesis, the effects on regular waves when propagating from deep to shallow water have been investigated, assuming linear wave theory. The effects of shoaling, refraction, reflection and diffraction have been studied. The process and types of breaking waves has also been reviewed.

Linear wave theory, second and higher order Stokes theory, Stream function theory, Solitary wave theory and Cnoidal theory have been reviewed. The relative validity of the different wave theories was also assessed.

The effects on the wave spectrum as a sea state travels from deep to shallow water, described by the energy balance equation, has also been addressed. The effects addressed were wind, nonlinear wave-wave interactions, white-capping, bottom friction and surf-breaking. Two computer models for numerically solving the energy balance equation was mentioned, being SWAN and STWAVE, where SWAN was chosen for use in the analyses.

The NORA10 hindcast was believed not to properly take the change in water depth into account at the Dogger Bank Zone. At a point north of the location of interest, the water depth was of such a magnitude (81m) that the NORA10 hindcast was believed to yield credible data for the significant wave height and spectral peak period. A long term estimate of the 50 year significant wave height was performed from the NORA10 data at the point north of the Dogger Bank Zone, by the environmental contour method. This resulted in an estimated 50 year significant wave height of 11.74m and spectral peak period of 15.68s.

The SWAN model was used on a test case from Svangstu (2011) to get familiar with the program, and investigate how the different physical effects influence the solution. With the knowledge acquired from the test case, the Dogger Bank case was analyzed in SWAN, to obtain the 50 year sea state parameters at the location of interest. The 50 year sea state north of the Dogger Bank Zone, the Dogger Bank bathymetry, as well as a constant wind of 23.3 m/s was used as input. The 50 year sea state at the location of interest was found to be characterized by a significant wave height of 7.34m and a spectral peak period of 15.56s. SWAN was found to result in a significant wave height of some 15-27% lower than what was found in NORA10.

By performing a short term analysis on the 50-year sea state at the location of interest, the 50-year design wave height was found to be 12.5m, assuming the individual wave heights to be modeled by the Gluhovski distribution. The 90% confidence interval of the design wave period was found to be $9.6s \leqslant T \leqslant 16.3s$. This was estimated from studying the ratio between the period of the three largest waves in a time series, and the spectral peak period of the sea state in 95 time series from Svangstu (2011). By evaluating only the limiting values of the period range, the longest and shortest design wave was found to be 80% and 97.4% of the breaking wave height respectively, assuming linear theory.

The wind turbine structure geometry was simplified to be modeled by a cylinder with a diameter of 6m. By computing the kinematics from the Stream Function theory, the maximum base shear and overturning moment using Morisons equation was found to be 3.67MN and 65.93MN respectively. The effects of the rate of change of added mass momentum was also assessed.

From a simplified and conservative approach, the impact loads from a breaking wave was estimated. This resulted in a base shear and overturning moment of such a magnitude that en extensive analysis is recommended on this topic in the future.

Preface

This Master Thesis has been written during the spring semester at the Norwegian University of Science and Technology 2012. The thesis has been submitted to partially fulfill the requirement for completing the degree of Master of Science, and have been performed at the Department of Marine Technology in Trondheim, Norway.

The process of writing this thesis have been challenging and academically rewarding. The most challenging aspects of writing this thesis have been related to the programming and troubleshooting of the numerous Matlab scripts written for use in the analyzes. Understanding some aspects of the results obtained using Swan in addition to obtain good results of loads from wave slamming have also been quite time demanding. Despite the hard work required to finish this thesis, I am truly grateful for my choice of topic.

Acknowledgments

I would like to take this opportunity to thank the people who have helped me through the process of writing this thesis.

Through my summer internship with Dr. techn. Olav Olsen in the summer of 2011, Dagfinn Sveen and Håkon S. Andersen guided, motivated and inspired me to pursuit further studies and knowledge of the topics related to estimating wave loads on fixed offshore wind turbine foundations. I am truly grateful for their contributions.

As my initial knowledge on establishing design wave parameters in finite water depth was scarce, I would have faced a massive challenge without the help and guidance provided by Prof. Sverre Haver (Statoil and NTNU). He has been a *truly* dedicated advisor, and there has been no limit to his helpfulness. Be it morning or evening, Monday or Sunday, or even a national holiday, Sverre has responded to my inquiries over email. His extensive knowledge on the topics of this thesis has been of tremendous value to me.

Last, but not least, I wish to thank my supervisor Prof. Dag Myrhaug for his time, help and assistance through this spring semester. In addition to assisting me through the work of this thesis, he has also lectured the course TMR4230 OCEANOGRAPHY, which I have attended parallel with writing the thesis. He is an inspirational lecturer and professor, and the course has contributed to a significant part of the theory applied in this thesis.

Espen Engebretsen

Espen Engebretsen, Trondheim, 9th Jun, 2012

Scope of Work

NTNU Trondheim
Norwegian University of Science and Technology
Department of Marine Technology

MASTER THESIS IN MARINE TECHNOLOGY

SPRING 2012

FOR

STUD.TECHN. ESPEN ENGEBRETSEN

WAVE CONDITIONS FOR OFFSHORE WIND TURBINE FOUNDATIONS IN INTERMEDIATE WATER DEPTHS

Offshore wind energy appears to be promising for alternative energy. The design of appropriate structures for mounting the foundation of wind turbines is a challenge for the engineering community, particularly for offshore locations. Different foundation options have been used, such as gravity base structures, monopiles, suction piles, jacket structures and multi-leg foundations (tripod/quadruped structures). It is essential to make reliable assessments of the wave and current loads on the structure. Offshore wind turbines are mounted in shallow and intermediate water depths and therefore it is crucial to apply an appropriate wave theory for making reliable assessments of the wave forces on the structure.

The purpose of this this thesis is to study the wave conditions in intermediate water depths from given wave conditions in deep water.

The student shall:

1. Give a review of wave theories in shallow and intermediate water depths with emphasis on the statistical description of the waves.

2. Transform the storm wave conditions from deep water to intermediate water depth using a third generation wave model.

3. Compare the results with:
   (i) The model tests by Svangstu (2011)
   (ii) The hindcast wave data from the Norwegian Meteorological Institute (NORA 10).

4. Calculate the forces on a monopile and compare the results by using different wave theories.
   If the time permits the loads from breaking waves shall also be considered.

In the thesis the candidate shall present his personal contribution to the resolution of problem within the scope of the thesis work.

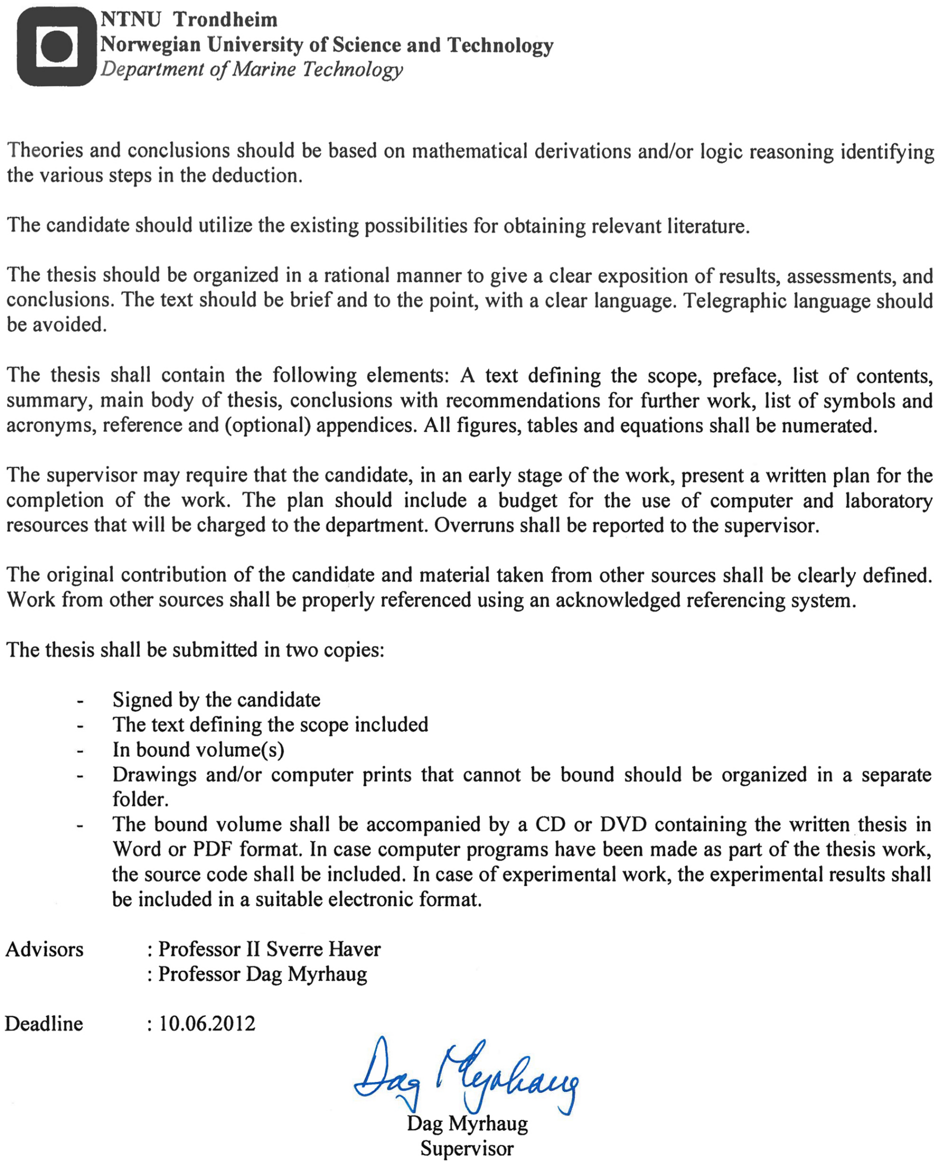

NTNU Trondheim
Norwegian University of Science and Technology
Department of Marine Technology

Theories and conclusions should be based on mathematical derivations and/or logic reasoning identifying the various steps in the deduction.

The candidate should utilize the existing possibilities for obtaining relevant literature.

The thesis should be organized in a rational manner to give a clear exposition of results, assessments, and conclusions. The text should be brief and to the point, with a clear language. Telegraphic language should be avoided.

The thesis shall contain the following elements: A text defining the scope, preface, list of contents, summary, main body of thesis, conclusions with recommendations for further work, list of symbols and acronyms, reference and (optional) appendices. All figures, tables and equations shall be numerated.

The supervisor may require that the candidate, in an early stage of the work, present a written plan for the completion of the work. The plan should include a budget for the use of computer and laboratory resources that will be charged to the department. Overruns shall be reported to the supervisor.

The original contribution of the candidate and material taken from other sources shall be clearly defined. Work from other sources shall be properly referenced using an acknowledged referencing system.

The thesis shall be submitted in two copies:

- Signed by the candidate
- The text defining the scope included
- In bound volume(s)
- Drawings and/or computer prints that cannot be bound should be organized in a separate folder.
- The bound volume shall be accompanied by a CD or DVD containing the written thesis in Word or PDF format. In case computer programs have been made as part of the thesis work, the source code shall be included. In case of experimental work, the experimental results shall be included in a suitable electronic format.

Advisors : Professor II Sverre Haver
: Professor Dag Myrhaug

Deadline : 10.06.2012

Dag Myrhaug

Dag Myrhaug
Supervisor

Contents

List of Figures

List of Tables

List of Symbols

Latin characters

a_1	Undisturbed horizontal fluid particle acceleration
d	Water depth
c	Constant **or** wave crest height
c_w	Phase velocity
c_g	Group velocity
f	Frequency
$f(x)$	Probability density function of stochastic variable x
g	Acceleration of gravity
h_0	Threshold level in POT method
h_1, h_2	Battjes and Groenendisjk parameters
h_T	Transition height
k	Wave number
m	Number of years
m_0	Zeroth spectral moment
m_2	Second spectral moment
n	Denoting number **or** spreading coefficient
$\vec{r}$	Horizontal plane position vector
s	Wave steepness **or** submergence of cylinder strip
t	Time
u	Undisturbed horizontal fluid particle velocity
u_1, u_2	Variables in standard normalized u-space
$\bar{x}$	Mean of variable x
$\hat{x}$	Estimated value of x
A^{2D}	High frequency limit of the added mass for a 2D cylindrical section
C_D	Drag coefficient
C_M	Mass coefficient
C_S	Slamming coefficient
D	Duration of sea state **or** diameter
$D(\theta)$	Directionality function
E	Energy
$E[x]$	Expected value of stochastic variable x
$F(x)$	Cumulative probability distribution function of stochastic variable x
$F(z,t)$	Horizontal force
H	Wave height
H_{m0}	Significant wave height obtained from spectrum
H_s	Significant wave height obtained from time series
I	Load impulse
K_{sh}	Shoaling coefficient
L	Wave length
$M(t)$	Overturning moment
N	Number of zero crossings

N_m	Number of sea states
P	Energy flux
P_0	Load amplitude
S_y	Standard deviation of variable y
S	Horizontal drift of water particle during one cycle
$S(\omega)$	Wave spectral density
T	Period
T_{3max}	Period of one of the three largest waves in a time series
T_{m02}	Spectral estimate of zero crossing period
T_n	Natural period
T_p	Spectral peak period
T_z	Mean zero crossing period
U_r	Ursell number
V	Velocity

Greek characters

α	Crest angle **or** bottom slope **or** Weibull parameter
α_H	Bandwidth parameter
β	Radius of contour constant probability of return in the U-space **or** slope **or** Weibull parameter
ϕ	Velocity potential
γ	Non-dimensional peak shape parameter
η_b	Breaking crest height
θ	Angle
ρ	Density **or** bandwidth parameter **or** Weibull parameter
ξ	Iribarren number
λ	Wave length **or** curling factor **or** Exponential distribution parameter
μ	Lognormal distribution parameter
σ	Lognormal distribution parameter **or** spectral width parameter
ω	Wave frequency
ξ	Iribarren number
ψ	Phase function **or** stream function
ζ	Wave elevation above mean free surface
ζ_a	Wave amplitude
ζ_c	Wave crest elevation
ζ_t	Wave trough depth
∇	Gradient

Φ	Standard normal cumulative distribution function
Γ	Gamma function
Ω	Source term in the energy balance equation

List of Abbreviations

CV	Coefficient of Variance
DFSBC	Dynamic Free Surface Boundary Condition
DAF	Dynamic Amplification Factor
DLF	Dynamic Load Factor
JONSWAP	Joint North Sea Wave Project
KFSBC	Kinematic Free Surface Boundary Condition
MOM	Method of Moments
NTNU	Norges Tekniske Naturvitenskapelige Universitet
POT	Peak Over Threshold
Std	Standard deviation
STWAVE	Steady State Spectral Wave
Var	Variance
Q-Q	Quantile-Quantile

1. Introduction

For offshore wind turbines, avoiding over-conservative design methods is of *great importance*, due to economic considerations. This call for complex and accurate analyzes and requires well documented input parameters. It is particularly complicated to calculate realistic wave loads for finite and shallow water areas, due to the sea bottom's effect on the incident waves. In general, this leads to increased loads compared to what is obtained using linear wave theory. The extreme load is characterized by the maximum overturning moment and may be calculated by different methods, where one of these methods is the design wave method.

In view of developing offshore wind farms with hundreds of similar wind turbine foundations, it is expected to be of considerable interest to develop analysis methods which estimates realistic extreme values for the foundation overturning moment.

The aim of this thesis is initially to discuss the effects of finite water depth on regular linear waves and wave spectrum, give a review of possible wave theories in shallow and intermediate water depth, to investigate the statistical description of waves in finite water depth and how to establish a 50 year design wave at a location in the Dogger Bank Zone. Furthermore, this thesis aims to make simplified calculations of the loads resulted by the 50 year design wave and from a breaking wave.

This thesis seek to answer all aspects of the scope of work, the only deviation has been in relation to calculating the forces on a monopile from *different* wave theories. As the design waves were found to be best described by the Stream Function theory, the kinematics were only calculated from this theory. Comparing with the results obtained from e.g. WAJAC for linear and Stokes fifth order theory is trivial, and therefore omitted to focus the available time on other topics.

The first 6 chapters of this thesis forms the basis of the theory applied in analyzes presented in the succeeding chapters. If new theory is applied in the analyzes presented after chapter 6, it will first be presented before results and discussion follows successively.

All figures and material presented in this thesis which has *not* been referenced to other sources, has been produced by the author. In the making of this thesis, the following software versions have been utilized

- MATLAB version R2012a
- WAJAC V6.2-01
- FOURIER as of 24 May 2012
- ENGAUGE DIGITIZER version 4.1

2. Finite Water Depth Effects on Linear Waves

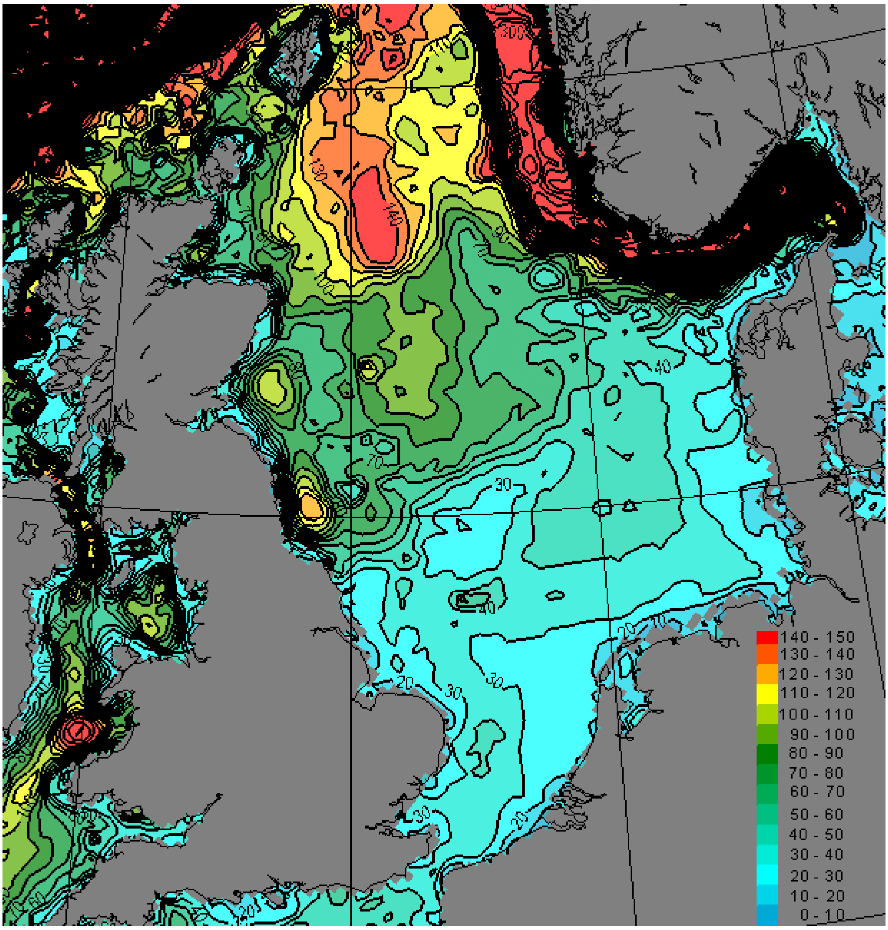

Figure 2.1: Bathymetry in the southern part of the North Sea from the WAM 10 model, Reistad (2011)

The area proposed for the offshore wind turbines described in this report, the Dogger Bank Zone, is in a water depth from 15m-40m. The area north of the Dogger Bank Zone is of relatively deep water, and design wave conditions at the wind turbine positions are likely to originate from here, Haver (2011a). This means that the storm condition in relatively deep water is propagating towards shallower water, where bottom induced effects will be significantly larger than where it originated from.

In the following, the effects on regular wave characteristics when propagating from deep to shallow water will be discussed. The derivations will be based on linear wave theory in finite water depth, assuming that linear theory is valid over the entire depth range.

2.1 Shoaling

Shoaling is the variation of waves in their direction of propagation due to depth-induced changes of the group velocity in that direction, Holthuijsen (2007). In this section the effects on the waves due to shoaling will be discussed, and a *normal* wave incidence to a coast with depth contours parallel to the coastline is assumed. The depth variation is assumed to be so slow that the local water depth can be assumed constant, Svendsen (2006).

A wave train can be represented by the following equation, Myrhaug (2006):

$$\zeta(x, y, t) = \zeta_A(x, y) \cos \psi(x, y, t) \tag{2.1}$$

where ψ is the phase function given by

$$\psi(x, y, t) = \vec{k} \cdot \vec{r} - \omega t \tag{2.2}$$

In **Equation 2.2**, $\vec{k}$ is the local wave number vector given by $\vec{k}(x, y) = k_x\vec{i} + k_y\vec{j}$, and $\vec{r}$ is the horizontal plane position vector given by $\vec{r} = x\vec{i} + y\vec{j}$ which yields:

$$\psi(x, y, t) = \vec{k}_x x + \vec{k}_y y - \omega t \tag{2.3}$$

As ψ is a continuous function, the order of differentiation does not matter (*Clairaut's theorem*) which results in the following relationship:

$$\frac{\delta\left(\nabla\psi\right)}{\delta t} = \nabla\left(\frac{\delta\psi}{\delta t}\right) \tag{2.4}$$

where ∇ is given by $\nabla = \frac{\delta}{\delta x}\vec{i} + \frac{\delta}{\delta y}\vec{j}$.

By combining **Equation 2.3** and **Equation 2.4** we get the following relationship

$$\frac{\delta\vec{k}}{\delta t} = -\nabla\omega \tag{2.5}$$

Equation 2.5 can be considered an equation for *conservation of wave crests*, and states that any temporal change in the wave number vector $\vec{k}$ must be balanced by a spatial change in the wave frequency ω. As the wave field is considered constant in time, the equation reduces to $\nabla\omega = 0$, and thus $\omega = \mathit{constant}$. This means that the wave period is constant in space, even as water depth is changing.

2.1.1 Wave length

A consequence of a constant wave frequency when waves are propagation towards shallower water can be seen from the dispersion relation in arbitrary water depth:

$$\omega^2 = gk \tanh(kd) \tag{2.6}$$

Because $\tanh(kd)$ evolves as indicated in **Figure 2.2**, the wave number must increase when the water depth d decreases to keep the wave frequency constant. The wave length is given by $\lambda = \frac{2\pi}{k}$, which means that the wave length will decrease as the wave number increase. This results in a decreased wave length as the wave propagates over decreasing water depth.

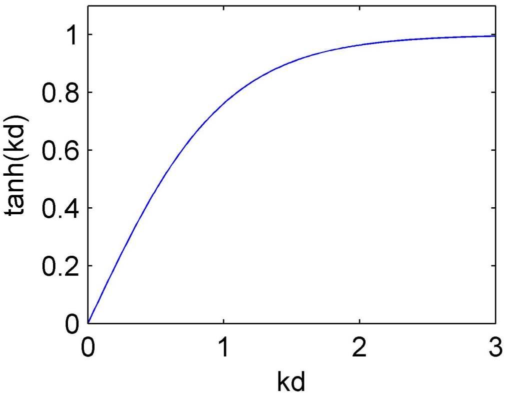

Figure 2.2: Plot of $\tanh(kd)$

2.1.2 Phase velocity and group velocity

The phase velocity is expressed by

$$c_w = \frac{\lambda}{T} = \frac{\omega}{k} \tag{2.7}$$

and because the wave number increases while the frequency is constant, the phase velocity is decreasing with decreasing water depth. This expression shows that, in general, the phase speed depends on the wave number and therefore on the frequency: long waves (small k) travel faster than short waves (large k). Such waves, where the propagation speed depends on wave length or frequency, are called *dispersive waves*, Holthuijsen (2007).

Equation 2.7 can in arbitrary water depth be expressed as

$$c_w = \sqrt{\frac{g}{k}\tanh(kd)} \tag{2.8}$$

which for shallow water ($kd \rightarrow 0, \tanh(kd) \rightarrow kd$) reduces to $c_{w,shallow} = \sqrt{gd}$. From this it is seen that waves in *shallow* water are *non-dispersive*, as the phase velocity does not depend on neither frequency nor wave length.

It is important to differ between the phase speed of a wave profile and the speed of the fluid particles of the wave. The particle velocity is determined from differentiation of the velocity potential or stream function, and is seen to be much less than the phase speed, Haver (2011a).

When harmonic waves with slightly different frequencies are traveling in the same direction, they will reinforce each other at one moment (when *in phase*), and cancel each other out at another moment (when 180° *out of phase*). This will typically be the case for a real ocean surface, a series of rather large amplitude waves followed by a series of rather small amplitude waves will be observed. This grouping of large and small waves is called *wave groups*, as illustrated in **Figure 2.3**.

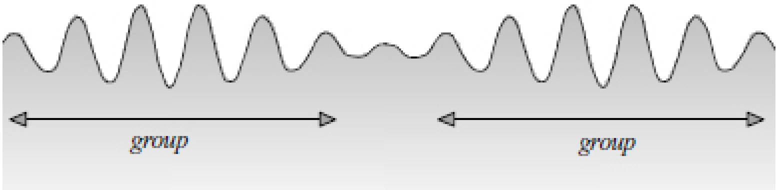

Figure 2.3: Illustration of wave groups, Holthuijsen (2007)

A surface elevation, as shown in the above figure, can be modeled by superposition of two harmonic waves which are slightly out of phase:

$$\zeta = \zeta_1 + \zeta_2 = a\sin(\omega_1 t - k_1 x) + a\sin(\omega_2 t - k_2 x) \tag{2.9}$$

By rearranging the terms, **Equation 2.9** can be expressed as

$$\begin{aligned}\zeta = 2a\cos\left(\frac{\omega_1-\omega_2}{2}t - \frac{k_1-k_2}{2}x\right)\cdot ...\\ \sin\left(\frac{\omega_1+\omega_2}{2}t - \frac{k_1+k_2}{2}x\right)\end{aligned} \tag{2.10}$$

where the sine wave is the carrier wave, and the cosine wave is the envelope of the waves which modulates the amplitude of the carrier wave, Holthuijsen (2007).

The maximum energy appears when the cosine term equals 1, which is when

$$\frac{\omega_1-\omega_2}{2}t - \frac{k_1-k_2}{2}x = 2n\pi \tag{2.11}$$

The position of maximum energy, denoted by $\tilde{x}$, can then be expressed as

$$\tilde{x} = \frac{4n\pi}{k_1-k_2} + \frac{\omega_1-\omega_2}{k_1-k_2}t \tag{2.12}$$

The forward speed of $\tilde{x}$, the *group velocity*, is then given by

$$c_g = \frac{d\tilde{x}}{dt} = \frac{\omega_1-\omega_2}{k_1-k_2} \rightarrow \frac{d\omega}{dk} \text{ as } \omega_1 \rightarrow \omega_2 \tag{2.13}$$

In arbitrary water depth, this results in

$$\begin{aligned} c_g &= \frac{d}{dk}\left[\sqrt{kg\tanh(kd)}\right] \\ &= \left[\frac{2kd}{\sinh(2kd)}+1\right]\frac{g}{2\omega}\tanh(kd) \\ &= \left[\frac{2kd}{\sinh(2kd)}+1\right]\frac{1}{2}\frac{\omega}{k} \end{aligned} \tag{2.14}$$

By combining **Equation 2.14 and 2.7**, a relation between the phase velocity and group velocity in arbitrary water depth can be derived. This relation is expressed as $c_g = nc_w$, where n is given by

$$n = \frac{1}{2}\left[\frac{2kd}{\sinh(2kd)}+1\right] \tag{2.15}$$

By using L'Hôpital's rule, we can see that in deep water:

$$\lim_{kd\to\infty}\frac{2kd}{\sinh(2kd)}\overset{L'H}{=}\lim_{kd\to\infty}\frac{1}{\cosh(2kd)}=0 \tag{2.16}$$

and in shallow water

$$\lim_{kd\to 0}\frac{2kd}{\sinh(2kd)}\overset{L'H}{=}\lim_{kd\to 0}\frac{1}{\cosh(2kd)}=1 \tag{2.17}$$

which results in $c_{g,0} = \frac{1}{2}c_{w,0}$ in deep water, and $c_{g,shallow} = c_{w,shallow}$ as the water depth approaches zero.

2.1.3 Wave Energy and Wave Amplitude

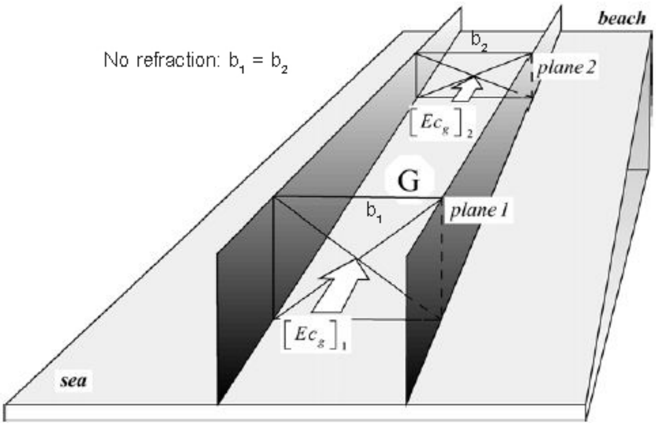

Figure 2.4: Wave energy propagating towards shore, Holthuijsen (2007)

By considering the wave propagating towards shallower water with a straight coastline (i.e. parallel bottom contours) at normal incidence (i.e. perpendicular to the coastline), there will be no variations along the wave crest and refraction will be absent.

The volume G is defined by two vertical sides parallel to the wave direction, two vertical planes normal to the wave direction (one on the seaward side and the other on the beachward side, see **Figure 2.4**), the sea bottom and the mean water surface. By assuming no energy generation (wind) and no energy dissipation (wave breaking, bottom friction, turbulence), no energy enters through the mean water surface nor the sea bottom. In addition, we know that the energy is carried by the group velocity, which is directed parallel to the wave propagation, thus no energy is carried through the lateral sides. So with these assumptions the energy flux through *plane 1* must be equal to the energy flux through *plane 2*, see **Figure 2.4**.

The time averaged, total wave induced energy (potential plus kinetic) per unit horizontal area E is given by

$$E = \frac{1}{2}\rho g \zeta_a^2 \tag{2.18}$$

The energy flux per unit time *per unit crest length* is given by

$$P = Ec_g \tag{2.19}$$

As stated above, the energy flux through plane 1 should be the same as through plane 2, or

$$E_1 c_{g1} b_1 = E_2 c_{g2} b_2 \tag{2.20}$$

In absence of refraction ($b_1 = b_2 = b$) and by combining **Equation 2.18 and 2.20**, the wave amplitude above plane 2 can be expressed as

$$\zeta_{a2} = \zeta_{a1}\sqrt{\frac{c_{g1}}{c_{g2}}} \tag{2.21}$$

By moving plane 1 out in deep water (index 1 renamed 0), the *Shoaling coefficient* K_{sh} describes the ratio between the wave amplitude in deep water and at a location closer to the shore

$$\frac{\zeta_a}{\zeta_{a0}} = K_{sh} = \sqrt{\frac{c_{g0}}{c_g}} \tag{2.22}$$

The shoaling coefficient can, as derived in **Appendix A**, be expressed as a function of *normalized water depth kd*

$$K_{sh} = \left(\left[\frac{2kd}{\sinh(2kd)} + 1\right]\tanh(kd)\right)^{-0.5} \tag{2.23}$$

The shoaling coefficient is plotted as function of (decreasing) normalized water depth kd in **Figure 2.5**. The following phenomena can be observed from the plot:

- The shoaling coefficient, and thus the wave amplitude, will start to decrease as the wave "feels" the presence of the sea bed
- For $kd < 0.639$ (analyzed in MATLAB) the wave amplitude increases towards infinity, which clearly is unphysical, and obviously questions the validity of linear wave theory when the water depth gets very small.
- The effect of shoaling on the group velocity is implicitly described in the plot, because $\frac{c_g}{c_{g0}} = \frac{1}{K_{sh}^2}$. We then see that group velocity start to increase as the wave "feels" the presence of the sea bed, and then decreases towards zero.

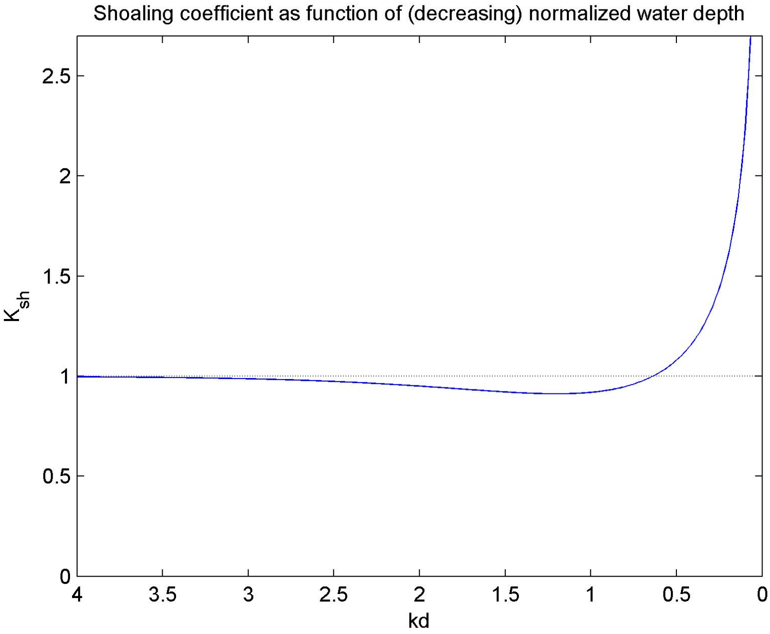

Figure 2.5: Plot of shoaling coefficient as a function of normalized water depth kd, where k is the wave number from linear theory (arbitrary depth)

As the group velocity is decreased, the velocity of the wave energy is decreased, resulting in an *accumulation* of energy. This energy accumulation is what leads to an increased wave amplitude. Wave breaking will limit the wave amplitude growth in real life.

It has now been shown that, with the mentioned assumptions, shoaling leads to the following effects:

- The wavelength *decrease*
- The phase velocity *decrease*
- The group velocity increases at first, and then *decrease*
- The wave amplitude decreases at first, and then *increase*

2.2 Refraction

In the previous section, the waves have been assumed to propagate normal to a coast with depth contours parallel to the coastline. In the following, the depth contours are still assumed parallel to the coastline, but the phenomenon occurring when the angle of propagation no longer is *normal* to the coast will be investigated. This phenomenon is known as *wave refraction.*

As explained in the previous section, the wave phase speed is decreased as the water depth decreases. When the wave approaches the coast with an angle, the presence of the sea bed is not felt simultaneously along the wave crest, see **Figure 2.6**. The part of the wave crest first affected by the presence of the seabed is slowed down, while the unaffected part continuous to travel with the initial phase velocity. This will lead to gradually bending the wave crest so that it is more closely aligned with the bottom contours.

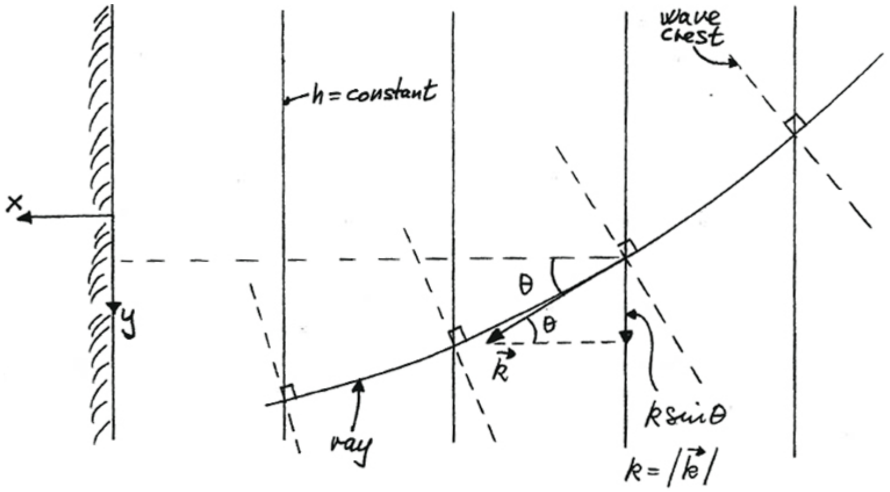

Figure 2.6: Wave refraction, Myrhaug (2006)

From **Equation 2.3** we see that

$$\vec{k} = k_x\vec{i} + k_y\vec{j} = \nabla\psi \tag{2.24}$$

The wave *ray* is, as indicated in the above figure, the curve tangent to the local wave number vector $\vec{k}$. The wave number vector is perpendicular to the wave crest, and thus the wave ray indicates the path of the wave crest (dashed lines perpendicular to the ray).

As $\vec{k}$ is the gradient of a scalar, it follows that $\nabla \times \vec{k} = 0$, Myrhaug (2006). This leads to the following relationship

$$\frac{\delta k_y}{\delta x} - \frac{\delta k_x}{\delta y} = 0 \tag{2.25}$$

The y-component of the wave number vector k_y is, as illustrated in the figure, $k_y = k\sin\theta$, where θ is the angle between the $\vec{k}$ and the x-axis. The x-component is given by $k_x = k\cos\theta$. Since the depth contours are parallel to the coast line, i.e. parallel to the y-axis, there will be no change of the wave number in y-direction $\frac{\delta k_x}{\delta y} = 0$.

From **Equation 2.25** we then get

$$\begin{aligned} \frac{\delta k_y}{\delta x} &= 0 \\ k_y &= const \\ k\sin\theta &= const \end{aligned} \tag{2.26}$$

By substituting **Equation 2.7** into the above equation, we get

$$\frac{\sin\theta}{c_w} = const \tag{2.27}$$

which is also known as *Snell's Law*, Myrhaug (2006).

As stated in **Section 2.1**, the phase velocity decreases as the water depth decreases, which leads θ to decrease to keep **Equation 2.27** constant. This leads the wave crest to be perpendicular to the coast as it reaches the beach. It also proves that if the wave crest initially propagates normal to the beach, the wave crest propagation angle will remain unchanged.

Depth refraction can cause a local increase or decrease in wave energy, and thus in wave amplitude. As the rays are bent according to **Equation 2.27**, the bathymetry can lead to spreading or focusing of the wave rays. This will lead to $b_1 \neq b_2$ in **Figure 2.4** and **Equation 2.20**. When the rays are focused ($b_2 < b_1$), the wave energy, and thus amplitude, is increased.

When the rays are spread ($b_2 > b_1$), the wave energy, and thus amplitude, are decreased. Both cases (A: spreading, B:focusing) are illustrated in **Figure 2.7**.

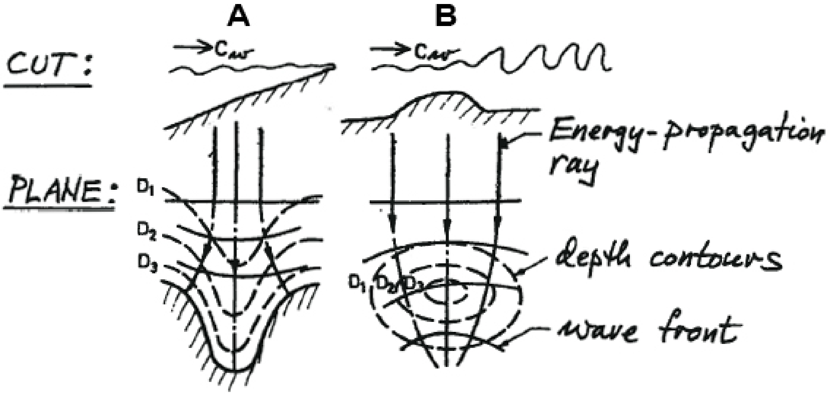

Figure 2.7: Examples of wave refraction, Myrhaug (2006). **A**: spreading of wave rays, **B**: focusing of wave rays

2.3 Neglected effects

2.3.1 Reflection

Wave reflection is a result of the presence of a wall, or an abrupt change in water depth, Myrhaug (2006), Haver (2011a). Since we assume a slow variation of water depth, this effect can be neglected.

2.3.2 Diffraction

Diffraction is when the waves are turned around a surface penetrating body or due to difference in wave amplitude along the wave crest, Myrhaug (2006), Holthuijsen (2007). The effect of diffraction is to turn the wave towards regions of lower wave amplitude. To my knowledge, there are no islands present within the Dogger Bank Zone, and the wind turbine foundations are assumed too slender relative to the waves appropriate for design for diffraction to be of interest. In addition it is in **Section 5.4** seen that diffraction is not included in the transformation of the incident wave spectrum in operational wave models, Holthuijsen (2007).

As refraction may lead to increased or decreased wave amplitude, it may result in a change of amplitude along the wave crest. For waves of low steepness, diffraction will try to *damp* the effect of refraction. Since the design wave will be of high steepness, the effect of diffraction is assumed negligible relative to other effect such as dissipative mechanisms.

3. Wave Breaking

Wave breaking occurs both in deep and shallow water and is one of the most nonlinear phenomenon affecting the waves as they propagate to shallow water.

According to Myrhaug (2006), the most common definition of *initiation* of wave breaking, is when *the very first air entrainment is visible on the surface of the wave.*

3.1 Breaking criteria

To establish breaking criteria in *deep water*, Stokes considered the highest possible two-dimensional wave of constant form that can propagate in constant water depth, Svendsen (2006), Myrhaug (2006). Based on the highest possible non-breaking Stokes wave[1], four criteria were obtained for the wave to break

- A crest angle *below* the crest angle corresponding to maximum wave steepness $\alpha = 120°$, see **Figure 3.1**
- Fluid particle velocity in the wave crest *above* the phase speed of the wave
- The downward directed vertical water particle acceleration close to the wave crest *larger than* $\frac{g}{2}$
- Wave steepness above the maximum wave steepness

$$s_{\max} = \frac{H}{\lambda} = 0.142 \tag{3.1}$$

obtained by Mitchell in 1893, Svendsen (2006)

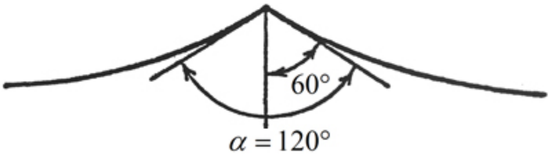

Figure 3.1: Angle corresponding to maximum wave steepness of the highest Stokes wave, Myrhaug (2006)

In shallow water, the breaking criterion is dependent on the water depth. To reduce the limiting parameters to just $\left(\frac{H}{d}\right)_{\max}$, waves with infinite wave length was considered (Solitary waves[2]), Svendsen (2006). In shallow water, the criterion was found by McCowan in 1894 to be

$$\left(\frac{H}{d}\right)_{\max} = 0.78 \tag{3.2}$$

Many scientists have been researching the exact value of **Equation 3.2**, and according to Svendsen (2006), Longuet-Higgins and Fenton obtained the value of highest accuracy in 1974

---

[1] More on Stokes wave theory in **Section 4.3**

[2] More on Solitary wave theory in **Section 4.5**

to be 0.8261. The value obtained by McCowan is still (un-justifiably) the most commonly used value.

Equation 3.1 and **3.2** represents breaking criterion for the outer extremes of wave depth, i.e. deep water and shallow water receptively. Miche established an interpolation function for arbitrary water depth, also referred to as the *Miche criterion*, Svendsen (2006)

$$\frac{H}{\lambda} = 0.142 \tanh(kd) \tag{3.3}$$

As $kd \to \infty$ in deep water, we see that the Miche criterion approaches the value of 0.142, which is the maximum steepness of the largest Stokes wave. To obtain the shallow water solution of the Miche criterion, we must evaluate **Equation 3.3** as $kd \to 0$. First we manipulate the equation by substituting the relationship between wave number and wave length

$$\begin{aligned} \frac{H}{\lambda} &= \frac{kH}{2\pi} = 0.142 \tanh(kd) \\ \frac{H}{d} &= \frac{2\pi \cdot 0.142 \tanh(kd)}{kd} \end{aligned} \tag{3.4}$$

Then evaluate the limit

$$\begin{aligned} \lim_{kd \to 0} \frac{H}{d} &= \lim_{kd \to 0} \frac{0.892 \tanh(kd)}{kd} \\ &\overset{L'H}{=} \lim_{kd \to 0} \frac{0.892}{\cosh^2(kd)} \\ &= 0.892 \end{aligned} \tag{3.5}$$

It is seen from this that the Miche criterion overestimates the shallow water breaking limit, when we compare this result with Longuet-Higgins and Fenton's result of 0.8261 or McCowan's 0.78. To make the Miche criterion match a different shallow water limit, it can be adjusted in the following way

$$\frac{H}{\lambda} = 0.142 \tanh(\beta kd) \tag{3.6}$$

As stated in Soulsby (1997), $\beta = 0,875$ gives the McCowan shallow water limit given in **Equation 3.2**. By solving **Equation 3.6** for β as done in **Equation 3.4** and **3.5** we find that $\beta = 0.9259$ gives the shallow water limit found by Longuet-Higgins and Fenton $\left(\frac{H}{d}\right)_{\max} = 0.8261$.

3.2 Types of breaking waves

Spilling breakers

Spilling breakers are the most common breaker form in deep water and on beaches, Myrhaug (2006). The spilling breaker is near symmetric and breaks at the crest where the entrapped air forms a "jet" moving down along the front of the wave, and is very close to the highest Stokes wave as describes in **Section 3.1**. The development of a spilling breaker is shown in **Figure 3.2**.

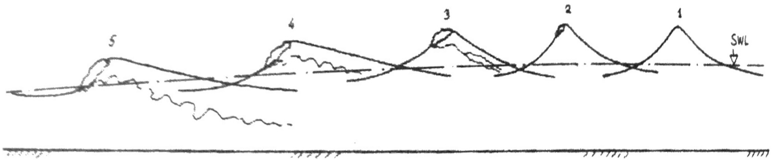

Figure 3.2: The development of a spilling breaker, propagating towards the left, Svendsen (2006)

Plunging breakers

The plunging breakers occur primarily in shallow water, but also frequently in deep water as well, Myrhaug (2006). They are very asymmetric and at breaking the crest shoot forward as a jet that plunges down into the wave trough in front of the crest, Svendsen (2006). The development of a plunging breaker is shown in **Figure 3.3**.

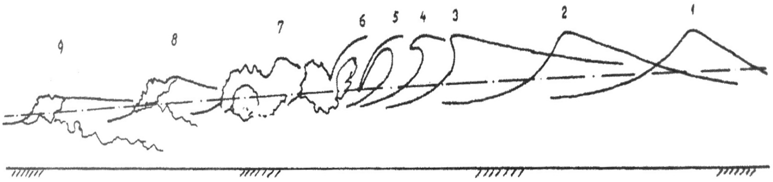

Figure 3.3: The development of a plunging breaker, propagating towards the left, Svendsen (2006)

This type of breaker is the most dangerous kind, at least for surface piercing bodies hit around step 3-5 in **Figure 3.3**. In combination with possible *slamming*, the load per unit length may well be 50 times the load from a non-breaking wave with equal height and period, Haver (2011a).

Surging breakers

The surging breakers only appear in the shallower part of the beach, and are therefore assumed less important than the two previously mentioned types of breakers, when it comes to offshore wind turbines. The development of a surging breaker is shown in **Figure 3.4**.

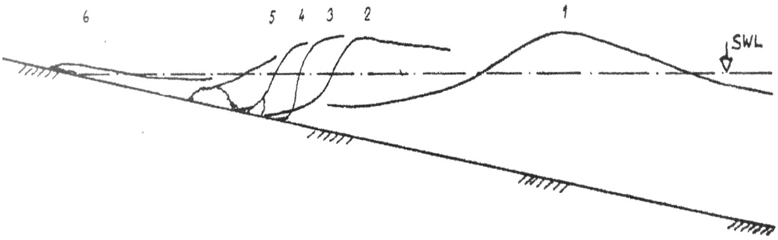

Figure 3.4: The development of a surging breaker, propagating towards the left, Svendsen (2006)

According to Holthuijsen (2007), the type of breaker can be determined by the surf similarity parameter or *Iribarren number*. The Iribarren number is given by $\xi = \tan\alpha\sqrt{\frac{\lambda_\infty}{H}}$ assuming a flat beach, where α is the bottom slope, λ_∞ is the deep water wave length and H is the wave height. By assuming a small angle bottom slope and substituting λ_∞ with the deep water relationship between wave length and wave period, we get

$$\xi = \alpha T_\infty \sqrt{\frac{1.56}{H}} \tag{3.7}$$

By evaluating the deep water wave height $H = H_\infty$ or the incipient breaking height $H = H_{br}$, the corresponding Iribarren ranges, given in **Table 3.1**, determines what kind of breaker to expect.

Table 3.1: What type of breaker to expect for given ranges of the Iribarren number, Holthuijsen (2007)

Type	Iribarren range	
Spilling	$\xi_\infty < 0.5$	$\xi_{br} < 0.4$
Plunging	$0.5 < \xi_\infty < 3.3$	$0.4 < \xi_{br} < 2.0$
Surging	$\xi_\infty > 3.3$	$\xi_{br} > 2.0$

4. Wave Theories

In the two previous chapters, the transformation of waves as they propagate to shallower water has been discussed. It is seen that nonlinear behavior appears and it is thus required to use an appropriate wave theory to be able to model some of these effects. In the following linear and higher order wave theory will be reviewed.

4.1 Governing equations

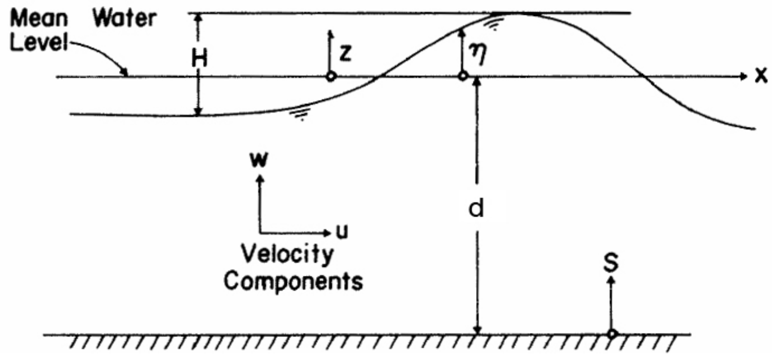

Figure 4.1: Definition sketch for a progressive wave system, Dean (1974). The wave elevation η is denoted ζ in the following

4.1.1 Assumptions

The water-wave phenomenon of interest is assumed idealized as a two-dimensional boundary value problem of *ideal flow.* Ideal flow meaning the fluid to be incompressible, irrotational and inviscid.

As the fluid is assumed incompressible, it follows from Faltinsen (1990) that

$$\nabla \cdot \vec{V} = 0 \tag{4.1}$$

where $\nabla = \frac{\delta}{\delta x}\vec{\imath} + \frac{\delta}{\delta z}\vec{k}$ and $\vec{V} = u\vec{\imath} + w\vec{k}$ when we consider the x-z-plane.

The velocity in the fluid is can be described by the velocity potential ϕ where

$$\vec{V} = \nabla\phi = \frac{\delta\phi}{\delta x}\vec{\imath} + \frac{\delta\phi}{\delta z}\vec{k} \tag{4.2}$$

and since the fluid also is assumed irrotational, i.e.

$$\nabla \cdot \vec{V} = 0 \tag{4.3}$$

it follows that the velocity potential satisfies the *Laplace equation*

$$\nabla^2\phi = 0 \tag{4.4}$$

4.1.2 Boundary Conditions

Bottom Boundary Conditions

At the assumed horizontal bottom, the vertical velocity component must be zero

$$\left(\frac{\delta\phi}{\delta z}\right)_{z=-d} = (w)_{z=-d} = 0 \tag{4.5}$$

Kinematic Free Surface Boundary Condition (KFSBC)

Due to impermeability, i.e. that the fluid particles do not leave the surface, and assuming long crested waves (i.e. $\frac{\delta}{\delta y} = 0$) the *kinematic free surface condition* is given in Faltinsen (1990) as

$$\frac{\delta\zeta}{\delta t} + \frac{\delta\phi}{\delta x}\frac{\delta\zeta}{\delta x} = \frac{\delta\phi}{\delta z} \text{ on } z = \zeta(x,t) \tag{4.6}$$

where $\zeta(x,t)$ is the wave elevation.

Dynamic Free Surface Boundary Condition (DFSBC)

Bernoulli's equation must be satisfied at the surface, and by evaluating the equation at two points at the surface, we get the *dynamic free boundary condition* given by Faltinsen (1990)

$$g\zeta + \frac{\delta\phi}{\delta t} + \frac{1}{2}\left(\left(\frac{\delta\phi}{\delta x}\right)^2 + \left(\frac{\delta\phi}{\delta z}\right)^2\right) = 0 \text{ on } z = \zeta(x,t) \tag{4.7}$$

4.2 Linear Wave Theory

The system of equations now introduced represents, according to Svendsen (2006), two difficulties:

1. The Laplace equation and bottom boundary condition are both *linear* while both the free surface boundary conditions are *nonlinear*
2. The free surface boundary conditions are both valid at the free surface, which position is also an unknown

This combination makes it *impossible* to analytically solve the problem without further simplifications.

The first simplification is made by evaluation the magnitude of the terms in the kinematic and dynamic free-surface conditions. In deep water (i.e. $d > \frac{\lambda}{2}$), the water particles are known to move in *circular* paths. One orbit is completed within one wave period T, and at the free surface, the diameter of the circular path must be the wave height (i.e. vertical distance from wave crest to wave trough). The velocity of this motion must then be

$$V = \frac{\pi H}{T} \tag{4.8}$$

The maximum horizontal and vertical velocity must be equal to this velocity, i.e.

$$\begin{aligned}\left(\frac{\delta\phi}{\delta x}\right)_{\max} &= \left(\frac{\delta\phi}{\delta z}\right)_{\max} = \frac{\pi H}{T} \\ &= O\left(\frac{H}{T}\right) = O\left(c_w\frac{H}{L}\right)\end{aligned} \tag{4.9}$$

where the expression for the phase speed has been utilized in the last term. As the velocity potential is harmonic, $\frac{\delta\phi}{\delta x}$ and $\frac{\delta\phi}{\delta z}$ will also be $O\left(c_w\frac{H}{L}\right)$.

The wave elevation must also have such an dependence so that

$$\frac{\delta\zeta}{\delta t} = O\left(c_w\frac{H}{L}\right) \tag{4.10}$$

$$\frac{\delta\zeta}{\delta x} = O\left(c_w\frac{H}{L}\right) \tag{4.11}$$

If we now assume the *wave steepness* $\frac{H}{L}$ to be small, i.e. $\frac{H}{L} \ll 1$, and insert **Equation 4.9**, **4.10** and **4.11** into the kinematic and dynamic boundary conditions, we see that the nonlinear terms can be neglected. We have then dealt with the first problem.

For the second problem, we assume the velocity potential to be proportional to the wave amplitude. By a Taylor expansion, the velocity potential can according to Pettersen (2007) be expressed as

$$\phi(x,\zeta,t) = \phi(x,0,t) + \zeta\frac{\delta\phi(x,0,t)}{\delta z} + ... \tag{4.12}$$

where the following terms on the right hand side can be neglected due to being dependent on the wave amplitude to the power of two and higher. As the velocity potential also is dependent on the wave amplitude, the second term on the right hand side of the Taylor expansion will also be dependent on the wave amplitude squared, and can thus also be neglected according to linear theory. This result in

$$\phi(x,\zeta,t) = \phi(x,0,t) \tag{4.13}$$

and we can transfer the dynamic and kinematic free surface conditions from $z = \zeta(x,t)$ to $z = 0$. The kinematic and dynamic free surface conditions can after these assumptions be simplified to:

$$\frac{\delta\zeta}{\delta t} = \frac{\delta\phi}{\delta z} \text{ on } z = 0 \tag{4.14}$$

$$g\zeta + \frac{\delta\phi}{\delta t} = 0 \text{ on } z = 0 \tag{4.15}$$

Velocity potential

Because the velocity potential is assumed periodic and must satisfy the Laplace equation, we can use the method of separation of variables to obtain the expression for the linearized velocity potential, as thoroughly derived in **Appendix C**:

$$\phi = \frac{\zeta_a g}{\omega}\frac{\cosh(k(z+d))}{\cosh(kd)}\sin(kx-\omega t)) \tag{4.16}$$

From this equation the velocity in x and z direction can be obtained by differentiation.

Dispersion relation

The dispersion relation is obtained by inserting the expression for the velocity potential into the *combined free surface condition*

$$\frac{\delta^2\phi}{\delta t^2} + g\frac{\delta\phi}{\delta z} = 0 \text{ on } z = 0 \tag{4.17}$$

which yields

$$\omega^2 = kg\tanh(kd) \tag{4.18}$$

4.3 Stokes Wave Theory

Assumptions and simplifications have been made to linearize the solution of the governing Laplace equation. Real waves in intermediate water are not described correctly by linear wave theory. One of the nonlinear characteristics is illustrated in **Figure 4.2** where the sinusoidal wave profile is compared to a "real" wave in intermediate water.

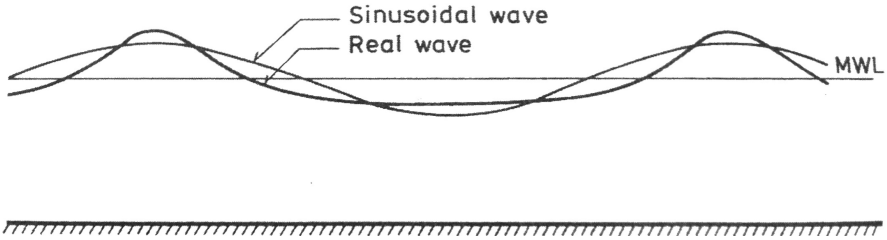

Figure 4.2: Comparison of sinusoidal and "real" wave profiles in intermediate water, Svendsen (2006)

How Sir Georg Gabriel Stokes extended the wave theory to best satisfy the mathematical formulation of the water wave theory using the *perturbation approach* will briefly be presented.

4.3.1 Second Order Stokes Waves

The wave steepness is defined as $s = \frac{H}{\lambda}$, still assumed much less than 1, and is according to Svendsen (2006) the proper expansion parameter for Stokes waves. The quantities in focus can be expanded into power series:

$$\phi = s\phi_1 + s^2\phi_2 + ... \tag{4.19}$$

$$\zeta = s\zeta_1 + s^2\zeta_2 + ... \tag{4.20}$$

The Laplace equation can then be written as

$$s\left(\frac{\delta^2\phi_1}{\delta x^2} + \frac{\delta^2\phi_1}{\delta z^2}\right) + s^2\left(\frac{\delta^2\phi_2}{\delta x^2} + \frac{\delta^2\phi_2}{\delta z^2}\right) + ... = 0 \tag{4.21}$$

The KFSBC (on $z = \zeta$) can be written as

$$s(\frac{\delta\zeta_1}{\delta t} - \frac{\delta\phi_1}{\delta z}) + s^2(\frac{\delta\zeta_2}{\delta t} - \frac{\delta\phi_2}{\delta z} + \frac{\delta\phi_1}{\delta x}\frac{\delta\zeta_1}{\delta x}) + ... = 0 \tag{4.22}$$

The DFSBC (on $z = \zeta$) can be written as

$$s\left(g\zeta_1 + \frac{\delta\phi_1}{\delta t}\right) + \\ s^2\left(g\zeta_2 + \frac{\delta\phi_2}{\delta t} + \frac{1}{2}\left[\left(\frac{\delta\phi_1}{\delta x}\right)^2 + \left(\frac{\delta\phi_1}{\delta z}\right)^2\right]\right) \\ + \ldots = 0 \tag{4.23}$$

Again we have the problem that the position of the free surface is varying (problem 2 in **Section 4.2**). By a Taylor expansion of the velocity potential, as for linear theory, we can express the KFSBC and DFSBC[1] for $z = 0$.

By neglecting all terms proportional to s to the power of two and higher, we see that we have the exact same equations as in linear theory, which yields that

$$\phi_1 = \frac{\zeta_a g}{\omega}\frac{\cosh(k(z+d))}{\cosh(kd)}\sin(kx - \omega t) \tag{4.24}$$

By solving the equations for terms proportional to s^2 we will get the expression for ϕ_2. This is done in a similar manner as described in **Appendix C**, but the details on deriving the second order velocity potential falls outside the scope of this thesis – the keen reader is referred to Svendsen (2006). This result in

$$\phi_2 = \frac{3}{8}\zeta_a^2\frac{\cosh\left(2k\left(z+d\right)\right)}{\sinh^4\left(kd\right)}\sin\left(2(kx - \omega t)\right) \tag{4.25}$$

The second order velocity potential is then given by $\phi = \phi_1 + \phi_2$.

By inserting the expression for ϕ_2 into the KFSBC translated to $z = 0$, similarly as what was done in **Appendix C**, the expression for ζ_2 is found to be

$$\zeta_2 = \frac{1}{4}k\zeta_a^2\frac{\cosh\left(kd\right)}{\sinh^3\left(kd\right)}\left(2 + \cosh\left(2kd\right)\right)\cos\left(2\left(kx - \omega t\right)\right) \tag{4.26}$$

The second order wave elevation is then given by $\zeta = \zeta_1 + \zeta_2$.

We can see that the second order term has a frequency equal to two times the frequency of the linear component, and a corresponding wave number to twice the wave number of the linear solution, Haver (2011a). This is illustrated in **Figure 4.3**.

---

[1] As we now cannot neglect the higher order terms, it means that we have to include more terms in **Equation 4.22** and **4.23** to translate them to z=0, which was not necessary for linear theory. Details on this are outside the scope of this thesis.

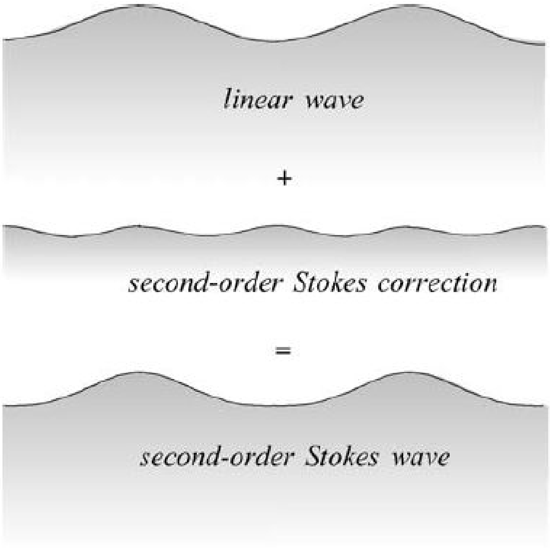

Figure 4.3: Surface profile of a second order Stokes wave, Holthuijsen (2007)

The dispersion relation is the same as for linear theory, but a correction occurs for third and higher order, see **Section 4.3.2**.

Convergence

The criterion for convergence is that the second order term is *less* than the first order term, or $\frac{\zeta_2}{\zeta_1} \ll 1$. By inserting the expression for ζ_1 and ζ_2 into the requirement, we get that

$$\frac{3}{8}\frac{k\zeta_a \cosh(2kd)}{\cosh(kd)\sinh^3(kd)} \ll 1 \tag{4.27}$$

Because $\sinh(kd) = \frac{e^{kd}-e^{-kd}}{2}$ and $\cosh(kd) = \frac{e^{kd}+e^{-kd}}{2}$, in deep water, where $kd \to \infty$, both $\sinh(kd)$ and $\cosh(kd)$ will approximately be equal to e^{kd}, as e^{-kd} goes to zero. Thus, the requirement for convergence in deep water simplifies to

$$3e^{-2kd}k\zeta_a \ll 1 \tag{4.28}$$

This is of course satisfied as kd is large and $k\zeta_a$ is small in deep water.

Deep water is as mentioned the definition of water depth where $\frac{d}{\lambda} \geqslant \frac{1}{2}$ or $d \geqslant \frac{\pi}{k}$ if we insert the relationship between wave number and wave length. As the convergence requirement is decreasing with increasing depth, the largest value of the requirement (within what is defined as deep water) will be obtained for the smallest value of d in deep water, i.e. $d = \frac{\pi}{k}$. The requirement is also increasing with increasing wave steepness $s = \frac{H}{\lambda} = \frac{\zeta_a k}{\pi}$. As mentioned in **Section 3.1** the maximum steepness of Stokes waves are $s = \frac{1}{7}$ or $\zeta_a k = \frac{\pi}{7}$, which means that the maximum value of the convergence requirement in deep water is

$$\frac{3\pi}{7}e^{-2\pi} = 0.0025 \ll 1 \tag{4.29}$$

so we see that convergence is achieved for all water depths defined as *deep water*.

In shallow water, $kd \to 0$, $\cosh(kd) \to 1$ and $\sinh(kd) \to kd$ so that the requirement becomes

$$\frac{3}{8}\frac{k\zeta_a}{(kd)^3} \ll 1 \;\Rightarrow\; \frac{k\zeta_a}{(kd)^3} \ll \frac{8}{3} \Rightarrow U_r \ll \frac{8}{3} \tag{4.30}$$

where $U_r = \frac{k\zeta_a}{(kd)^3}$ is the *Ursell number* (this is, according to Svendsen (2006), exactly where Stokes found this parameter). From this it is clear that for shallow water, i.e. small kd, this requirement cannot be met.

Shallow water is per definition where $\frac{d}{\lambda} < \frac{1}{20}$, i.e. $kd < \frac{\pi}{10}$. The maximum value of the convergence requirement in shallow water is thus obtained for

$$\begin{aligned} \frac{3}{8}\frac{\zeta_a}{d\left(\frac{\pi}{10}\right)^2} &< 1 \\ \frac{\zeta_a}{d} &< 0.263 \end{aligned} \tag{4.31}$$

This is much less than the breaking criteria given by McCowan $\left(\frac{\zeta_a}{d}\right)^{MC}_{\max} = 0.39$ and Longuet-Higgins $\left(\frac{\zeta_a}{d}\right)^{LH}_{\max} = 0.413$ (see **Section 3.1**), and implies that as the wave propagates to very shallow water, the Second order wave theory might not be sufficient.

Second order surface profile

As found in Myrhaug (2006), a converging combination of $k\zeta_a$ and kh may give a surface profile with an unphysical "bump" in the wave trough, see **Figure 4.4**

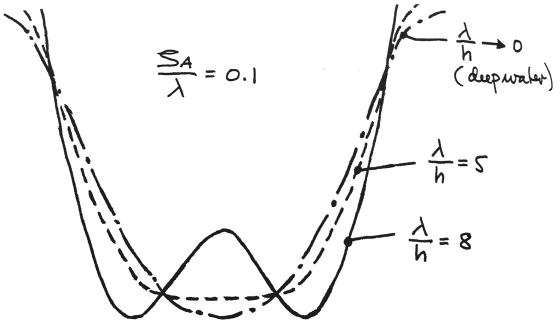

Figure 4.4: Surface profile for different combinations of $k\zeta_a$ and kh (figure out of scale), Myrhaug (2006). The water depth d is denoted h in the figure

This unphysical bump appears when the second derivative of the surface profile (w.r.t. x) at the trough is negative. Since we know that the wave trough appears at $kx - \omega t = \pi$, the requirement for the bump *not to appear* can be expressed as

$$\begin{aligned} \frac{\delta^2\zeta}{\delta x^2} &= k^2\zeta_a - k^3\zeta_a^2\frac{\cosh(kd)}{\sinh^3(kd)}\left(2+\cosh(2kd)\right) \geqslant 0 \\ k\zeta_a &\leqslant \frac{\sinh^3(kd)}{\cosh(kd)\left(2+\cosh(2kd)\right)} \end{aligned} \tag{4.32}$$

For deep water, this requirement simplifies to $k\zeta_a \leqslant \frac{1}{2}$, or $\frac{H}{\lambda} \leqslant \frac{1}{2\pi} \approx \frac{1}{6.283}$, which is *less strict* than the limiting steepness criterion of $\frac{H}{\lambda} < \frac{1}{7}$.

In shallow water, the requirement given in **Equation 4.32** simplifies to

$$\begin{aligned} k\zeta_a &\leqslant \frac{(kd)^3}{3} \\ \frac{k\zeta_a}{(kd)^3} &= U_r \leqslant \frac{1}{3} \end{aligned} \tag{4.33}$$

By comparing this to the requirement for convergence in **Equation 4.30**, we see that this requirement is stricter, and thus is used as the criterion for maximum wave amplitude.

As the *wave crest* appears when $kx - \omega t = 0$ and the *wave trough* appears when $kx - \omega t = \pi$they can be expressed as

$$\zeta_c = \zeta\left(\frac{\omega t}{k}, t\right) = \zeta_a + \frac{1}{4}k\zeta_a^2\kappa \tag{4.34}$$

$$\zeta_t = \zeta\left(\frac{\pi + \omega t}{k}, t\right) = -\zeta_a + \frac{1}{4}k\zeta_a^2\kappa \tag{4.35}$$

where $\kappa = \frac{\cosh(kd)}{\sinh^3(kd)}\left(2 + \cosh\left(2kd\right)\right)$. The wave height is defined as the vertical distance from the wave crest to the wave trough, and thus $H = \zeta_c - \zeta_t = 2\zeta_a$, which is equal to the wave height in linear theory.

The second order crest height is observed from **Equation 4.34** to be *larger* than the linear theory wave crest, and the second order wave trough is observed from **Equation 4.35** to be *shallower* than the linear theory wave trough. As $\kappa \to \kappa_0 = 2$ in deep water and $\kappa \to \kappa_{sw} = \frac{3}{(kd)^3}$ in shallow water, we get that

$$\frac{\kappa_{sw}}{\kappa_0} = \frac{3}{2(kd)^3} \tag{4.36}$$

which increases for decreasing water depth. This means that the effect of a larger crest height and shallower wave trough compared to linear theory is amplified as the wave propagates towards shallower water.

It should also be mentioned that the Stokes wave profile is symmetric with respect to the vertical axis through the wave crest, and thus cannot be used to properly model asymmetric nonlinear waves.

Second order drift

Another effect of the nonlinearity of the waves is that the fluid particles no longer will move in enclosed paths, as they do in linear theory. They will, according to Myrhaug (2006), have a net horizontal velocity different from zero which can be shown to be

$$U = c_w k^2 \zeta_a^2 e^{2kz_1} \tag{4.37}$$

where z_1 is the mean vertical position of the fluid particle during a wave cycle. During one wave period the wave particle is drifted $S = UT$ as illustrated in **Figure 4.5**. We can from **Equation 4.37** see that the convection is maximum at the free surface, and will exponentially decrease with water depth.

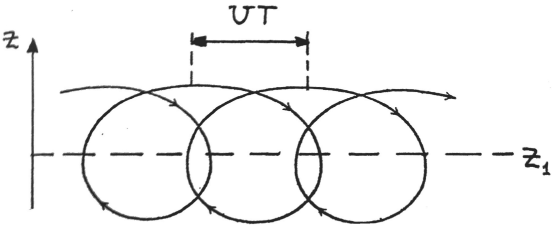

Figure 4.5: Water particle path for second order wave profile, Myrhaug (2006)

4.3.2 Higher order Stokes waves

In the previous, the new features entering the theory when extending from linear waves to second order waves was presented. This section will shed light on how even higher order approximations will modify the wave description.

Third order Stokes waves

By looking at the third order expansion of Stokes waves theory, two new features are added to the wave characteristics. These features are also present in all higher order approximations as well. The two new features are

1. The wave height is no longer twice the linear wave amplitude, i.e. $H \neq 2\zeta_a$, when we include the terms proportional to s^3 (see **Section 4.3.1**). The wave profile will be on the form
$$\zeta = \zeta_a^1 \cos(\theta) + \zeta_a^2 \cos(2\theta) + \zeta_a^3 \cos(3\theta) \tag{4.38}$$
where ζ_a^n is the amplitude of the n'th order correction for $n \geqslant 2$, and $\theta = kx - \omega t$, Svendsen (2006). The vertical distance between the wave height and wave trough will then become
$$H = 2\left(\zeta_a^1 + \zeta_a^3\right) \tag{4.39}$$
which for higher order will include all *uneven* terms in the right hand parenthesis, Svendsen (2006).
2. The phase speed will be dependent on the *wave height* in addition to the water depth and frequency, which make the waves both frequency and amplitude dispersive, Svendsen (2006).

Fifth and higher order Stokes waves

The method of expanding Stokes theory to higher order makes it *theoretically* possible to get a Stokes wave theory of infinite order. With increasing order, more terms are included, and it makes it a tedious job to derive. According to Svendsen (2006) and Dean and Dalrymple (1991), Cokelet expanded the Stokes wave theory to 110th order. This resulted in several surprising features, including the fact that the phase velocity, wave energy and wave momentum all reach their maximum values at wave heights slightly *smaller* than the highest wave.

The fifth order approximation of Stokes waves has for many years been used for offshore applications, Svendsen (2006), but the details on this theory will obviously not be given here, as the features previously described also are inherent in this order of approximation.

4.4 Stream function wave theory

Due to the difficulty of expanding Stokes wave theory to high orders, it was desirable to have wave theories that could be developed by a computer to any order, Dean and Dalrymple (1991). The first such theory was developed by Chappelear involving the velocity potential. Dean (1965) used the stream function to develop the *stream function theory* which was computationally simpler than Chappelear's method.

The stream function method is a *numerical solution* (in contrast to the analytical Stokes waves) to the exact governing equations and their boundary conditions, and is based on expanding the *unknown* stream function and surface elevation into *fourier series.* The stream function in the x-z-coordinate system is, according to Dean and Dalrymple (1991), defined as

$$\frac{\delta\psi}{\delta z} = \frac{\delta\phi}{\delta x} = u \tag{4.40}$$

$$-\frac{\delta\psi}{\delta x} = \frac{\delta\phi}{\delta z} = w \tag{4.41}$$

and will thus satisfy the Laplace equation. The coordinate system is set to follow the wave with the phase velocity, resulting in removing t as a variable. The solution will be on the form

$$\psi(x,z) = c_w z + \sum_{n=1}^{N} X(n) \sinh\left(nk\left(d+z\right)\right) \cos nkx \tag{4.42}$$

where N is the order of approximation and c_w is the phase velocity of the wave. N=1 gives the same solution as linear wave theory.

As the free surface *is* a stream line, the KFSBC is satisfied exactly. The parameters $X(n)$ in the stream function expression by Dean (1965) are chosen by a numerical perturbation procedure that provides a *best fit* to the *dynamic free surface boundary condition.* As for stokes waves, the wave form is assumed constant, and symmetrical with respect to the vertical axis through the wave crest.

It was later found that the solution technique described by Dean (1965) does not apply to the *highest waves.* According to Svendsen (2006), the approach presented by Rienecker and Fenton applies even to the highest waves, if a sufficient order is chosen.

4.5 Solitary waves

To allow for waves with a *finite amplitude* in very shallow water, the expansion cannot be done for the wave steepness (which must be assumed much less than one).The expansion procedure is, however, done for the parameter α/β, where $\alpha = \frac{\zeta_a}{d}$ and $\beta = \frac{d^2}{\lambda^2}$, Dean and Dalrymple (1991).

By assuming the waves to be of a constant form, symmetric about the z-axis and of infinite length, the solution of the wave profile becomes

$$\zeta = \frac{\zeta_a}{\cosh^2\left[\sqrt{\frac{3}{4}\frac{\zeta_a}{d^3}}\left(x - c_w t\right)\right]} \tag{4.43}$$

As the wave length is assumed infinitely long, there will not be a second wave crest further down the x-axis (i.e. not periodic), and the wave is thus named the *solitary wave.* For engineering use, one might assume a wave of infinite length has no value, but the *effective* length is much less. According to Dean and Dalrymple (1991), 95% of the area underneath a plot of the wave profile is contained within the length

$$l = \frac{2.12d}{\sqrt{\zeta_a/d}} \tag{4.44}$$

see **Figure 4.6**.

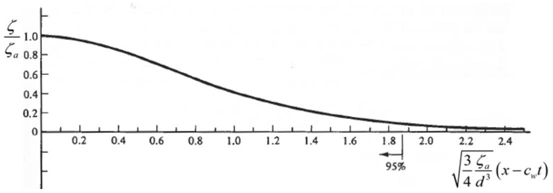

Figure 4.6: Dimensionless wave profile of a solitary wave, Dean and Dalrymple (1991)

4.6 Cnoidal Wave Theory

According to Dean and Dalrymple (1991), Korteweg and Devries managed to develop a shallow water wave theory where periodic waves were allowed to exist. It is for shallow water ($kd \to 0$) reduced to the solitary wave theory and for small wave amplitude ($k\zeta_a \to 0$) reduces to linear wave theory.

The wave profile is developed in terms of a *Jacobian elliptic integral*, $cn(u)$, and was therefore named *cnoidal* wave theory in the same way that linear theory are also called *sinusoidal* theory, due to the presence of sine or cosine.

For further details, see Dean and Dalrymple (1991).

4.7 Relative validity of wave theories

An important question is: *Which wave theory to use when?*. To answer the question, one must know the validity of the various wave theories.

There are two types of validity, namely *analytical validity* and *experimental validity*. Analytical validity is based on how well a theory satisfies the governing equations of the boundary value problem formulation. Experimental validity is based on how well the theory agrees with experimental measurements. It should be noted that good analytical validity not necessarily imply good representation of the natural phenomenon, because we do not know if the formulation has included *all* essential features of the wave motion (we assume ideal flow).

Dean (1970) examined the analytical validity of different wave theories by evaluating the root-mean-square errors in the kinematic and dynamic free surface conditions. **Figure 4.7** shows his result of how the different theories best fit the DFSBC (note that the fifth order Stream function theory is suggested as being valid except in the shaded area).

As the parameters wave height H, wave period T and water depth d uniquely define the characteristics of a periodic wave system propagating in uniform water depth, the dimensionless parameters $\frac{H}{gT^2}$ and $\frac{d}{gT^2}$ also uniquely define the these characteristics. The range of these parameters in **Figure 4.7** are covering most engineering conditions of interest.

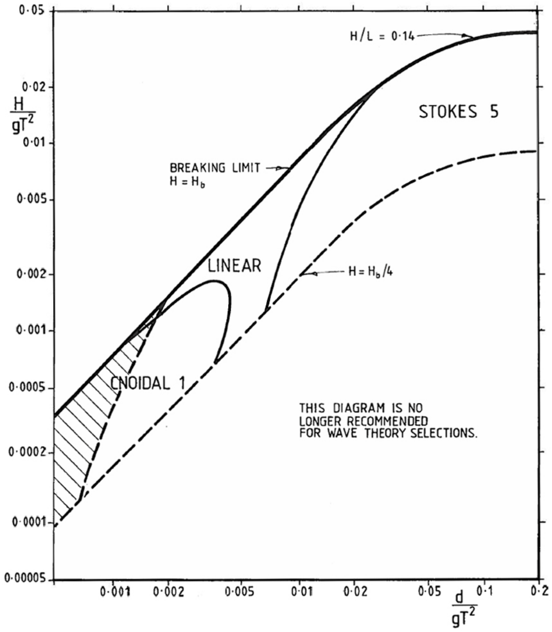

Figure 4.7: Ranges of where selected wave theories give the best fit of the dynamic free surface condition (DFSBC) in logarithmic scale. Fifth order Stream function theory is suggested as being valid everywhere except in the shaded area. Figure from Barltrop et al. (1990), based on results by Dean (1970). $L = \lambda$, H_b =breaking wave height

For deep water the dimensionless water depth range becomes

$$\frac{d}{\lambda} = \frac{kd}{2\pi} = \frac{(2\pi)^2 d}{2\pi g T^2} > \frac{1}{2}$$

$$\frac{d}{gT^2} > \frac{1}{4\pi} \approx 0.08 \tag{4.45}$$

where the relationship between wave length and wave number in addition to the deep water dispersion relation has been utilized.

Similarly, the shallow water dimensionless water depth range becomes

$$\frac{d}{\lambda} = \frac{kd}{2\pi} = \frac{2\pi d}{2\pi T\sqrt{gd}} < \frac{1}{20}$$

$$\frac{d}{gT^2} < \left(\frac{1}{20}\right)^2 = 0.0025 \tag{4.46}$$

Intermediate water depth is thus defined by $0.08 < \frac{d}{gT^2} < 0.0025$.

Méhauté (1976) has presented the approximate range of validity of various theories which is shown in **Figure 4.8**. He did *not* perform a quantitative investigation of the errors made by the different theories, so the plot is somewhat arbitrary and merely *qualitative*. There is, however, some agreement with the results presented by Dean (1970).

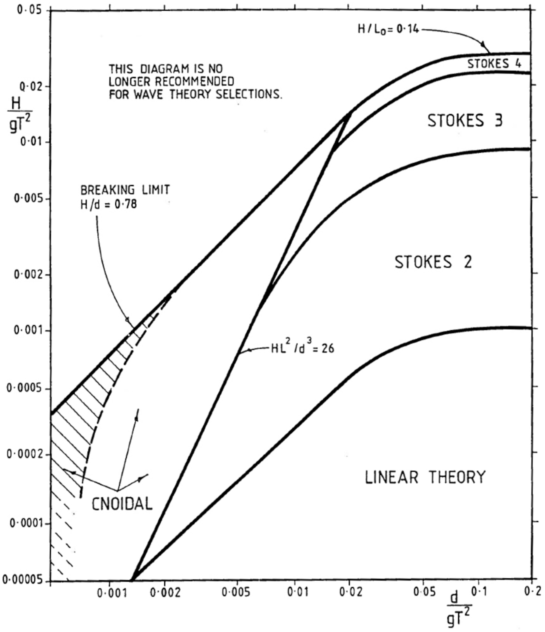

Figure 4.8: Qualitative ranges of validity of wave theories. Fifth order Stream function theory is suggested as being valid except in the shaded area. Figure from Barltrop et al. (1990), originally from Méhauté (1976)

Barltrop et al. (1990) took the qualitative ranges of validity by Méhauté (1976) (see **Figure 4.8**) and moved the boundaries in accordance with the agreement of

- Particle velocity under the wave crest
- Particle acceleration under the wave crest
- Wave height above still water level
- Wavelength

The theories assessed were linear wave theory, Stokes 5th order theory, and Stream function theory. The result can be seen in **Figure 4.9** and **4.10**, and is recommended used for selecting appropriate wave theory. It should be noted that

- Stream function theory is recommended for near the limit of breaking wave height
- None of the theories is theoretically correct at the breaking limit
- The upper limit is recommended set at 0.9 times the breaking wave height
- Multiple wave crests may occur also for the Stream function theory, so the surface profile should be checked.

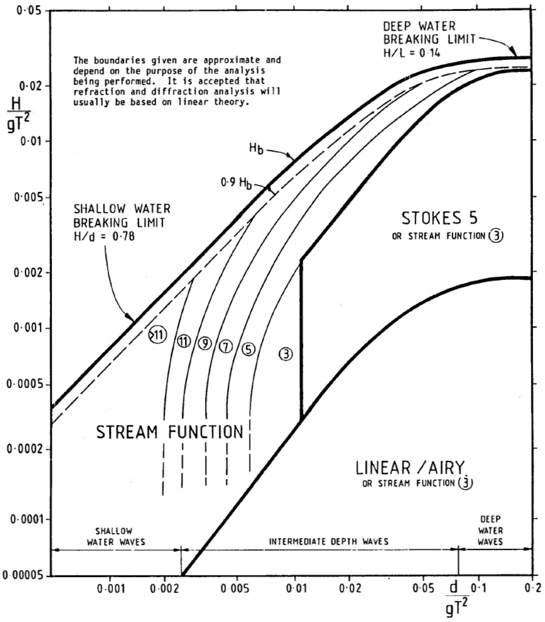

Figure 4.9: Regular wave theory selection diagram by Barltrop et al. (1990), logarithmic scales. The circled numbers indicate what order of the Stream function to apply

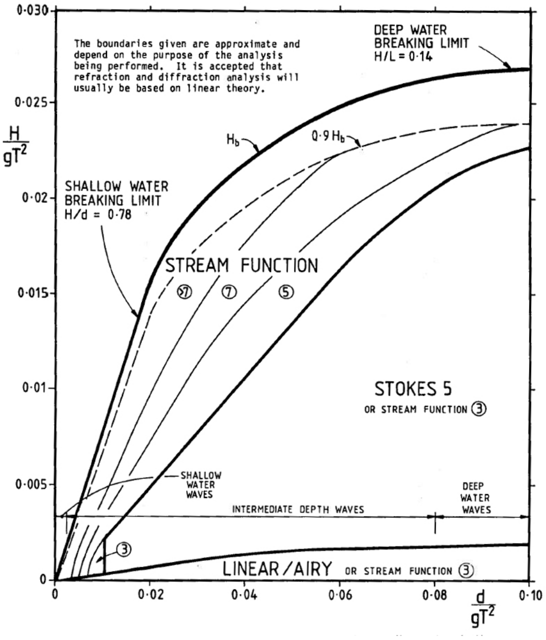

Figure 4.10: Regular wave theory selection diagram by Barltrop et al. (1990), linear scales. The circled numbers indicate what order of the Stream function to apply

5. Finite Water Depth Effects on the Wave Spectrum

The regular wave effects discussed in **Chapter 2** will also be present in the propagation of an irregular *sea state* from deep to shallow water. The sea state is described by the *wave spectrum*. In this section, the focus will be on how the wave spectrum is changed in space and time.

5.1 The energy balance equation

The energy balance equation represents *the time evolution of the wave spectrum*, Holthuijsen (2007):

$$\frac{dS(\omega,\theta,x,y,t)}{dt} = \Omega(\omega,\theta,x,y,t) \tag{5.1}$$

The right hand side, the *source term* Ω, represents all physical processes which transfer energy to, from or within the spectrum, Myrhaug (2006).

By an Eulerian approach (reference system fixed relative to the earth, whereas a Lagrangian approach would follow the water particles), we consider a grid as illustrated to the left in **Figure 5.1**.

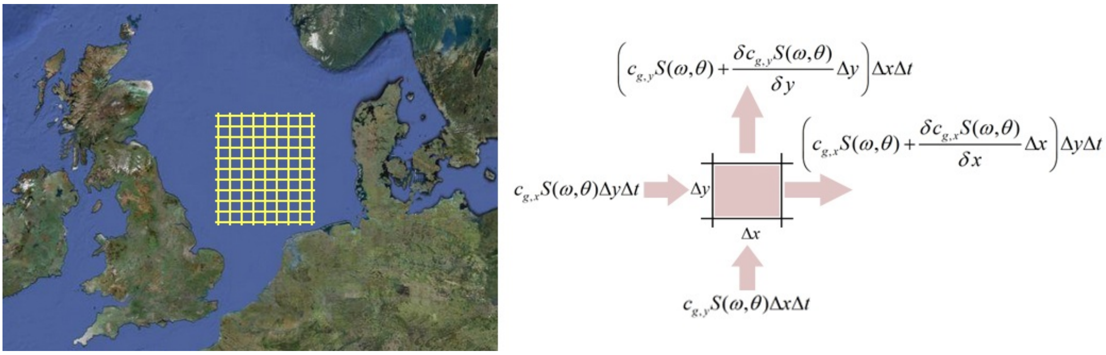

Figure 5.1: (Left:) A grid for the Eulerian approach of wave energy modeling. (Right:) Energy flux through a cell in the Eulerian grid

By considering the energy flux through one of the cells in the grid (energy propagating with the group velocity), as shown to the right in **Figure 5.1**, and through a *bin* in the directional space due to refraction or diffraction, see **Figure 5.2**, the total energy balance can be derived. Details on this derivation will not be given here, but the interested reader is referred to Holthuijsen (2007). The **energy balance equation** is then given by

$$\frac{\delta S}{\delta t} + \frac{\delta c_{g,x}S}{\delta x} + \frac{\delta c_{g,y}S}{\delta y} + \frac{\delta c_{\theta}S}{\delta \theta} = \Omega \tag{5.2}$$

where

$S = S(\omega, \theta, x, y, t)$, Wave spectrum
$\Omega = \Omega(\omega, \theta, x, y, t)$, Source term
$c_{g,x}, c_{g,y}$ = Group velocity in x,y-direction, now varying due to shoaling.
c_θ = Refraction- or diffraction-induced turning rate of the individual wave components, Holthuijsen (2007).

The first term on the left hand side describes the change of energy within the cell, the second due to net energy import in x-direction, the third due to net energy import in y-direction, and the last term due to net import of energy in θ-direction, Holthuijsen (2007).

The energy balance equation, as given in **Equation 5.2** is identical to the expression in deep water, except that the last term is not present for deep water (no refraction or diffraction), and that the group velocity is constant in x- and y-direction (no shoaling).

The source term on the right hand side of **Equation 5.2** can be divided into three components

$$\Omega = \Omega_{in} + \Omega_{nl} + \Omega_{ds} \tag{5.3}$$

where

Ω_{in} = Energy generation from the wind
Ω_{nl} = Nonlinear wave-wave interactions
Ω_{ds} = Energy dissipation

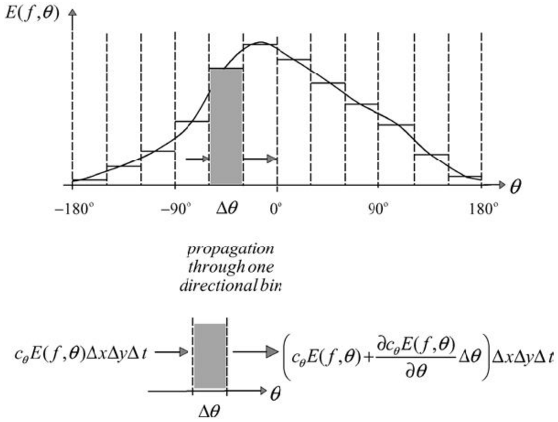

Figure 5.2: Top: directional wave spectrum for a given x,y,t. Bottom: Energy flux through a *bin* $\Delta\theta$ in the directional space due to refraction or diffraction, Holthuijsen (2007)

In the following, the effects of the mentioned phenomena on the wave spectrum will briefly be presented.

5.2 Shoaling

The effect of shoaling is to increase the wave amplitude, which will result in increased energy in the wave spectrum. This is more pronounced for the low frequency waves than for high frequencies, because for high frequency waves, the water may be defined as *relatively* deep water, where shoaling does not appear. As the effect is greater for lower frequencies, shoaling will result in shifting the mean frequency to a somewhat lower frequency. The resulting effect is illustrated in **Figure 5.3**

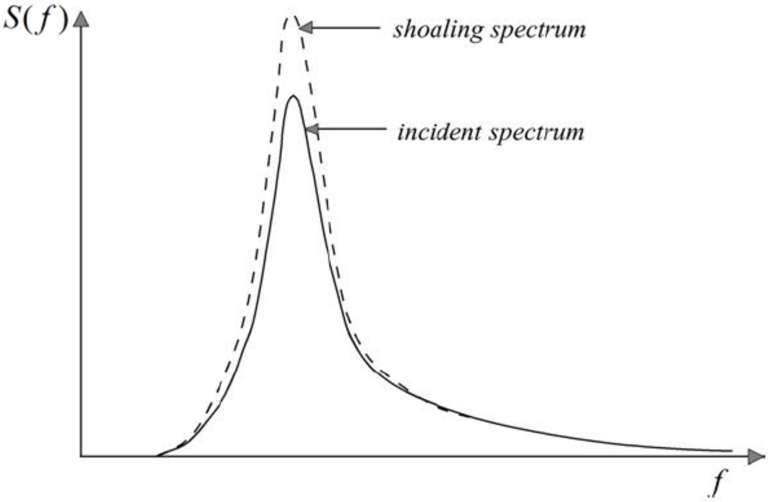

Figure 5.3: The qualitative effect of shoaling on the wave spectrum, Holthuijsen (2007)

.

5.3 Refraction

When the coast line is smooth and the bathymetry is slowly varying, refraction will turn the wave components in approximately the same direction, leading to a *narrowing* of the directional wave spectrum. When the coast is not smooth, refraction would lead to a more chaotic wave pattern for long crested, low frequency waves (swell conditions). For short crested wind-sea conditions, the mixing effect of refraction on waves with different direction and frequency lead to smoothing wave height and mean wave direction, Holthuijsen (2007).

5.4 Diffraction

The effect of diffraction is, as mentioned, that the waves are bent towards the area of lower amplitude. This is also the case for random, short crested waves, but since the waves approaches from many different directions at the same time, the effect will be much reduced. The **diffraction is therefore neglected** in wave models based on the energy balance equation, which leads c_θ in **Equation 5.2** to just represent refraction, Holthuijsen (2007).

5.5 Energy generation from wind Ω_{in}

The energy transfer from the wind to the waves Ω_{in} is, as given by Holthuijsen (2007) (originally Cavaleri and Malanotte-Rizzoli (1981) and Miles (1957))

$$\Omega_{in} = \alpha + \beta S(\omega, \theta) \tag{5.4}$$

where α describes the initial energy transfer, and β is proportional to the wind direction and wind speed over the phase speed of the waves, i.e. $\beta \sim \left[\frac{U\cos(\theta-\theta_{wind})}{c_w}\right]^2$. Here U is the wind speed, θ is the wave direction, θ_{wind} is the wind direction and c_w is the phase speed of the wave. As the phase speed of the waves decrease with reduced depth, this will result in an increased rate of energy transfer from the wind to the waves, compared to deep water. It should also be mentioned that most wave models restrict $\beta < 0$ to avoid energy transfer from the waves to the wind, Holthuijsen (2007).

As the energy transfer is also proportional to the wave spectrum itself, the shape of the source term will be the same as for the wave spectrum. The result is presented in **Figure 5.4**.

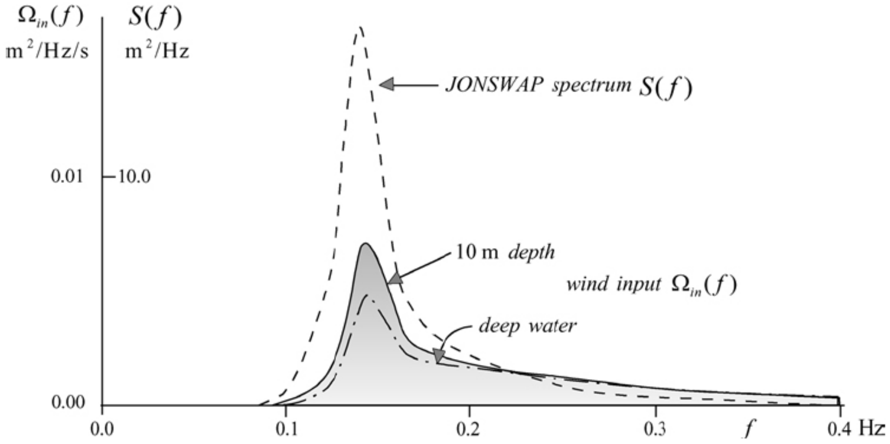

Figure 5.4: The energy transfer from the wind to the sea state. The effect is largest around the spectral peak period, and the effect of reduced water depth is also shown. $H_s = 3.5m$, $T_{peak} = 7s$ and $U_{10} = 20m/s$, Holthuijsen (2007)

.

5.6 Nonlinear wave-wave interactions Ω_{nl}

The source term for the nonlinear wave-wave interactions can, in shallow water, be divided in two components

$$\Omega_{nl} = \Omega_{nl,4} + \Omega_{nl,3} \tag{5.5}$$

where $\Omega_{nl,4}$ is the *quadruplet wave-wave interaction*, or 4-wave interaction, and $\Omega_{nl,3}$ is the *triad wave-wave interaction*, or 3-wave interaction, Holthuijsen (2007).

Common for both of these wave-wave interactions is the mechanism of *transferring* energy amongst waves with different frequency and direction due to resonance, so no energy is generated, nor dissipated. In the quadruplet wave-wave interaction this happens between 4 wave components, and is present in both deep and shallow water. In the triad wave-wave interaction this happens between three wave components and is just present in shallow water.

The quadruplet wave-wave interactions transfer energy from the peak frequency band to lower and higher frequencies, as shown in **Figure 5.5**. The effect increases with decreasing depth.

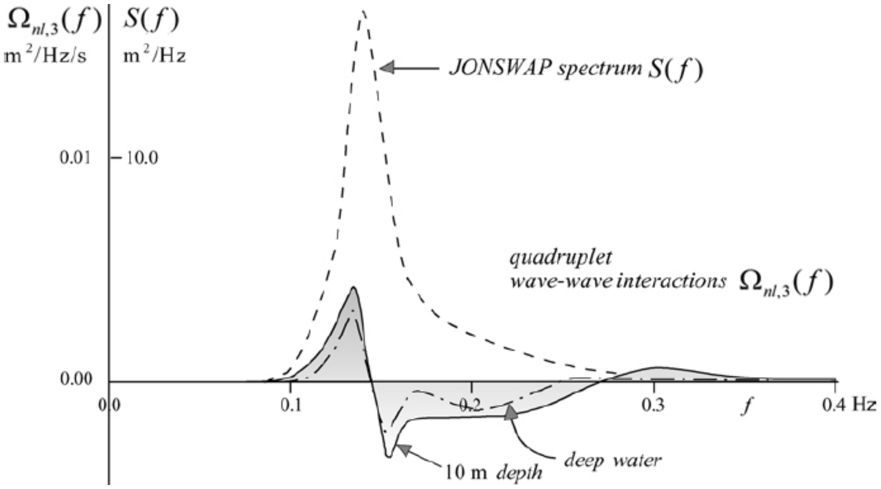

Figure 5.5: The energy distribution due to quadruplet wave-wave interactions for a JONSWAP spectrum in deep and in shallow water (10 m). Energy is transferred to lower and higher frequencies, and the effect is more pronounced for shallow water. $H_s = 3.5m$ and $T_{peak} = 7s$, Holthuijsen (2007)

.

The triad wave-wave interactions transfer energy from a smaller frequency band around the peak frequency to a frequency band of approximately twice the frequency, see **Figure 5.6**.

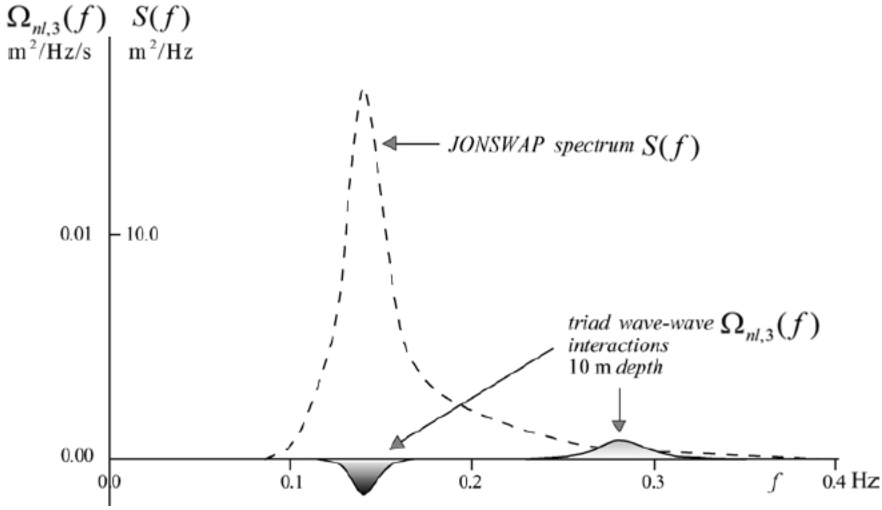

Figure 5.6: The energy distribution due to triad wave-wave interactions for a JONSWAP spectrum in shallow water, where energy is transferred to higher frequencies. $H_s = 3.5m$ and $T_{peak} = 7s$, Holthuijsen (2007)

.

5.7 Energy dissipation Ω_{ds}

The source term due to dissipation of energy can be divided into three components

$$\Omega_{ds} = \Omega_{wc} + \Omega_{bfr} + \Omega_{surf} \tag{5.6}$$

where Ω_{wc} is due to *white-capping*, Ω_{bfr} is due to *bottom friction* and Ω_{surf} is due to depth induced wave breaking (*surf-breaking*).

White-capping

White-capping is breaking due to wave steepness, and occurs also in deep water. Wave steepness is given by, Myrhaug (2006):

$$s = \frac{H}{\lambda} = \frac{2\zeta_a}{\lambda} \tag{5.7}$$

As shown in **Section 2.1**, the wave length is decreased and the wave amplitude is increased as the wave propagates to shallower water. This means that the wave steepness increases and occurrence of white-capping will have a larger effect on dissipation of energy compared to deep water. The dissipative source term due to white-capping is assumed proportional to the initial wave spectrum, and will thus have the same shape as the spectrum, but with negative values, as the energy is dissipated and not generated, Holthuijsen (2007), see **Figure 5.7**.

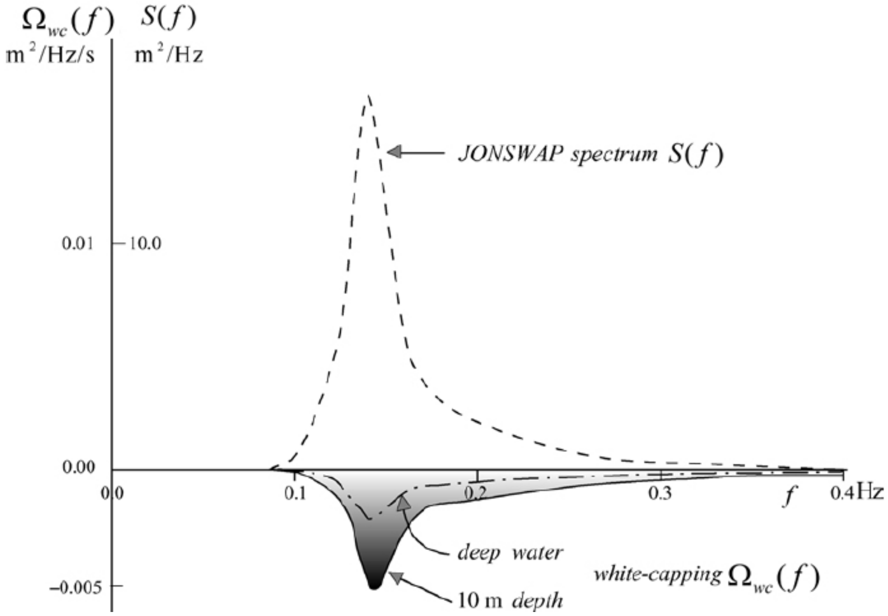

Figure 5.7: Source term due to white-capping. It is assumed proportional to the wave spectrum and it s effect is more pronounced in shallow water. $H_s = 3.5m$ and $T_{peak} = 7s$, Holthuijsen (2007)

.

Bottom friction

The source term due to bottom friction describes the dissipation of energy due to the complicated turbulent boundary layer at the sea bottom, created by the wave-induced water particle motion. Energy is transferred from the water particles to the turbulent motion in the boundary layer. The magnitude of the bottom friction dissipation is dependent on the sea bottom roughness and the particle velocity near the bottom and is assumed proportional to the wave spectrum, Holthuijsen (2007). As the wave induced water particle motion is negligible for high frequencies, the source term for bottom friction dissipation is also very small for high frequencies. No further detail will be given on this, but the general character of the bottom friction source term in given in **Figure 5.8**

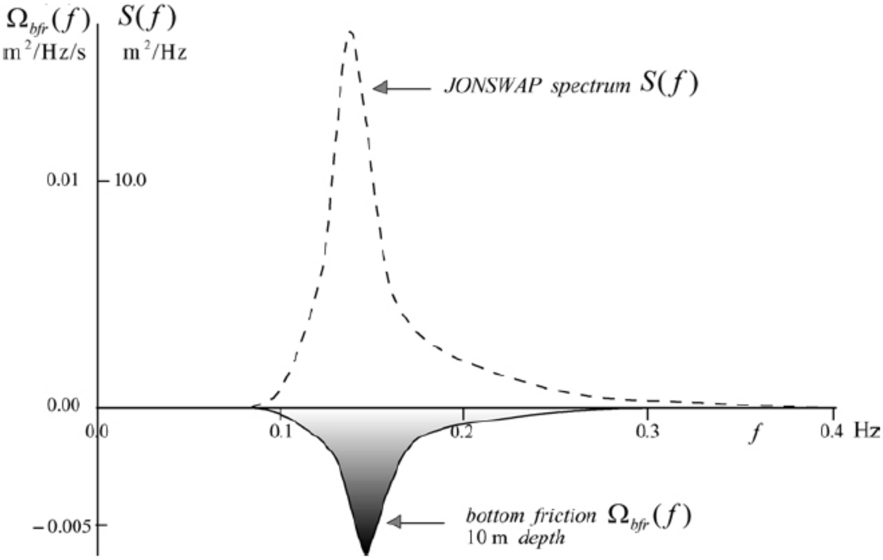

Figure 5.8: Source term due to bottom friction. $H_s = 3.5m$ and $T_{peak} = 7s$, Holthuijsen (2007)

.

Surf-breaking

The source term representing energy dissipation due to depth induced braking of waves, or *surf-breaking*, is illustrated in **Figure 5.9**. The source term is assumed proportional to the wave spectrum, as for the white-capping, but this dissipation term only take into account the breaking of waves due to the reduced water depth.

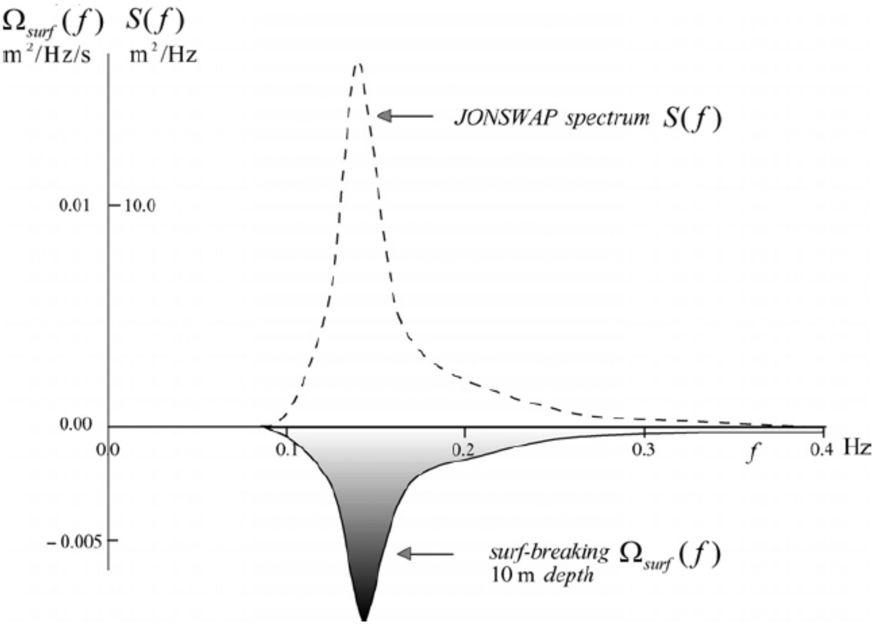

Figure 5.9: Source term due to surf-breaking of waves. $H_s = 3.5m$ and $T_{peak} = 7s$, Holthuijsen (2007)

.

The different source terms and how they generate, transfer and dissipate energy to the wave spectrum have now been presented. The total effect of these source terms is summarized in **Figure 5.10**.

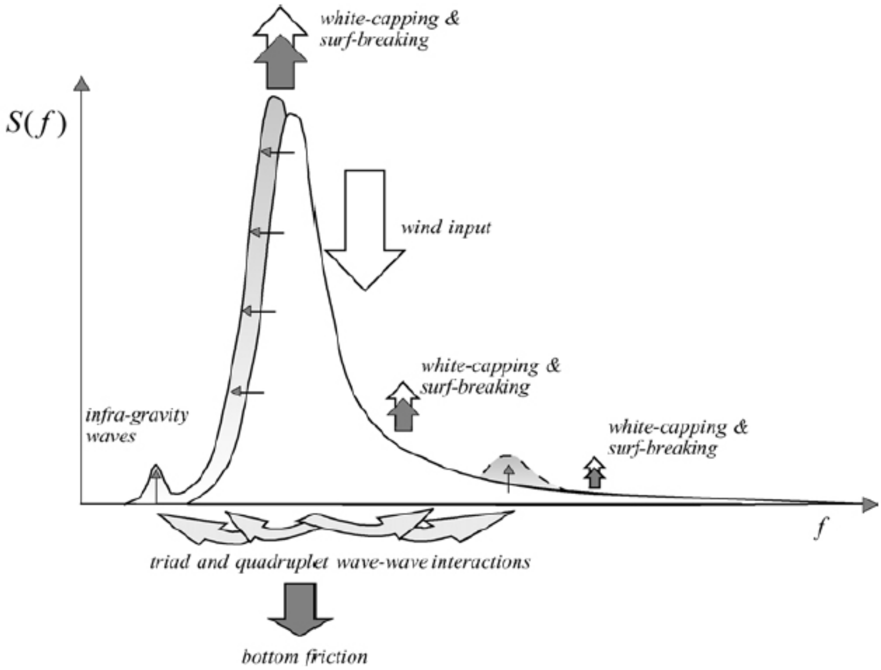

Figure 5.10: The total effect of the source terms on the incident wave spectrum, Holthuijsen (2007)

5.8 Computer models for computing spectral transformations

The previously mentioned transformations of the incident wave spectrum can be computed (or estimated) using existing computer models. Two of such computer models will briefly be mentioned here.

5.8.1 The SWAN wave model

The Swan model ((**S**imulating **WA**ves **N**ear Shore), from the Delft University of Technology) is a freely available, open-source, third-generation wave model for obtaining realistic estimates of wave parameters in coastal areas from given wind, bottom and current conditions, SWAN (2006). The model is based on solving the wave action balance equation given in **Equation 5.2** with sources and sinks.

The Swan model simulates wave propagation in time and space. Bottom- and current- induced shoaling and refraction is properly accounted for, but diffraction only approximately. Dissipation due to white-capping, bottom dissipation and surf-breaking are also accounted for by various models, and so are the quadruplet and triad wave-wave interactions.

The user specifies parameters like the initial wave spectrum, wind, bathymetry, grid, time dependency, output locations and output quantities (such as resulting wave spectrum).

5.8.2 The STWAVE wave model

Stwave (**ST**eady State Spectral **WAVE**) is an easy-to-apply, flexible, robust, half-plane (waves propagating in a half circle of 180-deg) model for near shore wind-wave growth and propagation, developed by the Coastal & Hydraulics Laboratory of the US Army Corps of Engineers. This model is also freely available for download.

The purpose of applying Stwave is, as for the Swan model, to quantify the change in wave parameters (wave height, period, direction, and spectral shape) between the offshore and the near shore. It is based on the following assumptions:

a) A mild bottom slope and negligible wave reflection
b) The input spectrum is constant along the offshore boundary
c) Steady-state waves, currents and winds
d) Linear refraction and shoaling
e) Depth uniform current
f) Negligible bottom friction
e) Depth uniform current
e) Linear radiation stress

6. The Design Wave Approach

When designing an offshore structure, the characteristic loads must be determined. The loads of interest in this thesis will be the wave induced loads. The wave conditions which are to be considered for structural design purposes, may be described by either *stochastic methods* (for nominal loading conditions), or by deterministic *design wave methods* (for the extreme loading conditions).

For dynamically behaving structures, i.e. the mass and drag term in the equation of motion *cannot* be neglected, stochastic modeling of the sea surface and its kinematics by time series is required. Examples of platforms where a full dynamic analysis is recommended are jackets in water depths exceeding 150m and most jack-ups in water depth lager than approximately 70-80m Haver (2011b).

For quasi-static structures, i.e. where the mass and damping term can be neglected in the equation of motion (resulting in $x\left(t\right)=\frac{F(t)}{k}$), the deterministic design wave method is sufficient. Quasi-static structures can, as a rule of thumb, be assumed to have a largest natural period of less than 2s, which is typically the case for all jackets up to a water depth of about 150m, Haver (2011b). Even though the largest natural period is somewhat larger than 2s, the design wave method is assumed to be adequate in calculating the quasi-static response.

The offshore wind turbine foundations in mind will consist of jacket structures in up to 50 m water depth, and the largest natural period is assumed to be much lower than the period of energetic forcing. With this assumption, dynamics can be neglected, and the *deterministic design wave approach* can be applied. To which extent dynamics *should* be accounted for and how a proper effect of dynamics should be estimated, can be indicated by studying the dynamic amplification factor, Haver (2011b).

An outline of the design wave approach is given in Sarpkaya and Isaacson (1981). When the analysis of the extreme loading condition is based on a design wave, the deterministic wave parameters such as wave height, period and direction is chosen statistically, see **Section 7**. An appropriate wave theory is then chosen (see **Chapter 4**), and the fluid velocities and accelerations along the axis of each structural element is calculated for each time step specified, as the wave is acting on the structure, see chapter **Chapter 11**. The wave is assumed to be long crested and to propagate with a constant shape and speed. The instantaneous sectional force is calculated through the use of Morison's equation, and is then integrated to get the force on each element. The forces are then summed to get the total force and overturning moment on the whole structure.

According to DNV (2011), the design of offshore wind turbine structures in ultimate limit state[1] is based on the characteristic load effect with a return period of *50 years.* How to statistically obtain the properties of the design wave at the site of interest will be presented in the following chapters.

---

[1] Corresponds to the limit of the load-carrying capacity, i.e. to the maximum load-carrying resistance DNV (2011)

7. Determining the 50-year Sea State

Hindcast data of the significant wave height and corresponding spectral peak period is available for the north sea (NORA10 from the Norwegian Institute of Meteorology[1]). In principal we can from this data establish the long term distribution for the individual wave height from the following expression

$$F_H(H) = \int\limits_{H_{m0}} \int\limits_{T_p} F_{H|H_{m0}T_p}(H|\, H_{m0}, T_p) \cdot ... \\ f_{H_{m0}T_p}\left(H_{m0}, T_p\right) w\left(H_{m0}, T_p\right) dH_{m0} dT_p \tag{7.1}$$

where $F_{H|H_{m0}T_p}(H|\, H_{m0}, T_p)$ is the conditional cumulative probability distribution of individual wave heights given the significant wave height H_{m0} and the spectral peak period T_p. $f_{H_{m0}T_p}\left(H_{m0}, T_p\right)$ is the joint probability density function of H_{m0} and T_p and $w\left(H_{m0}, T_p\right)$ is a weighting factor taking the variability of the wave frequency within each sea states into account, Myrhaug (2007). $F_{H|H_{m0}T_p}(H|\, H_{m0}, T_p)$ will be given by an analytical wave height distribution, and $f_{H_{m0}T_p}\left(H_{m0}, T_p\right)$ and $w\left(H_{m0}, T_p\right)$ are established from the hindcast data.

By solving $1 - F_H(H) = \frac{1}{N}$ by numerical integration, where $F_H(H)$ is given by **Equation 7.1** and N is the number of individual waves during 50 years, the wave height exceeded *once* during 50 years can be calculated (the 50-year wave height).

According to Sverre Haver, the grid resolution used in the NORA10 hindcast model is believed to be too coarse to give accurate results for H_{m0} and T_p, when the wave depth is as small as for the Dogger Bank Zone. This means that the effects of decreasing water depth may not properly be taken into account. Due to this, we do not have reliable data to perform the analysis outlined above at the area of interest.

---

[1] The NORA10 hindcast data contains estimated values for the wind speed, wind direction, significant wave height, peak period and mean wave direction for every 3 hours from September 1^{st} 1957 to December 12^{th} 2011

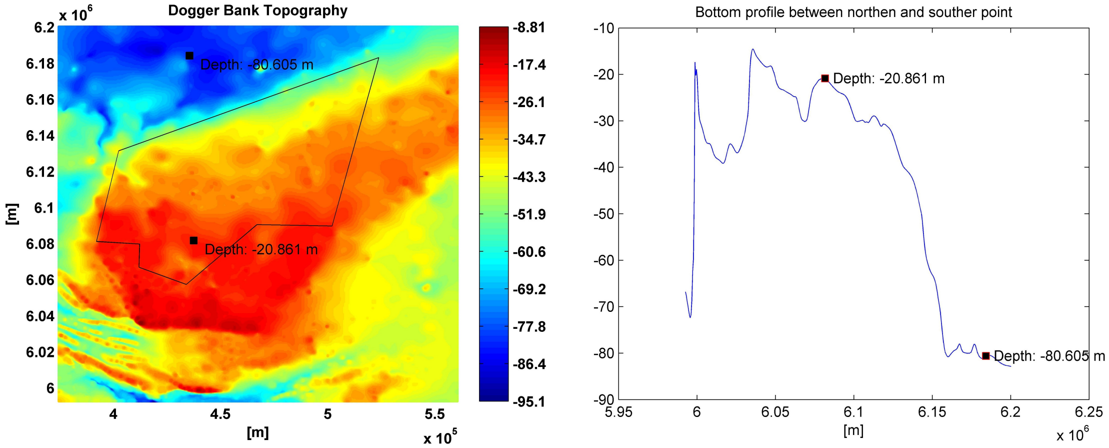

Figure 7.1: (Left:) Dogger Bank bathymetry and location of two positions where hindcast data is available; one at the site of interest, and another north of the Dogger Bank Zone (black line). (Right:) Bottom profile between the two data point locations

By examining **Figure 7.1**, it is seen that the water depth is greater north of the Dogger Bank Zone, and the hindcast model from the Norwegian Institute of Meteorology is believed to give good results for H_{m0} and T_p in this area. NORA10 data is available at the northern point in **Figure 7.1** where the local water depth is 80.6m. This point is in the rest of this thesis referred to as *the northern point*. The area where offshore wind turbines may be installed (the Dogger Bank Zone) is illustrated by the polygon on the figure. A point in the southern part of the Dogger Bank Zone, 102.5km south of the northern point, has been chosen as the potential location of offshore wind turbine installation. This point, where the water depth is 20.9m, will in the rest of this thesis be referred to as *the southern point* or *the location of interest*.

As the NORA10 hindcast is believed to yield credible data for H_{m0} and T_p at the northern point, the 50-year *sea state* can be estimated at the northern point based on this data. This can, according to DNV (2010a) be done by applying the *environmental contour* concept.

The *environmental contour* concept represents a rational procedure for determining an extreme sea condition, which means determining the (H_{m0},T_p) which corresponds to m-year probability of return. This is done by taking the joint probability density function of H_{m0} and T_p

$$f_{H_{m0}T_p}\left(H_{m0},T_p\right)=f_{H_{m0}}\left(H_{m0}\right)f_{T_p|H_{m0}}\left(T_p|\,H_{m0}\right) \tag{7.2}$$

and transforming it into a *standard normalized U-space*

$$\begin{aligned}\Phi\left(u_1\right) &= F_{H_{m0}}\left(H_{m0}\right) && (7.3)\\ \Phi\left(u_2\right) &= F_{T_p|H_{m0}}\left(T_p|\,H_{m0}\right) && (7.4)\end{aligned}$$

where Φ is the standard normal cumulative distribution function (zero mean and unit variance), and the uppercase F denotes cumulative distribution function. The advantage of this, is that the contours of constant probability of return will lie on a circle of radius β defined by

$$\sqrt{{u_1}^2+{u_2}^2}=\beta=-\Phi^{-1}\left(\frac{1}{N_m}\right) \tag{7.5}$$

where

$$u_1 = \Phi^{-1}\left(F_{H_{m0}}\left(H_{m0}\right)\right) \tag{7.6}$$
$$u_2 = \Phi^{-1}\left(F_{T_p|H_{m0}}\left(T_p|\,H_{m0}\right)\right) \tag{7.7}$$

N_m is the estimated number of sea states during m years given by

$$N_m = \frac{n_{obs} \cdot m[years]}{m_{obs}[years]} \tag{7.8}$$

where n_{obs} is the number of "observed" sea states in the specified direction, and m_{obs} is the number of years the data extend over. When the circle of constant probability of return in the U-space is known, the circle can be transformed back to the H_{m0},T_p-space by

$$H_{m0} = {F^{-1}}_{H_{m0}}\left(\Phi\left(u_1\right)\right) \tag{7.9}$$
$$T_p = {F^{-1}}_{T_p|H_{m0}}\left(\Phi\left(u_2\right)\right) \tag{7.10}$$

This is illustrated in **Figure 7.2**, which also shows that the parameters of the m-year sea state $H_{m0,m}$ and $T_{p,m}$ are assumed to be determined by the (H_{m0},$T_{p,m}$)-pair corresponding to the *peak of the contour line.*

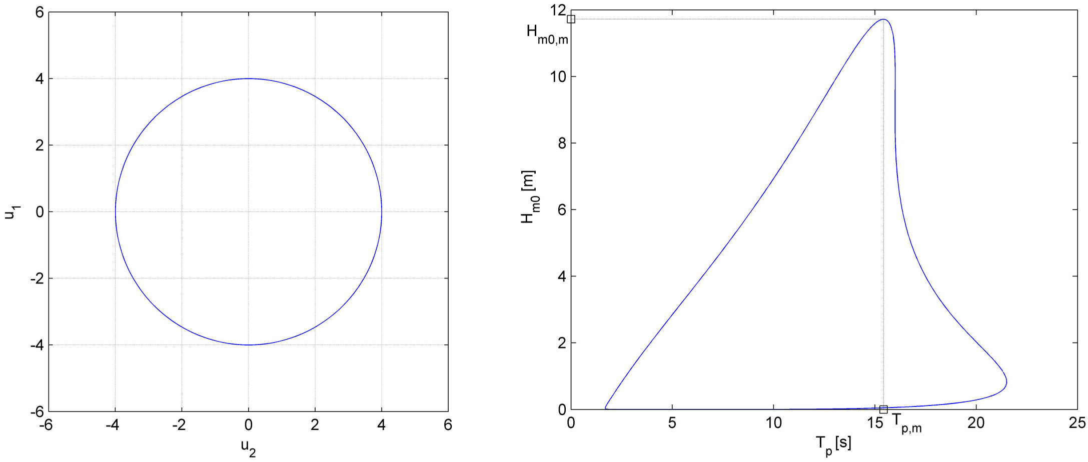

Figure 7.2: Example of transforming the contour line of constant probability of return from the Gaussian space (left) to the physical space (right). The m-year sea state parameters are determined from the peak of the contour.

The procedure outlined above requires the cumulative distribution of the significant wave height $F_{H_{m0}}\left(H_{m0}\right)$ and the conditional cumulative distribution of peak period $F_{T_p|H_{m0}}\left(T_p|\,H_{m0}\right)$ to be known. These are estimated from the hindcast data at a point north of the Dogger Bank Zone, organized in a scatter diagram.

7.1 Estimating the cumulative distribution $F_{H_{m0}}(H_{m0})$

DNV (2010a) refers to two methods for estimating the cumulative distribution $F_{H_{m0}}(H_{m0})$, namely the *initial distribution method*, where all available data is utilized, or the *Peak Over Threshold (POT) method*, where a distribution is fitted to the peak values within each storm above a given threshold h_0.

When all available data for the significant wave height is utilized, there must be a natural correlation between adjacent data points. This means that the values are not strictly independent, but as *all the data* is taken into account, uncertainty is reduced. The peaks within each storm is, however, independent, but fewer, which again increases uncertainty. Both the initial distribution method and the peak over threshold method has been performed and compared in the following.

7.1.1 Initial distribution method

The following calculations have been performed by the self-developed MATLAB script *long_term_analysis.m*.

According to Myrhaug (2007) and DNV (2011), the *upper tail*[2] of the long term cumulative probability distribution of the arbitrary significant wave height H_{m0} is given by a Weibull distribution[3]

$$F_{H_{m0}}(H_{m0}) = 1 - \exp\left[-\left(\frac{H_{m0}}{\rho}\right)^{\beta}\right] \tag{7.11}$$

where β and ρ are constants.

By taking the logarithm of both left and right hand side of **Equation 7.11** twice we get

$$\ln\left[-\ln\left(1 - F_{H_{m0}}(H_{m0})\right)\right] = \beta\ln\left(H_{m0}\right) - \beta\ln\left(\rho\right) \tag{7.12}$$

If we now introduce $y = \ln\left[-\ln\left(1 - F_{H_{m0}}(H_{m0})\right)\right]$, $x = \ln\left(H_{m0}\right)$ and $c = -\beta\ln\left(\rho\right)$ we see that, if the values are really Weibull distributed, in an x-y-coordinate system the long term cumulative distribution of the significant wave height becomes a straight line, i.e. $y = \beta x + c$. A plot with such x- and y-axis is called a Weibull probability paper.

As the true underlying distribution $F_{H_{m0}}(H_{m0})$ is unknown, it is more reasonable to plot the expected value of the probability distribution $E\left[F_{H_{m0}}(H_{m0})\right]$. It can, according to Leira et al. (2010), be shown that a uniformly distributed population has the following mean value

$$E\left[F_{H_{m0}}(H_{m0})\right] = \hat{F}_{H_{m0}}(H_{m0}) = \frac{n_{H_{m0}}}{n+1} \tag{7.13}$$

where $n_{H_{m0}}$ is the number of observations *less or equal* to H_{m0} and n is the total number of observations. The *hat* in $\hat{F}_{H_{m0}}(H_{m0})$ denotes that the value has been *estimated.*

The values of **Equation 7.13** can easily be calculated from a scatter diagram, containing the hindcast data from the northern point in **Figure 7.1**. Before constructing the scatter diagram, one first has to decide which sea state wave directions to consider. In this case, it has been decided to include the sea states with a mean wave direction of 330-15 degrees, see **Figure 7.3**.

---

[2] The upper tail is really what is of interest because we are interested in the largest H_{m0} of the contour line

[3] The significant wave height may also be modeled by a three-parameter Weibull distribution. Details on this will not be given.

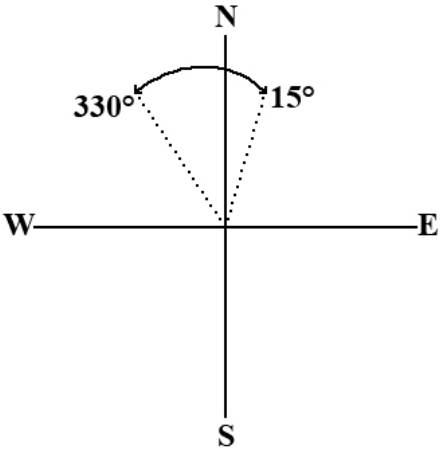

Figure 7.3: Mean wave direction of sea states included in the scatter diagram. N,S,E,W denotes North, South, East and West. Waves traveling directly from north will have a direction of 0 or 360 degrees

The mean wave direction is the mean direction of witch the waves are traveling **from**. This specific choice is based on the assumption that the largest storms will originate from north of the Dogger Bank Zone. The goodness of this assumption is assessed in **Section 8.1.1**.

The scatter diagram has been constructed by counting the number of sea states within specific ranges of H_{m0} and T_p, and can be viewed in **Appendix B**.

When the values of $\hat{F}_{H_{m0}}(H_{m0})$ was calculated, they were plotted in a Weibull plot (the corresponding H_{m0} values are found by calculating the average H_{m0} within each H_{m0} range in the scatter diagram). To fit a straight line to the data points, one first has to decide where the *tail* of the distribution starts, as only the tail of the distribution will follow a Weibull distribution. This decision is somewhat arbitrary, as one has to graphically decide at which point the data points are aligned in a straight line. In this case the data seems to give a good fit to the Weibull distribution for $H_{m0} > 4.79m$, see **Figure 7.4**. The least square fit is done by utilizing the built-in MATLAB function *fit*, which estimated $\hat{\beta} = 1.227$ and $\hat{\rho} = 1.719$ in **Equation 7.11**.

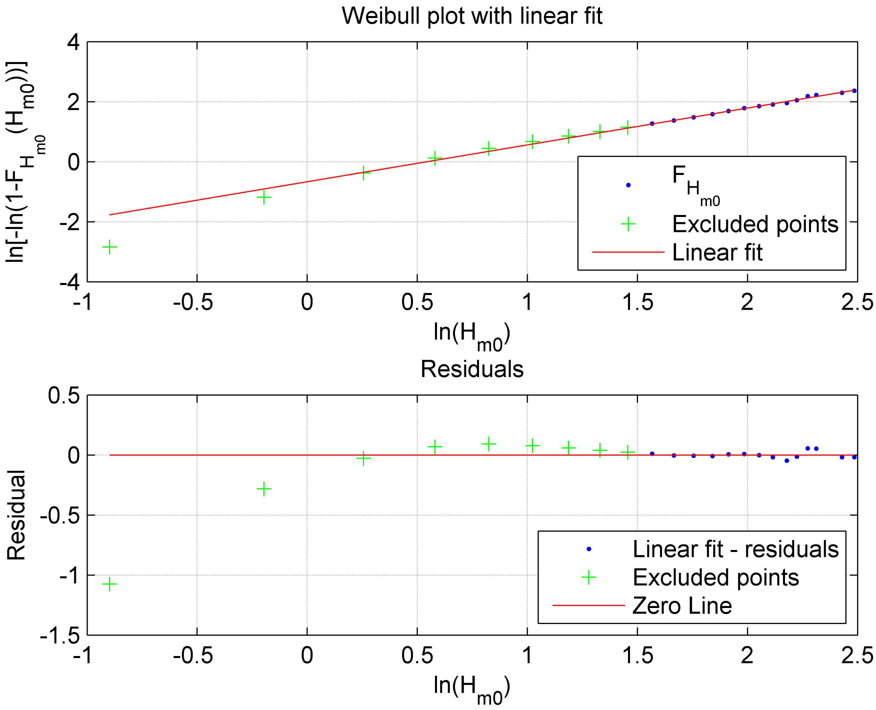

Figure 7.4: (Top): Least square fit of Weibull distribution to hindcast data. (Bottom): Visualization of the goodness of the fit by showing the point wise residuals

When knowing the values of $\hat{\beta}$ and $\hat{\rho}$, we know the estimated long term distribution of the significant wave height. The 50-year significant wave height can then easily be estimated by solving the equation

$$1 - F_{H_{m0}}(H_{m0}) = \frac{1}{N_m} \tag{7.14}$$

where $F_{H_{m0}}(H_{m0})$ is given in **Equation 7.11** with the values obtained for $\hat{\beta}$ and $\hat{\rho}$, and N_m is given in **Equation 7.8** with $m = 50[years]$. The number of years which the hindcast expands over is $m_{obs} \approx 54.3$ years (from September 1957 to December 2011). The estimated 50-year significant wave height was then found to be $H_{m0,50} = 11.74$m.

The effect of number of observations

Intuitively it is of great importance to have data from a long period of time, for the distribution to properly describe the underlying stochastic variable, H_{m0}. To study the effect of duration of the available time series on the estimated 50-year value of the significant wave height, $H_{m0,50}$ has been calculated based on different parts (of different length) of the available time series. The durations considered were 5, 10, 15, 20 and 25 years, and the result is presented in **Figure 7.5** and **Table 7.1**.

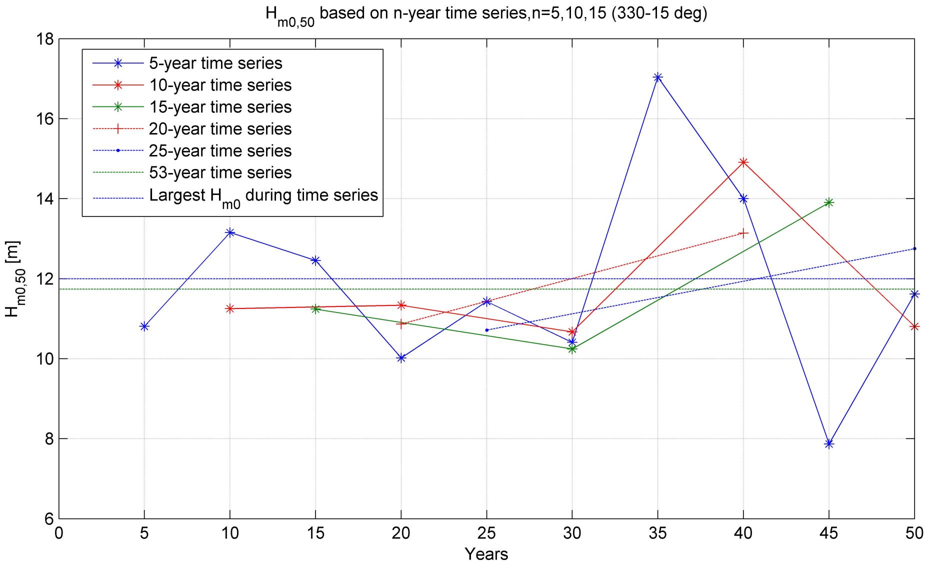

Figure 7.5: Effect of duration of time series on estimating the 50-year significant wave height. Durations of 5, 10, 15, 20 and 25 years have been considered, and compared to the largest value observed in the 54.3 year long time series (12 m), and the $H_{m0,50}$ based on the full time series (11.74 m). The first point of each graph is the $H_{m0,50}$ based on the firs n years of the full time series, the second point is the $H_{m0,50}$ based on the next n years and so on.

Table 7.1: Mean and standard deviation of $H_{m0,50}$ estimated from segments of different duration from the full 54.3 year long time series of H_{m0}

	Mean	Std
5-year time series	11.88	2.50
10-year time series	11.79	1.76
15-year time series	11.80	1.89
20-year time series	12.00	1.61
25-year time series	11.73	1.44

From **Figure 7.5** and **Table 7.1** it is seen that the average value of $H_{m0,50}$ is close to the value obtained from the full time series, although somewhat more conservative for durations smaller or equal to 20 years. It is also seen that for the shortest duration (5 years) the standard deviation is large and is decreased with increased duration. It should be noted that the standard deviation of $H_{m0,50}$ based on the 20 and 25 years time series are calculated from only two values.

By evaluating the values of the estimated $H_{m0,50}$ based on the ten 5-year time series, it is seen to increase significantly from year 30 to year 35. From further investigation it is found that the largest storm in the full 54.3 year time series is found in this time range, and is the reason for this increase. To examine how sensitive the predicted 50-year value of the significant wave height is to extreme events when calculated from the full time series, $H_{m0,50}$ was calculated with the largest value *removed* from the time series. This resulted in $H_{m0,50}$=11.39, or a decrease of 3% from what was obtained from the full time series.

7.1.2 Peak over threshold (POT) method

The following calculations have been performed by the self-developed MATLAB script *POT2.m*.

To best compare the result obtained from the initial distribution method with the result from a POT analysis, a threshold level of the POT analysis was set to $h_0 = 4.79m$, as the initial distribution method fitted the distribution for $H_{m0} > 4.79m = h_0$. This resulted in 308 peaks above $H_{m0} = h_0$, which is considered adequate to perform the analysis. Some of the peaks are illustrated in **Figure 7.6**.

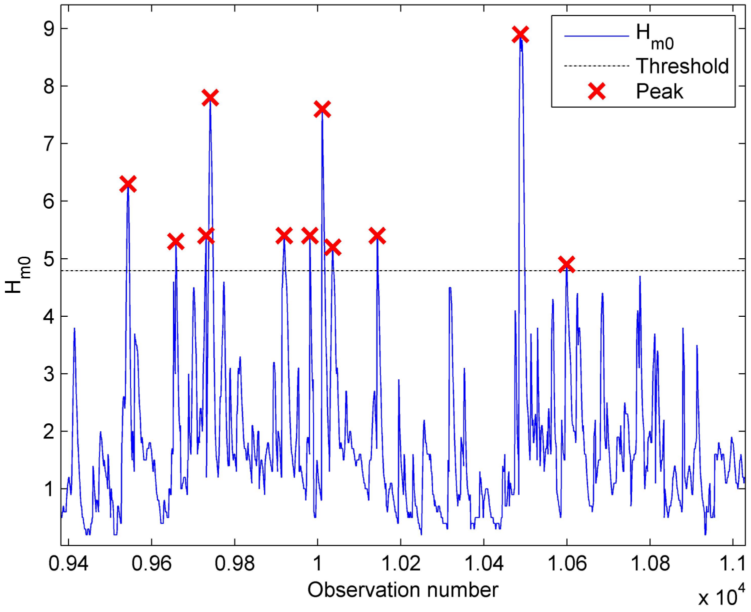

Figure 7.6: Visualization of some of the peaks over the threshold of $h_0 = 4.79$m from the hindcast data

DNV (2010a) recommends fitting either a 2-parameter Weibull distribution or an Exponential distribution to the stochastic variable

$$Y = H_{m0} - h_0 \tag{7.15}$$

where H_{m0} here denotes the *peak values* of the significant wave height above the threshold level.

To do this, the Method of Moments (MOM) was chosen to fit the distributions to the data. For the Weibull distribution, this is, according to Leira et al. (2010), done by solving the following equation system

$$\hat{\rho}_Y \Gamma \left(1 + \frac{1}{\hat{\beta}_Y}\right) = \bar{Y} \tag{7.16}$$

$$\hat{\rho}_Y^2 \left\{ \Gamma \left(1 + \frac{2}{\hat{\beta}_Y}\right) - \Gamma^2 \left(1 + \frac{1}{\hat{\beta}_Y}\right) \right\} = S_Y^2 \tag{7.17}$$

where $\hat{\rho}_Y$ and $\hat{\beta}_Y$ are the estimated parameters of the Weibull distribution, Γ is the gamma function given by $\Gamma(x) = \int\limits_0^\infty e^{-t} t^{x-1} dt$, and $\bar{Y}$ and S_Y^2 is the mean and variance of the stochastic variable Y given in **Equation 7.15**.

Equation 7.16 and **7.17** was solved numerically by first construction a table of the *coefficient of variance* CV for many values of the variable $\hat{\beta}_Y$, where

$$CV = \frac{\text{Variance}}{\text{Mean}} = \frac{\sqrt{\Gamma\left(1+\frac{2}{\hat{\beta}_Y}\right) - \Gamma^2\left(1+\frac{1}{\hat{\beta}_Y}\right)}}{\Gamma\left(1+\frac{1}{\hat{\beta}_Y}\right)} \tag{7.18}$$

Then the estimated $CV_{est} = \frac{S_Y}{\bar{Y}}$ was calculated, and the corresponding value for $\hat{\beta}_Y$ was found from the table. Then the value of $\hat{\rho}_Y$ was found solving **Equation 7.16**. The resulting values found from MOM were $\hat{\beta}_Y = 1.022$ and $\hat{\rho}_Y = 1.25$

To fit the data to the Exponential distribution by the MOM is less complicated, as the distribution is given by

$$F_Y^{\exp}(Y) = 1 - e^{-\lambda x} \tag{7.19}$$

The expected value is given by $\mathrm{E}[Y] = \frac{1}{\lambda}$, thus the moment estimator is given by

$$\hat{\lambda} = \frac{1}{\bar{Y}} \tag{7.20}$$

The resulting value was found to be $\hat{\lambda} = 0.81$.

To compare the Weibull fit and the Exponential fit, they have been plotted together with the data points in an Exponential plot, see **Figure 7.7**.

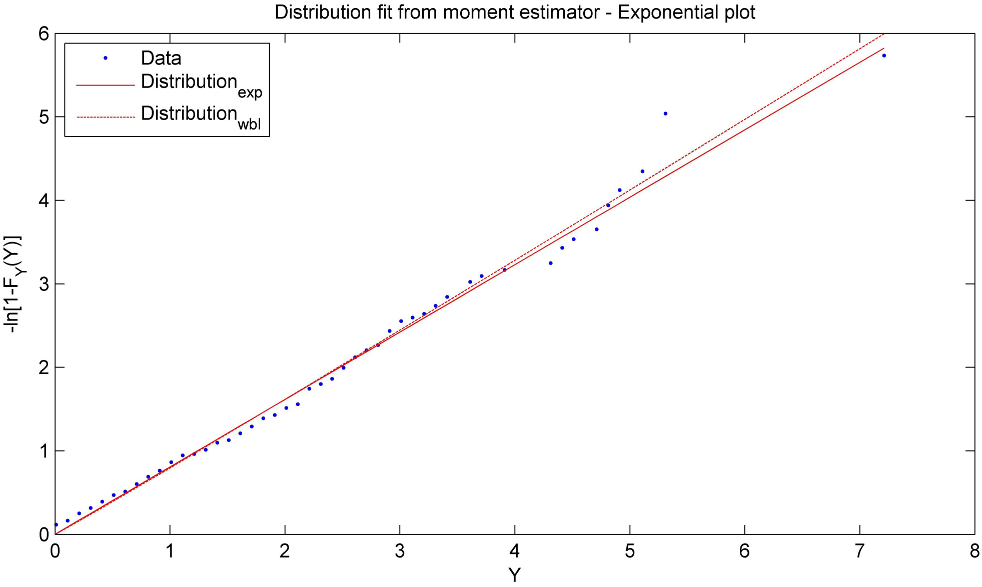

Figure 7.7: Comparison of Weibull and Exponential distribution to the POT data

By examining the two distributions in **Figure 7.7**, it is not clear which one is best representing the data. To investigate this further, 100 Monte Carlo simulations were performed to replicate the data points in the plot. This procedure is performed by creating as many random numbers (from 0 to 1) as there are data in the POT analysis, i.e. 308. Then 308 values for Y can be obtained by solving the expression for the Weibull distribution by inserting the random numbers for $F_Y(Y)$ and the estimated parameters for β and ρ (one could also have chosen the Exponential distribution, but the result would have been very similar). This is done 100 times (i.e. with 100 series of 308 random numbers), which gives 100 different data series who all are described by the same Weibull distribution. The result is represented in **Figure 7.8**

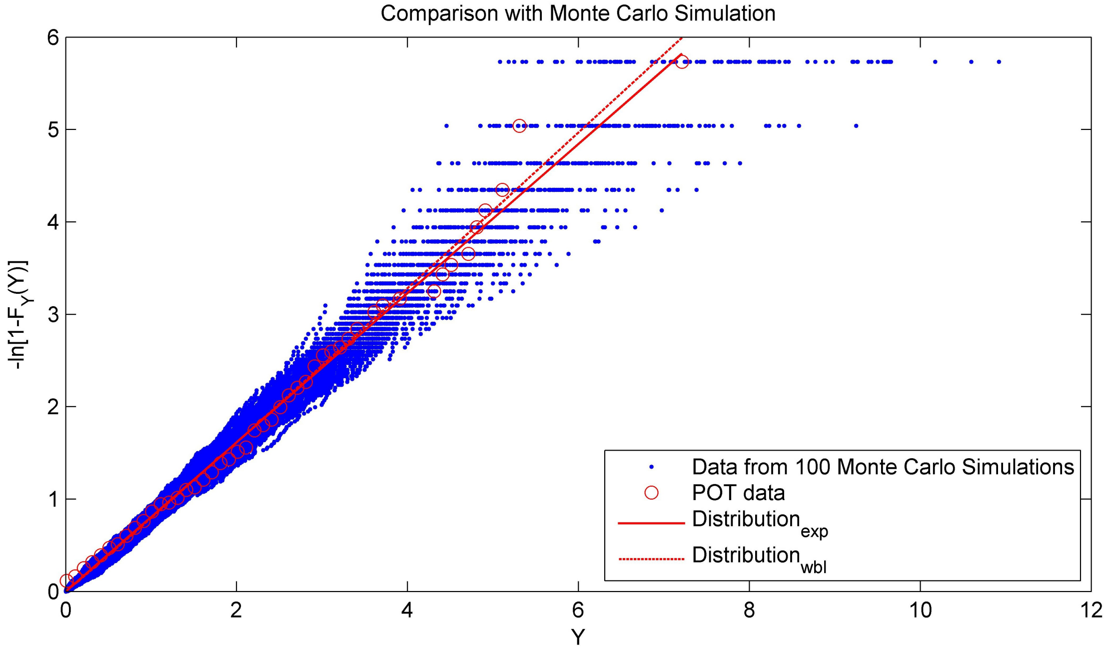

Figure 7.8: Comparison of the Weibull and Exponential distribution obtained from the POT analysis with data from 100 Monte Carlo simulations

By studying **Figure 7.8** we can see that both the Weibull and the Exponential distribution may represent the data from the POT analysis. However, the Weibull distribution will be used in the following calculations due to the fact that it has *two parameters*. It is assumed that a two parameter distribution has more flexibility in representing the data, compared to a one parameter distribution (i.e. the Exponential distribution).

Based on the Weibull distribution, the 50-year significant wave height obtained from the POT analysis is calculated from the following equation

$$1 - F_Y(Y) = \frac{1}{N_m} \tag{7.21}$$

where $F_Y(Y)$ is given in **Equation 7.11** with the POT values obtained for $\hat{\beta}$ and $\hat{\rho}$. The estimated 50-year value of Y was found to be $Y_{50} = 6.8m$. By inserting this in **Equation 7.15** with $h_0 = 4.79m$, it is found that the 50-year significant wave height is $H_{m0,50}^{POT} = 11.59m$.

This result is close to what was obtained from the initial distribution method, where the 50-year significant wave height was found to be 11.74m. It is observed that the result from the POT analysis is *less* conservative, which is why the distribution obtained from the initial distribution method will be used in further calculations.

7.2 Estimating the conditional cumulative distribution of spectral peak period $F_{T_p|H_{m0}}\left(T_p|\, H_{m0}\right)$

The following calculations have been performed by the self-developed MATLAB script *long_term_analysis.m*.

To determine the estimated conditional cumulative distribution for the spectral peak period, it is assumed to be modeled by a lognormal distribution, DNV (2010a). The probability density function is needed to estimate its parameters. The lognormal probability density function is given by

$$f_{T_p|H_{m0}}\left(T_p|\, H_{m0}\right) = \frac{1}{\sigma T_p\sqrt{2\pi}} \exp\left\{-\frac{\left[\ln\left(T_p-\mu\right)^2\right]}{2\sigma^2}\right\} \tag{7.22}$$

where the distribution parameters μ and σ are functions of H_{m0}. These parameters are given by

$$\mu = E\left[\ln\left(T_p\right)\right] \tag{7.23}$$

$$\sigma = std\left[\ln\left(T_p\right)\right] \tag{7.24}$$

So, by estimating μ and σ for each of the H_{m0}-classes containing sufficient number of observations in the scatter diagram, continuous functions are fitted to obtain $\mu\left(H_{m0}\right)$ and $\sigma\left(H_{m0}\right)$, Haver and Nyhus (1986). DNV (2010a) suggests

$$\mu\left(H_{m0}\right) = a_0 + a_1 H_{m0}^{a_2} \tag{7.25}$$

$$\sigma\left(H_{m0}\right) = b_0 + b_1 \exp\left(b_2 H_{m0}\right) \tag{7.26}$$

where a_i, b_i for $i = 0, 1, 2$ are estimated from this fitting procedure.

From the scatter diagram in **Appendix B**, the fitted functions in **Figure 7.9** were obtained.

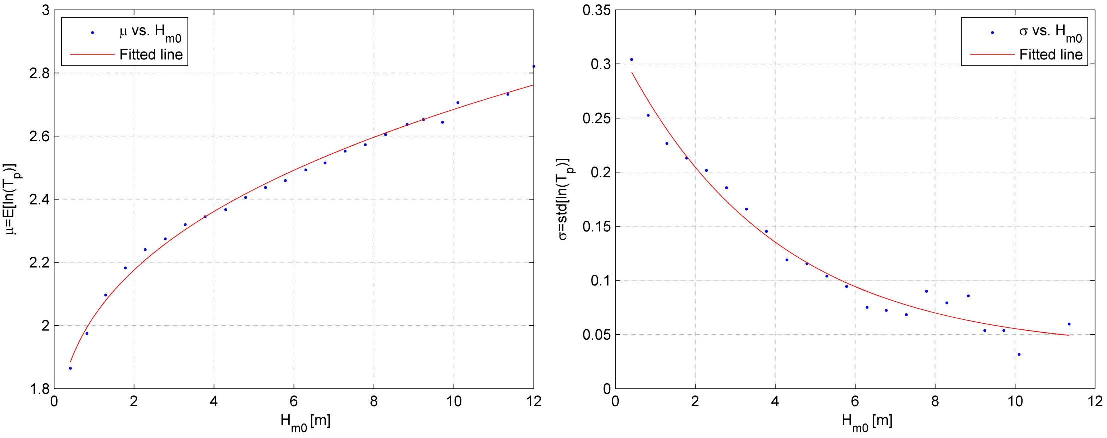

Figure 7.9: Fitted functions of the parameters μ and σ for the conditional cumulative distribution of the spectral peak period

The estimated values of the coefficients in **Equation 7.25** and **7.26** from the least square fit in MATLAB are presented in **Table 7.2**

Table 7.2: Values of the estimated coefficients in **Equation 7.25** and **7.26**

Coeff.	Value
$\hat{a}_0$	1.482
$\hat{a}_1$	0.547
$\hat{a}_2$	0.342
$\hat{b}_0$	0.035
$\hat{b}_1$	0.287
$\hat{b}_2$	-0.262

As μ and σ have been estimated, the conditional cumulative distribution is given by

$$F_{T_p|H_{m0}}\left(T_p|\,H_{m0}\right) = \Phi\left(\frac{\ln\left(T_p\right)-\mu}{\sigma}\right) \tag{7.27}$$

where Φ again is the standard normal cumulative distribution function.

Now both $F_{H_{m0}}\left(H_{m0}\right)$ and $F_{T_p|H_{m0}}\left(T_p|\,H_{m0}\right)$ have been estimated, and the environmental contour line corresponding to m-year return period can be determined as previously described. The result is presented in **Figure 7.10**

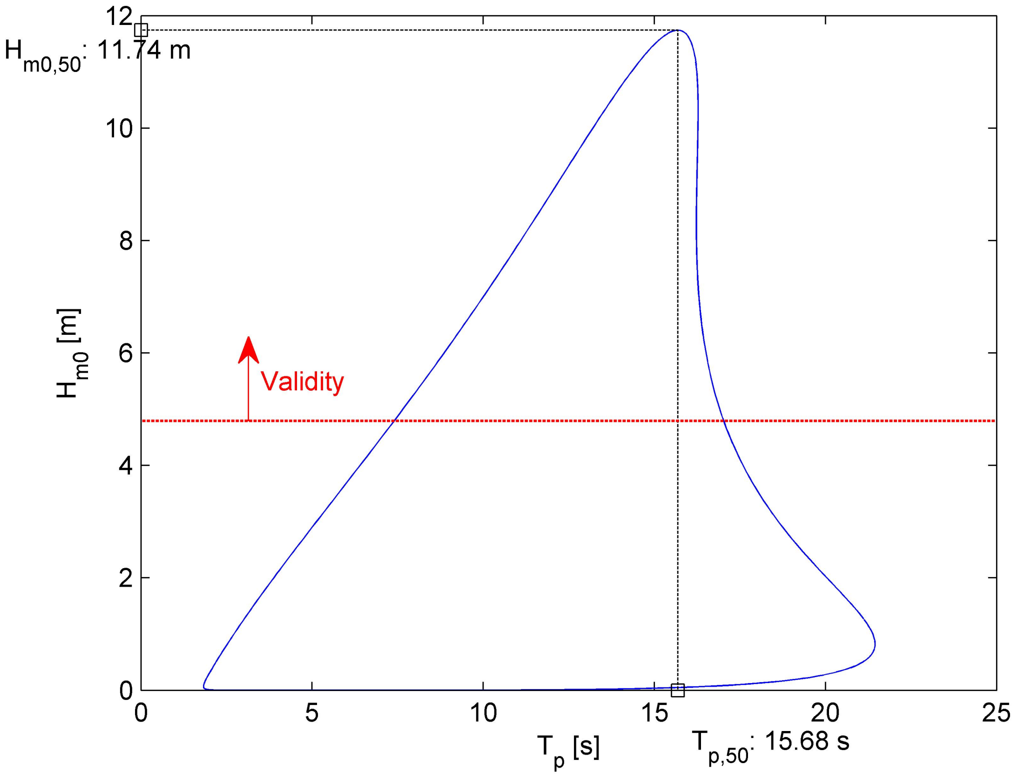

Figure 7.10: The 50-year contour of H_{m0} and T_p, and the 50-year sea state ($H_{m0,50}$,$T_{p,50}$). The valid part of the plot is also shown

It is emphasized that as the cumulative distribution of significant wave height $F_{H_{m0}}(H_{m0})$ has been estimated for $H_{m0} > 4.79$, the contour plot is also just representative for $H_{m0} > 4.79$, as shown by the red arrow in the figure above. Since the peak of the contour plot is what is of interest, the lack of validity below $H_{m0} = 4.79$ is not a problem.

From **Figure 7.10** it is seen that estimated parameters of the 50-year sea state is $H_{m0,50} = 11.74m$ and $T_{p,50} = 15.68s$ at the northern point, 102.5 km north of the site of interest.

8. Sea State Parameters at the Site of Interest

From **Chapter 5** it is known that the sea state is changed when propagating from the northern to the southern point at the Dogger Bank Zone. The change of the 50-year sea state obtained in **Chapter 7** will be calculated by the use of SWAN, a third-generation wave model briefly mentioned in **Section 5.8**, to obtain the 50-year sea state parameters at the southern point in **Figure 7.1**. This procedure will be explained later in this chapter, but first the change of the sea state from the northern to the southern point according to the hindcast data will be investigated.

8.1 Sea state development from northern to southern point according to hindcast data NORA10

As stated in **Section 7**, the hindcast data is believed to give accurate results north of the Dogger Bank Zone, but not at the site of interest. This is because the hindcast model is not believed to properly take the effects of such a small water depth into account. The hindcast model is, however, taking it into account in some sense, and this will be investigated further in this section.

As shown in **Figure 7.1**, hindcast data is available at two locations, at a point north of the Dogger Bank and at a point located in the Dogger Bank Zone. The water depth at the northern point is 80.6m and 20.9m at the site of interest, and the distance between the two points are 102.5km. To investigate how the sea states changes according to the hindcast data from the northern to the southern point, two plots have been constructed: the cumulative probability of the observations and a Q-Q plot[1] as shown in **Figure 8.1**. In this case *all wave directions* are considered.

---

[1] A Q-Q plot (or quantile-quantile plot) is easily constructed by sorting the data at the two locations in ascending order and plotting the values against each other

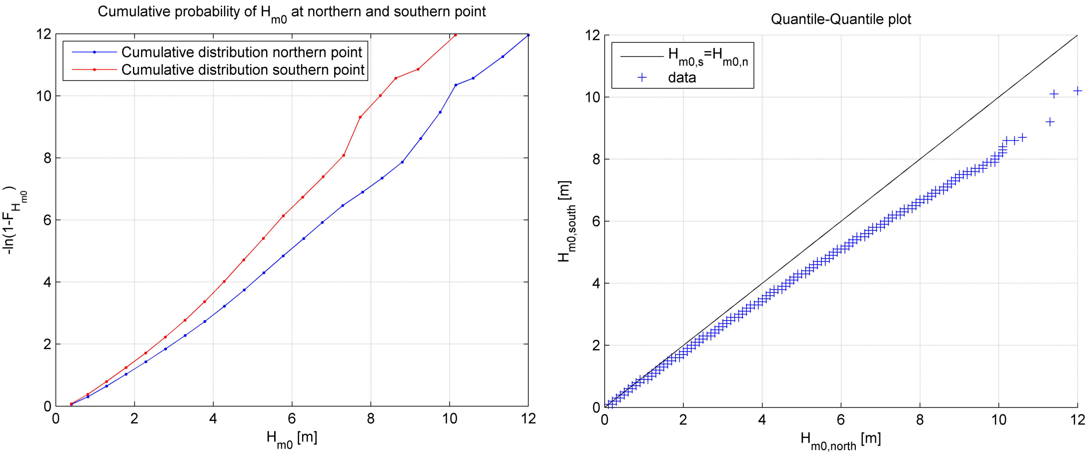

Figure 8.1: (Left:) The cumulative probability of significant wave height at the northern and southern locations plotted in an Exponential plot. (Right:) Quantile-quantile plot of the H_{m0} data at the northern and southern points

By evaluating the exponential plot of the cumulative distribution of H_{m0} in **Figure 8.1** it is seen that for all values of H_{m0}, there is a larger probability of exceedance $(1 - F_{H_{m0}})$ at the northern point, compared to the southern point. It is also seen that this effect is more pronounced for larger values of the significant wave height. This means that, as expected, the sea states are worse at the northern point.

From the Q-Q-plot it is seen that the when plotting the values of the significant wave heights at the northern point versus at the southern point, the data points are bent downwards compared to the $H_{m0,s} = H_{m0,n}$ line. This confirms that the values of the significant wave height are larger at the northern position.

As seen in **Section 5.7**, the dissipative effects will increase as the water depth decrease, which is why the decrease in significant wave height from the northern to the southern point is expected. From the results above it is seen that NORA10 takes these effects into account to some extent.

8.1.1 The largest storms

In addition to study *all* the values of H_{m0} and how it compares in the northern and southern point, the *largest* storms has also been considered. **Figure 8.2** shows the peak value of the significant wave height in the 30 worst storms in the northern position, and the corresponding value as the storm has traveled to the southern point.

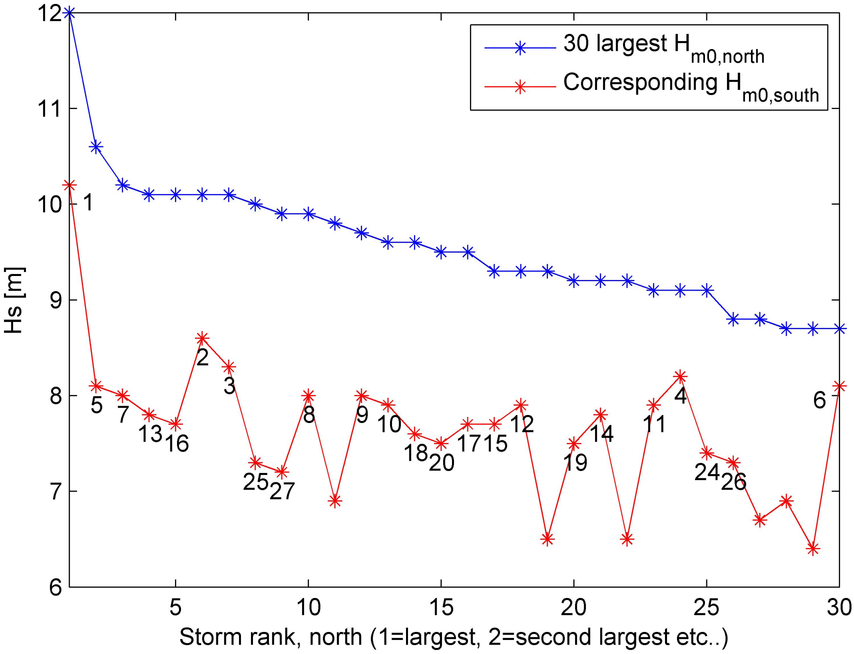

Figure 8.2: Peak significant wave height of the 30 largest storms in the northern point, and their corresponding values in the southern point. The value of $H_{m0,north}$ is in decreasing order from left to right. The numeric values next to each $H_{m0,south}$-point is its rank among all $H_{m0,south}$-values, i.e. the third $H_{m0,south}$-point is the seventh largest etc.

From this it is once again confirmed that the significant wave height is decreased from north to south, but it is observed that the values of H_{m0} is not *monotonically* decreasing at the southern point. In other words it is not clear if the 30 largest storms at the northern point corresponds to the 30 largest storms in the southern point. This has been further investigated, and the result is presented in the numeric values attached to each of the $H_{m0,south}$ data points. This value is the *rank* among the 30 largest storms at the southern position (those without a number is not among the 30 largest). From this is is seen that

- The 5 largest storms at the northern point is corresponding to 2 of the 5 largest storms at the southern point
- The 10 largest storms at the northern point is corresponding to 6 of the 10 largest storms at the southern point
- The 20 largest storms at the northern point is corresponding to 16 of the 20 largest storms at the southern point
- The 30 largest storms at the northern point is corresponding to 24 of the 30 largest storms at the southern point

From this it can be concluded that the worst storms at the northern point corresponds to the worst storms at the southern point, as expected.

When investigating how the 30 largest storms had developed from the northern to the southern point, it was also studied if any time delay could be traced from the two time series. By plotting the cross-correlation of the largest storms at the northern position and the corresponding storms at the south point (i.e. for the same time span), it was found that the maximum value of the cross-correlation function had its maximum at *zero time delay*, which means that no delay was found. As the distance between the two points is 102.5km, it seems unreasonable that there is no time delay. But from the time series it is found that the *mean peak period* of the 30 largest storms is T_p =13.2 s, which results in a mean peak group velocity of $c_{g,p} = \frac{g}{4\pi}T_p = 10.31\frac{m}{s}$ assuming deep water. This means that the 30 largest storms on average will use approximately 2.76 hours to travel from the northern to the southern point, which shows that the time resolution in the hindcast data of 3 hours is too course to capture this time delay.

Direction of the largest storms

As stated in **Section 7.1.1**, the worst storms are assumed to have a mean wave direction of 330-15 degrees. To investigate if this is a good assumption, **Figure 8.3** has been constructed. In this plot the wave direction of the 30 largest storms in the northern and southern point from the hindcast data has been is plotted. The median of the wave direction of the 30 largest storms have then been compared to the direction span of 330-15 degrees.

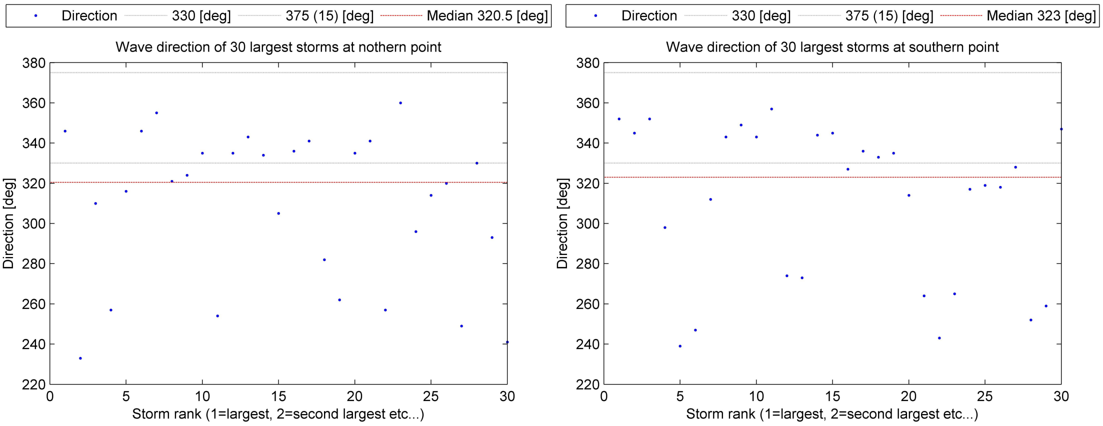

Figure 8.3: Mean wave direction of the 30 largest storms at the northern (left) and southern (right) position. The direction range 330-15 degrees and the median is also indicated

From the plots in **Figure 8.3** it is seen that for both the northern and southern point, the median wave direction of the 30 largest storms is *below* the lower limit of the direction range 330-15 degrees. This means that *less than half* of the 30 largest storms will be within the specified direction range. This might raise concerns that the fitting of the distribution of significant wave height is not based on the worst storms and thus resulting in non-conservative estimates of $H_{m0,50}$ at the northern point.

To investigate this further, a new estimate of $H_{m0,50}$ was performed (with the procedure outlined in **Section 7.2**), including all sea states with a mean wave direction of 220-15 degrees, which lead all the 30 largest storms to be included in the analysis. This resulted in $H_{m0,50}$=11.92m, which compared to the initial result of $H_{m0,50}$=11.74m is only 1.53% larger. As the increase is not larger, we can accept the initial assumption of the mean wave direction range of 330-15 degrees, as other uncertainties are believed to be of greater importance.

8.2 Obtaining sea state parameters $\hat{H}_{m0,50}$ and $\hat{T}_{p,50}$ at site of interest using the SWAN wave model

As mentioned in **Section 5.8**, the SWAN wave model solves the wave action balance equation as given in **Equation 5.2** to determine how the energy of a sea state changes in time and space. For the details on the different physical mechanism and numerical approaches, the keen reader is referred to SWAN (2011).

Before running the real problem (with the actual bathymetry and 50-year sea state etc.), SWAN was first run on a long crested and short crested *test case* to investigate how the wave model works, and how different physical effects influence the solution.

8.2.1 Using SWAN on a *test case* to better understand how the wave model works

This *test case* was taken from the Master Thesis of Svangstu (2011), where the wave elevation of irregular sea states were measured on a sloping bottom (constant slope of approximately 1:20) at MARINTEK, at a scaling factor of 81. The results from these tests were available which made comparison with results from SWAN convenient.

Svangstu (2011) presents various test setups with different sea states, but the following setup was chosen for comparing the results obtained from SWAN:

Table 8.1: Model test setup values from Svangstu (2011)

	Model Scale	Full Scale
H_s [m]	0.1289	10.5138
T_p [s]	1.25	11.25
Max depth [m]	0.83	67.23
Min depth [m]	0	0
Horizontal length of tank [m]	17	1377.187

The model test was performed with long crested waves, without wind, with a JONSWAP spectrum with a peakedness coefficient of 3.3.

When setting up the **stationary** SWAN analysis, the following had to be specified:

- The boundary condition (input wave spectrum)
- Output parameters and locations
- The bathymetry and size of the computational grid
- Which physical processes to be activated
- The mesh density of the computational domain
- The direction resolution
- The frequency range and resolution

After running the analysis, the results were compared to those obtained during the model test in Svangstu (2011).

Choosing the boundary condition

The input boundary condition chosen were a JONSWAP wave spectrum with peakedness coefficient 3.3 and $H_{m0} = 10.5138$m and $T_p = 11.25$s, which was chosen to be constant along the side of largest water depth (67.23m) of the computational domain, see **Figure 8.4**. The wave spectrum is 2-dimensional on the form

$$S(f,\theta) = S(f)D(\theta) \tag{8.1}$$

where f is the frequency in Hz, θ is the direction in degrees, $S(f)$ is the 1-dimensional wave spectrum (JONSWAP) and D(θ) is the directionality function. The directionality function is on the form

$$D(\theta) = A\cos^n(\theta - \theta_p) \text{ for } |\theta - \theta_p| \leqslant \frac{\pi}{2} \tag{8.2}$$

where n is the spreading coefficient controlling how much the waves are spread (spreading decreases with increasing n), θ_p is the main wave direction and A is chosen so that $\int\limits_{\theta} D(\theta) = 1$.

The spreading coefficient of the sea state was set to n=65 (the maximum value accepted by SWAN), to make the sea state approximately long crested. Alternatively SWAN could also have been run in 1D mode as $\frac{\partial}{\partial y} = 0$, but because the model also would be tested in short crested waves, the 1D-mode was not utilized.

The three other boundaries of the rectangular domain was chosen as water-water boundaries, i.e. no boundary conditions were specified (as the water depth was zero at one end, this is interpreted by SWAN as land, where all energy is absorbed).

Choosing the output parameters and locations

The main output parameters were chosen to be the significant wave height H_{m0}, and the spectral density $S(f)$. The location of the output points were chosen on a straight line along the x-axis from the deepest point (67.23m) to a depth of 15m, in the center line of the computational domain, i.e. at y=2500, see **Figure 8.4**. This corresponded to where the wave probes were placed in the model test in Svangstu (2011) for the results to be compared properly.

Choosing the bathymetry and size of the computational grid

The bathymetry was chosen to correspond with the model test in Svangstu (2011) with a constant sloping bottom from a depth of d=67.23m to a depth of d=0m, over a horizontal length of 1377.187m. The width of the bathymetry (in y-direction) was given as 5000m due to the reasons stated in the paragraph below. The bathymetry grid was defined as coarse as possible (only defined by the corner points), as the interpolation between these points would result in a correct bottom value due to the constant slope.

When specifying the computational grid (in this case uniform and rectangular) the location of its origin, extent in x- and y-direction and number of elements[2] in x- and y direction is taken as input in SWAN. The origin of the computational grid in the horizontal plane was chosen to be in (x,y)=(0,0) with $0 \leqslant x \leqslant 1377.187$ and $0 \leqslant y \leqslant 5000$, i.e. the computational grid covers the bathymetry, see **Figure 8.4**. The choice of the computational grid's extent in y-direction is based on the fact that no boundary condition is given along the water boundary at $y = 0$ and $y = 5000$, so SWAN assumes that no waves can enter the area, and that waves can leave these boundaries freely, SWAN (2006). In a short crested sea state this assumption contains errors which will propagate into the model and it is recommended to chose the location of these boundaries sufficiently far away from where reliable computations are needed. In this case the

---

[2] The number of elements define at how many points in the horizontal computational domain SWAN will solve the energy balance equation

waves were long crested, with the wave crest orthogonal to these boundaries, and the location of these boundaries are believed to be of less importance as no waves will propagate into the model at these boundaries. To be on the safe side, and to be able to use the same model in a short crested case, the output was taken 2500m away from these boundaries, i.e. at y=2500.

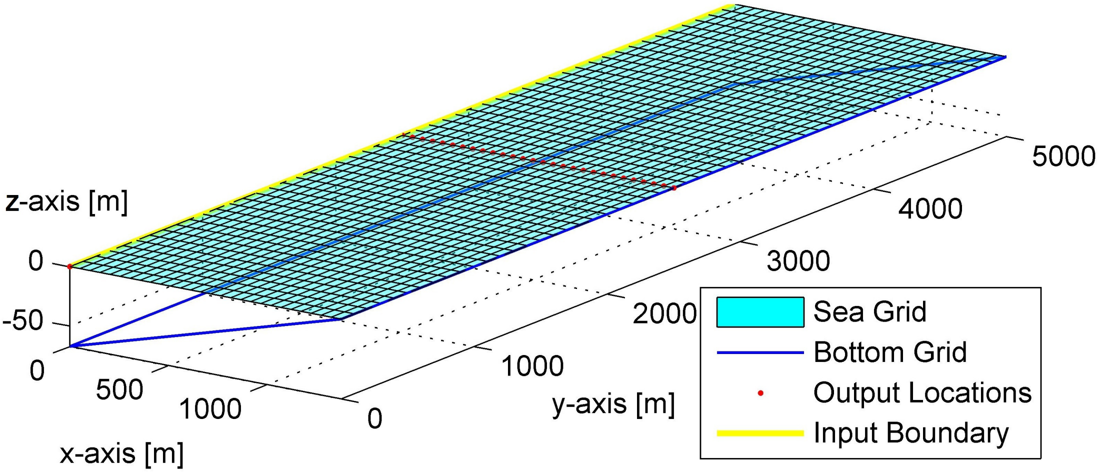

Figure 8.4: Grid, input boundary and locations plotted in Matlab for graphical presentation (Swan has no graphical interface)

Choosing which physical processes to be activated

The physical processes believed to give the most realistic result for the *long crested* test case were the *default* physical processes in Swan, except for the quadruplet wave-wave interactions. The *default* physical processes are bottom friction, surf breaking, refraction, white-capping, triad wave-wave interactions and quadruplet wave-wave interactions. Quadruplet wave-wave interactions were disabled in this test case as the approximation of this process is unreliable for long crested waves according to SWAN (2006). In the following sensitivity analysis of the mesh density and frequency resolution, the previously mentioned physical processes were enabled, except for quadruplet wave-eave interactions.

Choosing the mesh density of the computational domain

As the waves were long crested traveling in the positive x-direction, the number of elements in y-direction is of less importance and was somewhat arbitrarily chosen to be 50 (dy=100m), but the mesh density in x-direction will influence the solution. The effect of the number of elements in x-direction was tested by plotting the significant wave height as function of dimensionless water depth from d=67.23m to d=15m, as presented **Figure 8.5**.

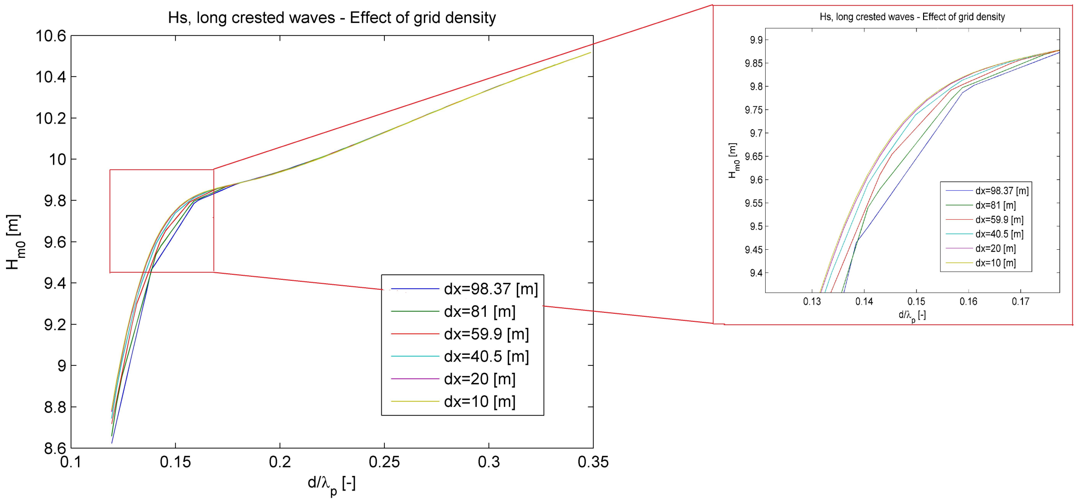

Figure 8.5: Effect of mesh density in x-direction in long crested test case

From **Figure 8.5** it is seen that the effect of the grid resolution in x-direction does not affect the result until the dimensionless water depth $\frac{d}{\lambda} \leqslant\sim 0.18$ (d$\approx$ 29m). It was found that dx=20m (69 elements in x-direction) was sufficient.

The frequency resolution was at this point chosen somewhat arbitrary, but in a way that the incident wave spectrum was rendered sufficiently (from a graphical evaluation). It was assumed that if, however, the initial chosen frequency density was not optimal, this would not have a critical effect on the result from the sensitivity analysis of the mesh density in x-direction, i.e. if a more optimal frequency resolution existed, the result of dx=20m was still valid.

Choosing the direction resolution

The direction range was chosen from 0 to 360 degrees, with 36 discrete directions, i.e. a resolution of 10 degrees. According to SWAN (2006), a resolution of 10 degrees is suitable for wind seas with a directional spreading of typically 30 degrees, but recommends a finer resolution for sea states with a narrower directional spreading. This may indicate that a finer resolution than 10 degrees was required for the long crested case, but by varying the direction resolution from 1 to 10 degrees it was found that it did not affect the solution. This confirmed that a direction resolution of 10 degrees was sufficient.

Choosing the frequency range and resolution

The frequency resolution, minimum and maximum spectral frequency also had to be specified. The frequency resolution was chosen by specifying the lowest frequency f_{low}, the highest frequency f_{high} and the number of frequencies $(1{+}n_{freq})$. The resolution is not constant, but distributed logarithmically where the frequency step Δf is determined from

$$\Delta f = \left(-1 + \left[\frac{f_{high}}{f_{low}}\right]^{\frac{1}{n_{freq}}}\right) f \tag{8.3}$$

where f_{low} and f_{high} is the lowest and highest frequency of the wave spectrum and $(1{+}n_{freq})$ is the number of frequencies from f_{low} to f_{high}. The frequency step determines how well the frequency is reproduced by SWAN.

With this logarithmic distribution of frequencies, the resolution is highest for the lower frequencies, and then decreasing with increasing frequency. Varying the values of f_{low}, f_{high} and n_{freq} has an effect on how the specified input spectrum was rendered. A bad choice of these parameters will result in different values of H_{m0} and T_p at the input boundary compared to what is specified in the input spectrum, because the spectrum will be rendered badly. The lowest value of f_{low} that SWAN accepted was 0.053 Hz, so this value was chosen for f_{low}. Comparing the two remaining parameters, n_{freq} clearly had the largest effect on how the spectrum was rendered. Choosing $(1{+}n_{freq}) \geqslant 80$ made the solutions dependence of f_{high} very small, so $(1{+}n_{freq})$ was set to 80 and f_{high} was set to 1 Hz. This resulted in the spectrum at the input boundary having a $H_{m0} = 10.519$m and $T_p = 11.21$s, which was considered sufficient compared to the values given as input, see **Table 8.1**.

It should be noted that if the effect of quadruplet wave-wave interactions were to be used, the calculation of these interactions are based on a frequency resolution of $\frac{\Delta f}{f} = 0.1$. With the chosen values of f_{low}, f_{high} and n_{freq}, the frequency resolution $\frac{\Delta f}{f} = 0.038$ which is far from the desired value of 0.1. This was not a problem in the long crested test case, as quadruplet wave-wave interactions were turned off.

When all the above mentioned parameters had been decided and specified in the SWAN input file, the wave model was run from a command window. The results have been post processed, and compared with the results from the model test in MATLAB.

Comparing results of the long crested test case from SWAN with the model test results from Svangstu (2011)

The following calculations have been performed by the self-developed Matlab script *svang.m*.

In the model test by Svangstu (2011), 10 tests were performed with the sea state parameters and setup described in **Table 8.1**. Wave probes measured the wave elevation at several locations from a full scale depth of d=67.23m to d=15m. By calculating the variance of the non-transient part of each time series, the significant wave height was calculated from

$$\hat{H}_{m0} = 4\sqrt{Var(\zeta(t))} \tag{8.4}$$

where $\hat{H}_{m0}$ is the *measured* significant wave height and $\zeta(t)$ is the time series of the wave elevation measured by the wave probe at a given location. This was done for all the 10 tests performed in the model test, and plotted against the dimensionless water depth d/λ_p, where λ_p is the wave length corresponding to the peak period of the sea state, where λ_p is given by

$$\lambda_p = \frac{g}{2\pi} T_p \tanh(\frac{2\pi}{\lambda_p} d) \tag{8.5}$$

where T_p is the peak period of the sea state, g is the acceleration of gravity and d is the water depth at the given location. λ_p was computed by iteration in Matlab.

As the wave elevation is known at the "input boundary", i.e. at a full scale depth of d=67.23 m, the wave spectrum was computed using the Welch's method by the built-in function *pwelch* in Matlab. This function splits the data into overlapping segments, computes modified periodograms of the overlapping segments, and averages the resulting periodograms to produce the *power spectral density estimate*. The default settings were used, except the length of the overlapping segments. The longer the overlapping segments, the less detail will be included in the wave spectrum. The default length of the overlapping segments resulted in a wave spectrum with too much detail, and was then by some trial and error set to 2800 points. As the sampling frequency of the wave probes was 100Hz, this is equivalent to a length of 28 seconds of the overlapping segments, and produced a smooth spectrum with enough detail to obtain the trends of the spectrum.

According to Goda (2010), the time series should be corrected for the mean water level by subtracting all the values in the time series by the mean of the time series, to obtain a mean water level of exactly zero. If this is not done, the spectral estimate near $f = 0$Hz may appear large, which is not physical. Goda (2010) also recommends adjusting the energy level of the estimated wave spectrum, by multiplying the spectral estimates by ζ_{rms}^2/m_0, where ζ_{rms}^2 is the root-mean-square of the surface elevation and m_0 is the zeroth moment of the spectral estimate. By doing this we obtain

$$\zeta_{rms} = \sqrt{m_0} \tag{8.6}$$

which by definition should be the case. m_0 is the zeroth spectral moment, where the nth spectral moment according to Myrhaug (2007) is defined as

$$\mathrm{m}_n = \int_0^\infty f^n S(f) df \tag{8.7}$$

By applying the procedure above, the wave spectrum could be estimated at any of the wave probe locations. It was then seen that the shape of the *average* wave spectrum from the 10 tests at a full scale depth of d=67.23m (corresponding to the input boundary in **Figure 8.4**) deviated somewhat from the JONSWAP spectrum given as input to the wave maker, see **Figure 8.6**.

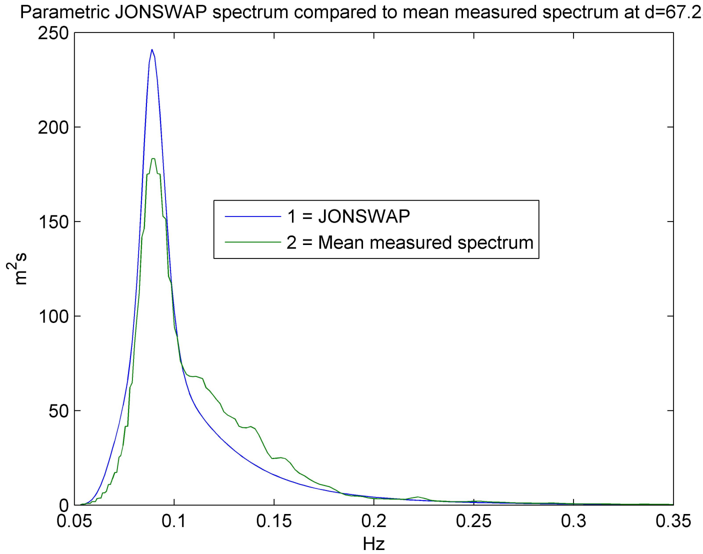

Figure 8.6: Comparison of JONSWAP input spectrum and measured input spectrum

Seen in **Figure 8.6**, the mean spectrum from the 10 runs in the model test has more energy in the frequency range $\sim 0.1 \leqslant f \leqslant\sim 0.18$ Hz and less energy for frequencies less ~ 0.1 Hz compared to the JONSWAP spectrum with the same peak frequency and significant wave height.

As SWAN has the ability to take a *measured* wave spectrum as a boundary condition, the analysis was in addition to the JONSWAP spectrum also run with the measured spectrum as input. The result of how the significant wave height develops as a function of dimensionless water depth, with a JONSWAP-spectrum as input, with a measured input spectrum and the results from the model tests are compared in **Figure 8.7**.

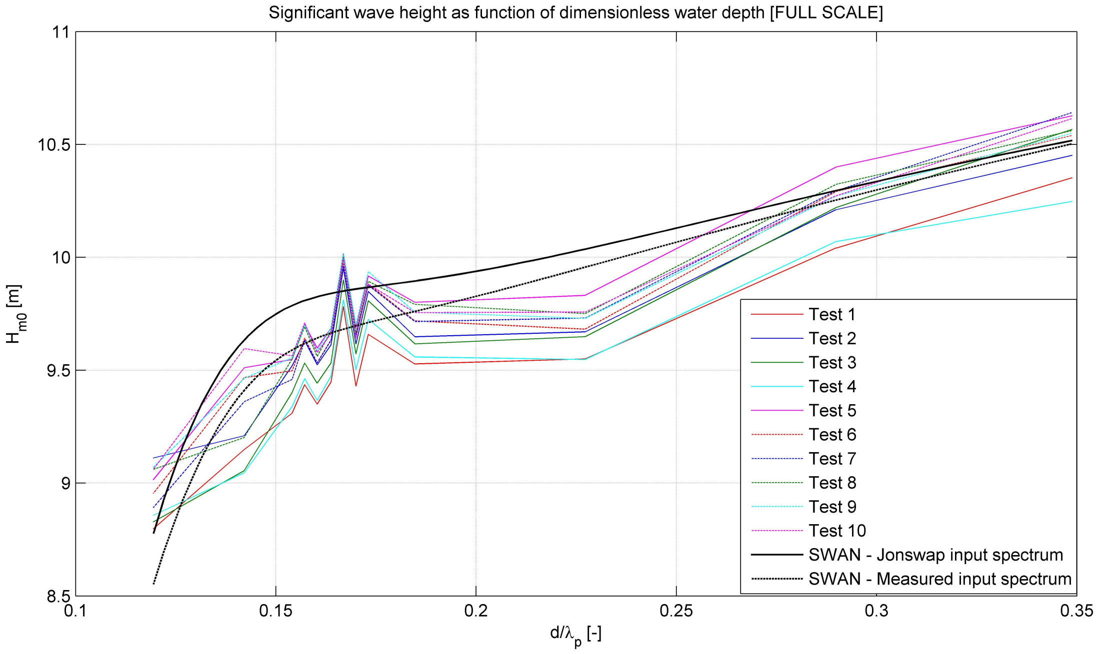

Figure 8.7: Full scale significant wave height as function of dimensionless water depth from 10 model tests compared with results from two simulations in Swan - one with a JONSWAP input spectrum and one with the mean measured input spectrum from the 10 tests

From **Figure 8.7** it is seen that the two Swan simulations resulted in values fairly close to the results from the model tests. It was also seen that the result is dependent on the shape of the incident wave spectrum, as the JONSWAP and measured input spectrum both contains the same energy. The reason for the measured spectrum to result in a smaller significant wave height is not intuitively clear. According to Winterstein (2011), steeper waves were observed when simulating the measured spectrum in **Figure 8.7** compared to when simulating an actual JONSWAP spectrum with the same H_{m0} and T_p. This may lead to believe that the dissipation by white-capping may be larger for the measured wave spectrum, because the dissipation by white-capping increases with increasing steepness, see **Section 5.7**.

How the shape of the wave spectrum was changed as the sea state traveled from the full scale depth of d=67.23m to d=15m, was calculated in Swan both with a JONSWAP input spectrum and the mean measured input spectrum. This result was also compared to the wave spectra obtained from the wave probes. The result is plotted in **Figure 8.8**.

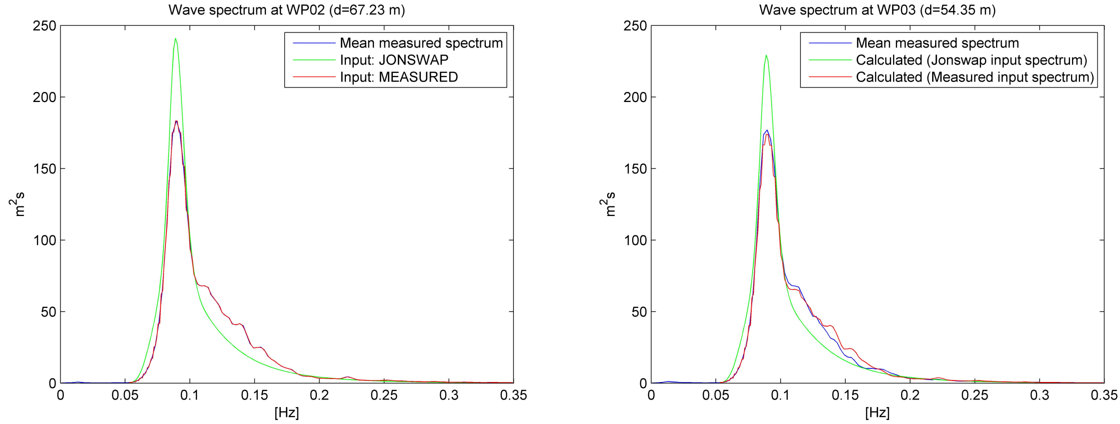

(a) Spectrum at wave probe 2, full scale depth d=67.23m (b) Spectrum at wave probe 3, full scale depth d=54.35m

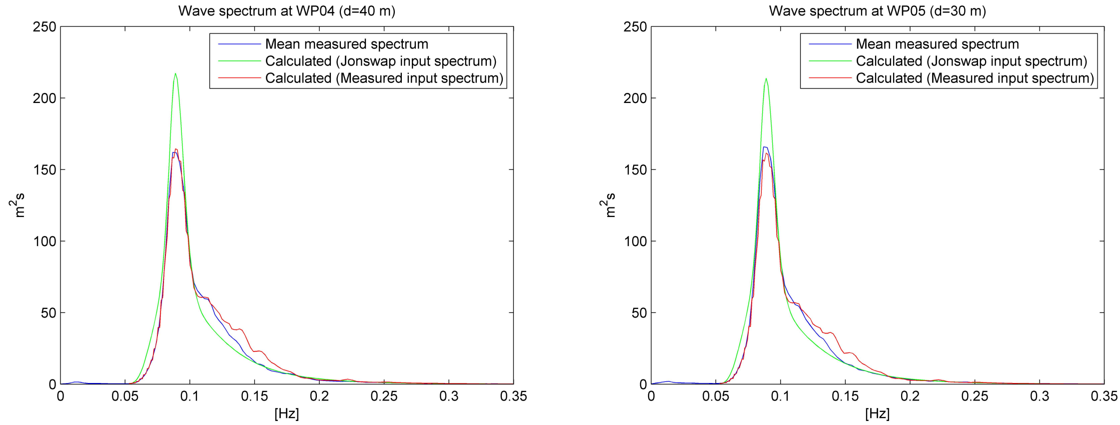

(c) Spectrum at wave probe 4, full scale depth d=40m (d) Spectrum at wave probe 5, full scale depth d=30m

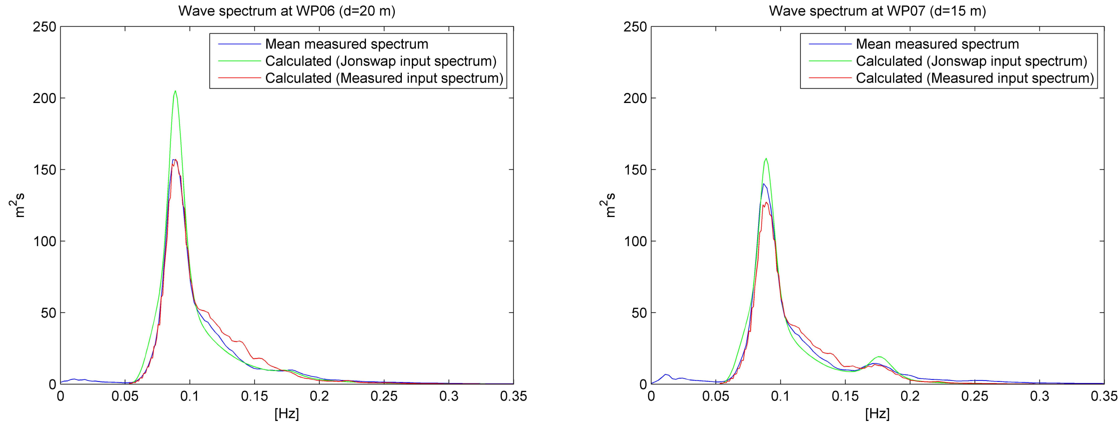

(e) Spectrum at wave probe 6, full scale depth d=20m (f) Spectrum at wave probe 7, full scale depth d=15m

Figure 8.8: Wave spectrum development from a full scale depth of $15m \leqslant d \leqslant 67.23m$. The results from SWAN with a JONSWAP and a mean measured input spectrum is compared to the mean measured spectrum from 10 model tests at the location of the wave probes

From **Figure 8.8 a)** it is seen that the mean measured spectrum given as input to SWAN coincides with the mean measured wave spectrum from the model test, as it should. It is then seen that as the water depth decreases, SWAN calculates a spectrum with *too much* energy in the frequency range $\sim 0.1 \leqslant f \leqslant\sim 0.18$ Hz, for the case with the measured input spectrum. A reason for this may be that the quadruplet wave-wave interactions were turned off in the SWAN analysis, while this effect obviously is present in real life. The quadruplet wave-wave interactions are, as seen in **Figure 5.5**, suppose to redistribute energy from this frequency band, and is therefore believed to be the reason for this difference in the two spectra.

It is also seen that the mean measured spectra for a full scale water depth less that 54.35m contains some energy for frequencies less than 0.053 Hz. This cannot be represented in the SWAN model, as the lowest possible frequency was found to be 0.053 Hz.

In **Figure 8.8 f)**, it is clearly seen a ”bumb” of energy at about 2 time the peak frequency. This is, as seen from **Figure 5.6**, due to the triad wave-wave interactions. The SWAN analysis with the JONSWAP input spectrum overestimates the energy in this region due to the high energy values around the peak frequency, as energy redistributed by the triad wave-wave interactions comes from this frequency range.

Evaluating what effect the different physical processes has on the result

To better understand what effects the different physical processes has on how the significant wave height develops with decreasing water depth, multiple analyzes were run. These analyzes were based on the input file with the *default* settings previously described, but where each analysis was done with one of the physical processes turned off, while the other processes were kept on. In this way, the effect of the physical process could be determined. The default settings had the following physical processes turned *on*:

- Bottom induced wave breaking (surf breaking)
- Bottom friction
- Triad wave-wave interaction
- White-capping
- Refraction

In the different analyzes, one physical process were turned off at a time, keeping all the others turned on. The comparison of how the significant wave height develops as a function of dimensionless water depth is shown in **Figure 8.9**.

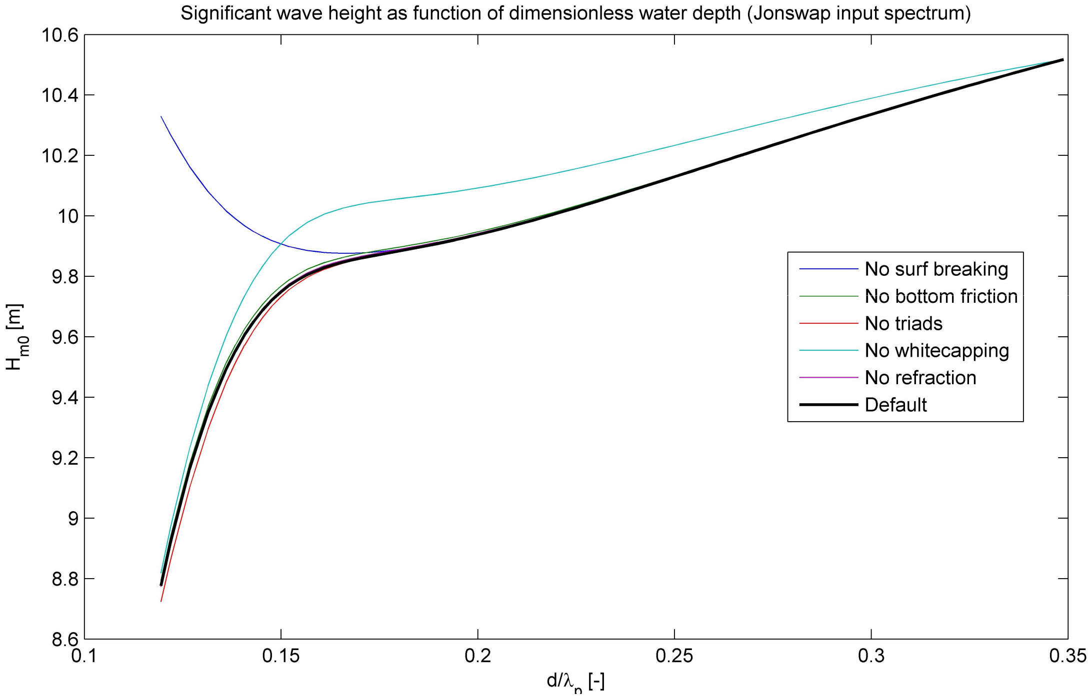

Figure 8.9: Effect of different physical processes on the significant wave height as function of dimensionless water depth

From **Figure 8.9** it is seen that white-capping is the main source of energy dissipation for $d/\lambda_p > 0.15$ ($d >\sim$21.8m), and is the governing physical process in reducing H_{m0} in this region. It is also seen that for $d/\lambda_p < 0.15$ surf breaking is the main source of energy dissipation, and is the governing process in reducing H_{m0} toward the minimum water depth d=15m. It should be noted that the solution does not converge in SWAN, when the physical process of surf breaking is turned off. The effect of the rapid increase of the significant wave height when surf breaking is turned off is the same effect that is present in linear theory, shown in **Figure 2.5**.

Bottom friction has a less pronounced effect compared to the two previously mentioned processes, but it is seen to reduce the significant wave height somewhat in the range $\sim 0.19 > d/\lambda_p >\sim 0.13$.

Triad wave-wave interactions also has a smaller effect on H_{m0} compared to white-capping and surf breaking, but is seen to increase the significant wave height somewhat in the range $d/\lambda_p < 0.15$. The reason for this is not quite clear, but may be due to less energy being dissipated by surf breaking as some energy is redistributed from the peak frequency range to a frequency twice the peak frequency. From **Figure 5.9** it is seen that the main energy dissipation from surf breaking is around the peak frequency, and if there is less energy around the peak frequency (due to redistribution by triad wave-wave interactions) this may cause less energy to be dissipated, i.e. a larger H_{m0}.

It is seen that the effect of refraction is negligible as expected, because the waves are propagating with the wave crest perpendicular towards a shore with bottom contours parallel to the coast line (see **Section 2.2**).

Running SWAN on a short crested test case

The previous described test case was a long crested test case taken from Svangstu (2011). A short crested sea state was also analyzed, to be able to test the effect of quadruplet wave-wave interactions, to see what kind of grid size was necessary when the waves propagates in two dimensions and to compare with the long crested test case. The following parameters were *unchanged* from the long crested test case previously described:

- The boundary conditions (except for the exponent n in the directionality function)
- Output parameters and locations
- Bathymetry and size of computational domain
- The direction resolution (as SWAN recommends a resolution of 10 degrees for wind seas)
- Frequency range

The same sea state was used (i.e. a JONSWAP spectrum with H_s=11.5138, T_p=11.25s and peakedness coefficient of 3.3), but now the exponent n in the directionality function (see **Equation 8.2**) was set to 2, to obtain a typical short crested wind sea according to DNV (2010a). The physical processes were the same as for the long crested case, except for quadruplet wave-wave interactions now were activated (which were turned off in the long crested case).

The frequency resolution $\frac{\Delta f}{f}$ should as previously mentioned be close to 0.1, as the approximation for the quadruplet wave-wave interactions is based on this frequency resolution. The frequency resolution then had to be changed from what was specified in the long crested case as that resulted in $\frac{\Delta f}{f} = 0.038$. To obtain $\frac{\Delta f}{f}$=0.1, the number of frequencies (1+n_{freq}) was simply not given as input, but only the highest and lowest frequency f_{high} and f_{low} (respectively as 0.053 Hz and 1 Hz as before) were given. By only specifying f_{high} and f_{low}, SWAN calculates which n_{freq} is needed to obtain a $\frac{\Delta f}{f}$ of approximately 0.1 by solving **Equation 8.3**. With f_{high}=1 Hz and f_{low}=0.053 Hz this gives n_{freq}=31, i.e. 32 frequencies from f_{low} to f_{high}. The input spectrum was then somewhat coarser than what was used in the long crested case, and resulted in the input spectrum having H_{m0}=10.516 m and T_p=11.179 s.

The last thing to evaluate was which mesh density to be used in the short crested test case. The number of elements in x- and y-direction was decided to be chosen so that the length of each element was approximately the same (i.e. dx≈dy). The effect of grid density on how the significant wave height develops as function of dimensionless water depth (with all physical processes described above turned on) is shown in **Figure 8.10**.

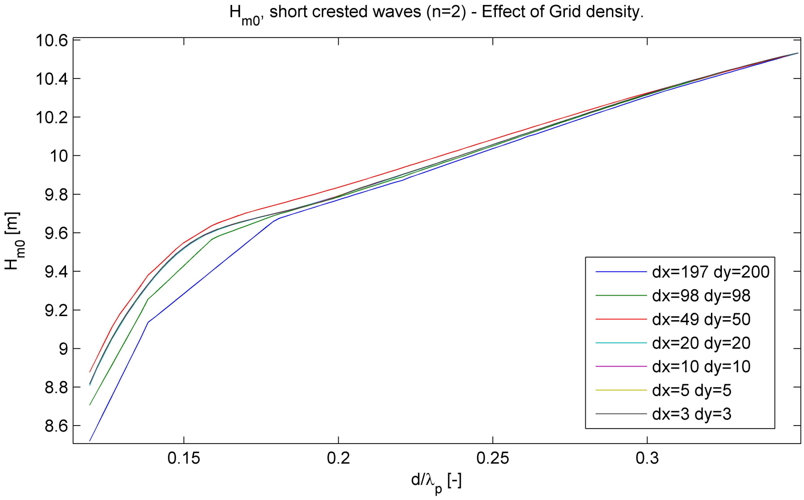

Figure 8.10: Effect of grid density on how the significant wave height develops as a function of dimensionless water depth in the short crested test case

It is seen from **Figure 8.10**, that the solution is as good for a grid density of dx=dy=20 m as for a grid density of dx=dy=3 m, so a grid density of dx=dy=20 m was chosen to save computational time. As all parameters now were chosen, the analysis was run and the result was compared to what was obtained in the long crested case, see **Figure 8.11**.

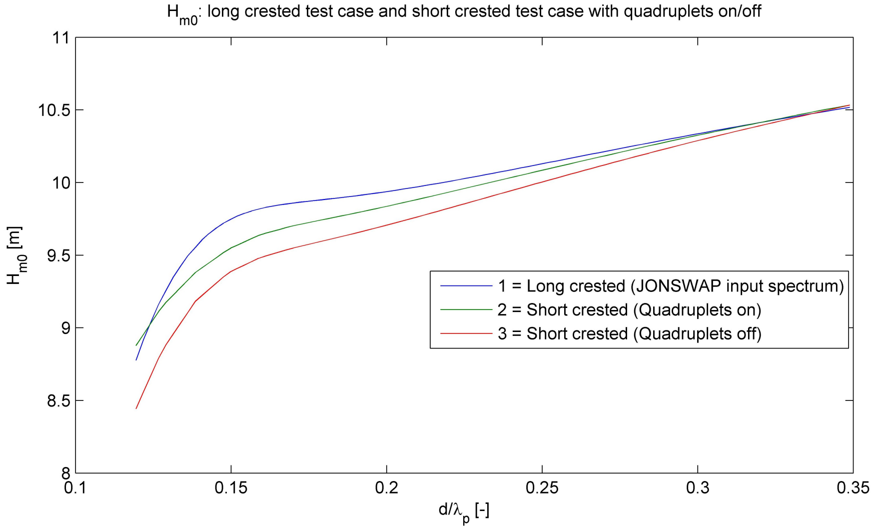

Figure 8.11: Significant wave height as function of dimensionless water depth in short crested (n=2) and long crested (n=65) test case. Th short crested test case was run with and without the effect of quadruplets

From **Figure 8.11** the effect of making the sea state short crested is seen from comparing the blue and red line, where for the short crested case (red line), the quadruplets are turned off to isolate the effect of directional spreading. It is seen that the significant wave height has decreased when the sea state is short crested compared to when it is long crested. This may be because as the energy of the sea state has been spread over a larger direction range, some energy will "escape" out of the lateral boundaries of the computational domain (at y=0 and y=5000). This energy did *not* escape in the long crested sea state, resulting in a larger significant wave height for a long crested sea state. The effect of directional spreading is further investigated in the next subsection.

The effect of turning the quadruplet wave-wave interactions on is seen from comparing the red and green line in **Figure 8.11**. This result is quite surprising as one might expect the opposite effect, namely a reduction of the significant wave height. The reason for expecting a lower significant wave height when quadruplet wave-wave interactions are turned on is that when energy is redistributed as seen in **Figure 5.5**, the energy redistributed to *higher* frequencies will be dissipated by white-capping, Holthuijsen (2007). A significant effort has been made in trying to understand why turning on quadruplet wave-wave interactions leads to increase the significant wave height, but unfortunately without success. Without further examination, the effect of quadruplet wave-wave interactions is believed to give realistic results, and will be used in the Dogger Bank analysis.

The effect of directional spreading and width of computational domain

From **Figure 8.11** it was seen that when plotting the significant wave height as function of dimensionless water depth for a long crested sea state (n=65) and for a short crested sea state (n=2) it resulted in an overall higher value of H_{m0} for the long crested sea state. This is, as mentioned, believed to be due to the wave components "escaping" out of the lateral sides of the computational domain. To more clearly illustrate this, some plots of the significant wave height over the entire computational domain has been constructed. The first plot, **Figure 8.12** shows how the significant wave height varies over the computational domain for the long crested test case.

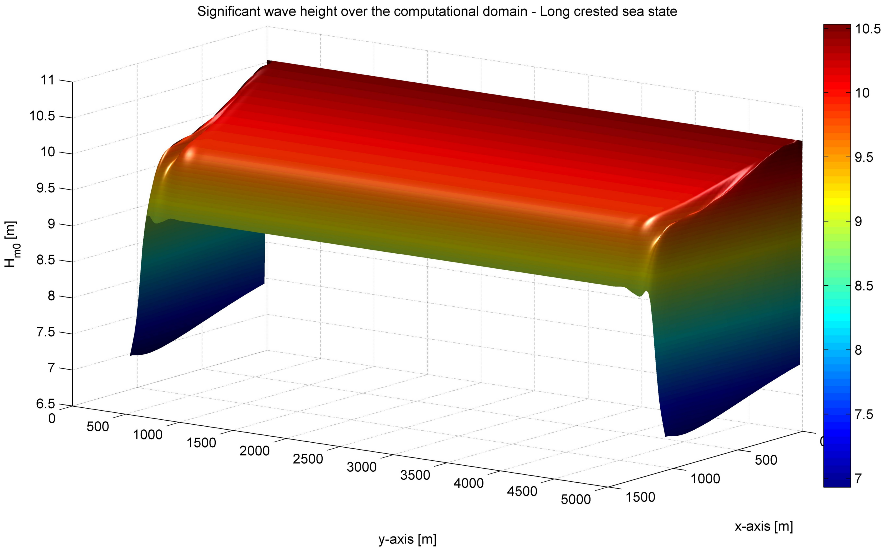

Figure 8.12: The significant wave height over the entire computational domain for the long-crested test case

From **Figure 8.12** it is seen that H_{m0} is approximately constant in y-direction, as expected, due to the longcrestedness of the simulated sea state (and due to the nature of the bathymetry off course). One can also see the disturbance in the solution near the lateral sides of the domain.

In the next plot, the significant wave height is plotted over the computational domain for the short crested test case, see **Figure 8.13**.

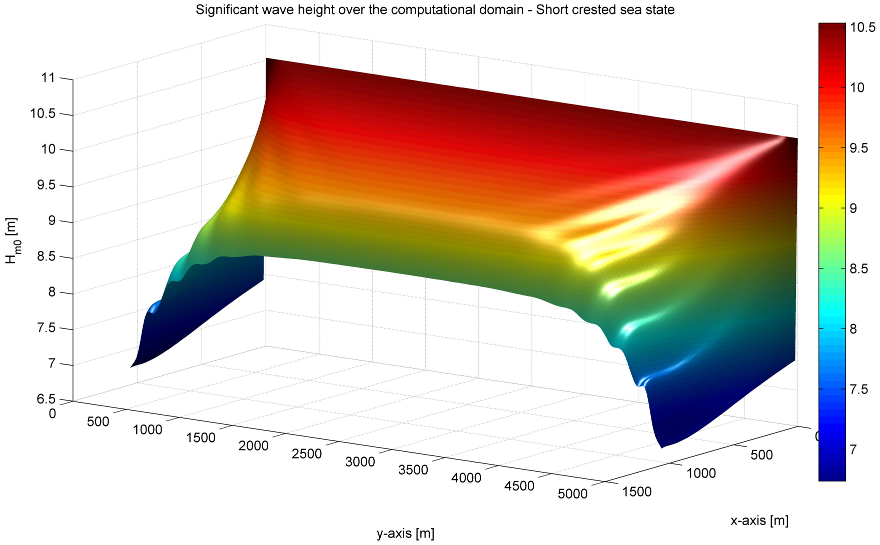

Figure 8.13: The significant wave height over the entire computational domain for the short-crested test case

It is clearly seen from **Figure 8.13** that the significant wave height is no longer independent of y, as H_{m0} decreases as y approaches the boundary values. For values of y close to the middle of the domain (i.e. $y = 2500$), the significant wave height is approximately constant in y-direction which emphasizes the importance of placing the lateral water-water boundaries far away from where reliable results are needed. The wider the computational domain, the wider is the area of $\frac{\delta H_{m0}}{\delta y} = 0$ near the centerline of the domain.

By plotting the two previous surface plots in the same plot, is clearly seen that the significant wave height is larger over the entire domain (except for at the input boundary where it is equal) for the long crested case compared to the short crested case, see **Figure 8.14**. This is seen from the fact that the long-crested, transparent surface plot lies above the short-crested surface plot.

To see how the effect is enhanced with increasing longcrestedness, the result from varying the spreading coefficient n from 2 (short crested) to 65 (long crested) is shown in **Figure 8.15**, taken at the center line of the computational domain. In **Figure 8.15** the quadruplets have been turned off, to avoid the bad handling of long crested waves to distort the result.

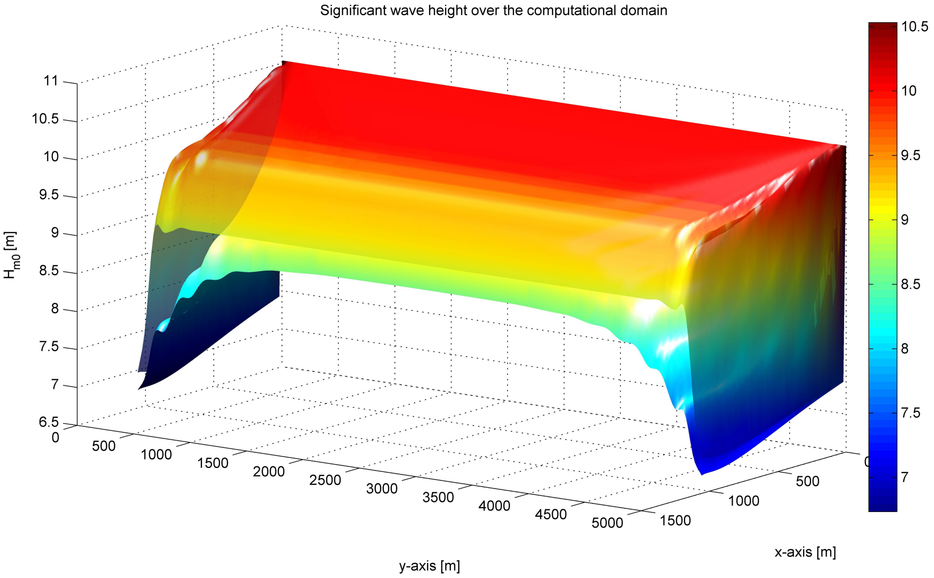

Figure 8.14: The significant wave height over the entire computational domain for both the long-crested test case (upper, transparent surface) and the short-crested test case (lower, nontransparent surface)

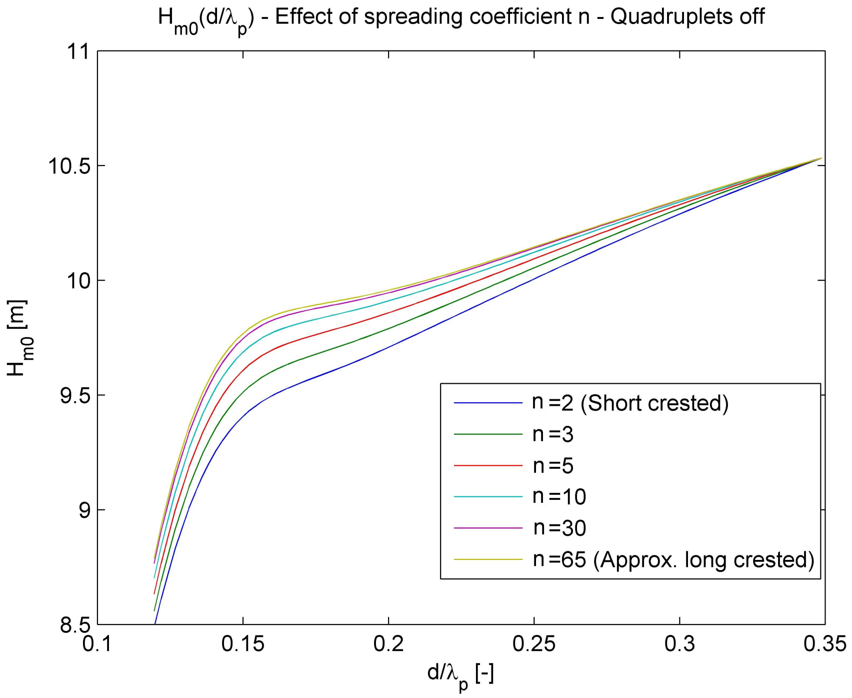

Figure 8.15: The effect of directional spreading on the significant wave height when quadruplets are turned off. The increase in significant wave height is clearly seen as the sea state is more and more long crested

From **Figure 8.13** it is clearly seen that if output is taken close enough to the lateral sides (y=5000 or y=0), the result will be influenced by these boundaries. As long as the output is taken in the center line (y=2500) it is not a problem, but to illustrate how the area of $\frac{\delta H_{m0}}{\delta y} = 0$ near the center of the domain increases with increasing computational width, three runs was done in SWAN: one with 5000m, one with 7500m and one with 20000m width. The significant wave height was then plotted along a straight line parallel with the y-axis where the water depth were constantly equal to 15m see **Figure 8.16**.

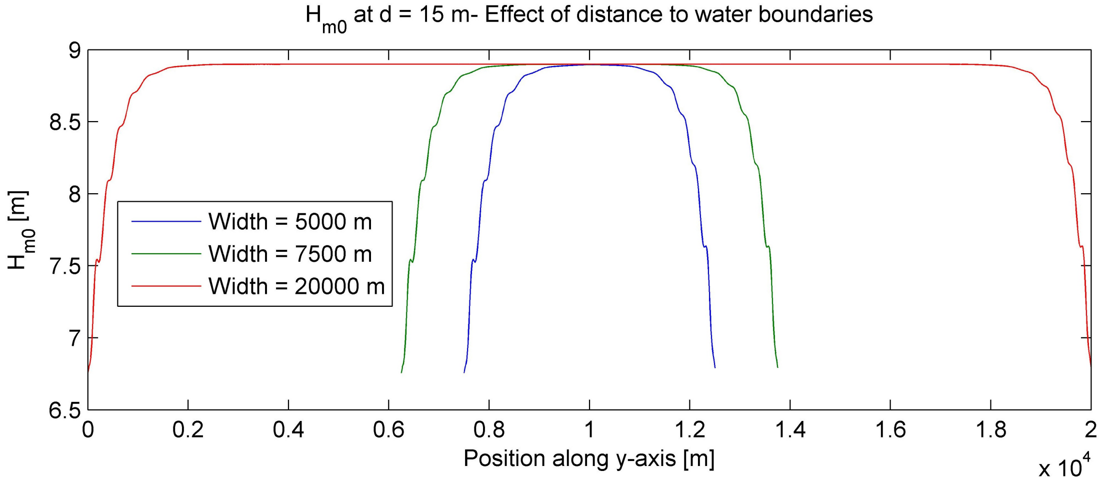

Figure 8.16: The effect of the width of the computational domain for the short crested test case

For this idealized case, **Figure 8.16** shows that as long as the output is taken in the center line of the domain, the result will be the same for the three runs. If, however, the output is *not* taken in the center of the domain, it is seen that one should choose a width of the computational domain large enough, such that the lateral boundaries does not influence the solution.

The effect of wind on the short crested test case

As there will be a wind present in a realistic case, the effect of the wind speed has also been investigated. The sea state is the same as described above (i.e. default settings with quadruplets turned on), and the wind is modeled as a constant wind in the same direction as the main wave direction. The effect of the wind on how the significant wave height develops with decreasing dimensionless water depth is shown in **Figure 8.17**.

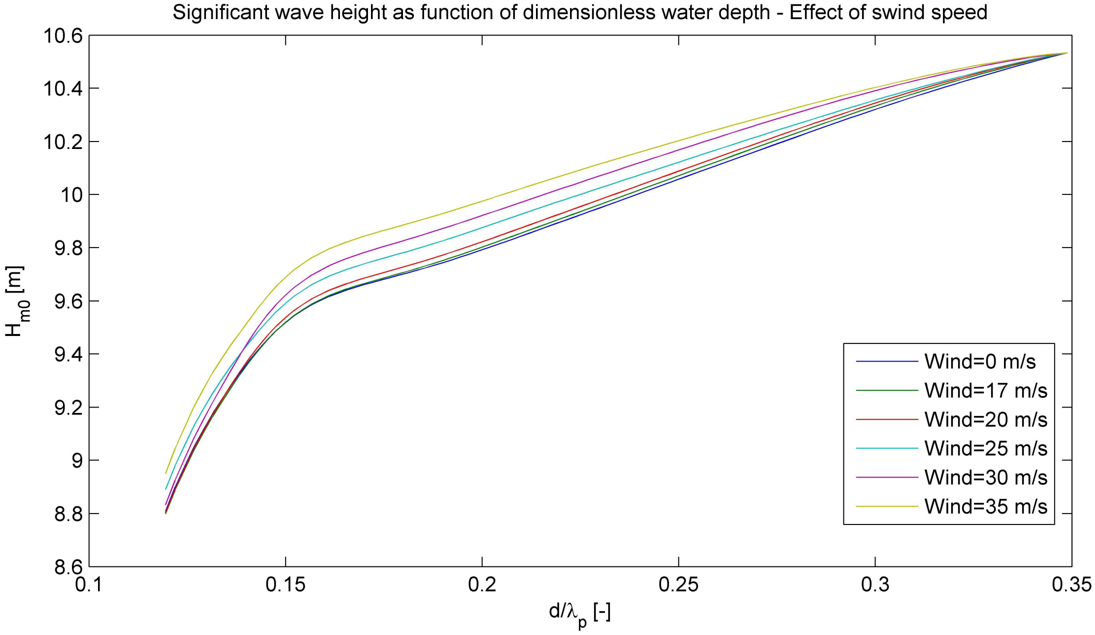

Figure 8.17: The effect of the wind speed on how the significant wave height develops as function of dimensionless water depth

As expected, the significant wave height is increased when the wind speed is increased, as more energy is transferred to the wave spectrum, see **Figure 8.17**. It is also seen that the effect is somewhat larger for $d/\lambda_p > 0.15$ ($d >\sim$21.8m), than for $d/\lambda_p < 0.15$, when surf breaking is the dominating (dissipating) process.

8.2.2 Obtaining the sea state parameters at the location of interest in the Dogger Bank Zone from SWAN

After getting familiar with using SWAN and getting some experience of which parameters were important, the Dogger Bank case was analyzed. The input boundary condition was a JONSWAP spectrum with peakedness coefficient 3.3, $H_{m0} = 11.74$m and $T_p = 15.68$s, as found from the long term analysis in **Section 7.2** at a point north of the Dogger Bank Zone. This input boundary condition was applied along the northern boundary of the computational domain.

The spreading coefficient in **Equation 8.2** was for this case also chosen to be n=2, even though the result from **Figure 8.15** may indicate that this is nonconservative. The reason why choosing n=2 will be shown later.

The bathymetry data available, as seen in **Figure 7.1**, was cropped to include the northern point (where NORA10 data was used to estimate the 50-year sea state) on the northern boundary, and some of the southern part excluded to limit computational time (as the area south of the point of interest is not needed). The bathymetry with the northern data point, the Dogger Bank Zone and the southern point (the point where output is of interest) is shown in **Figure 8.18**. The length (in y-direction) is 134km and the width (in x-direction) is 186km and the length between each point of bathymetry data is 500m. The same size has been used for the computational domain in SWAN.

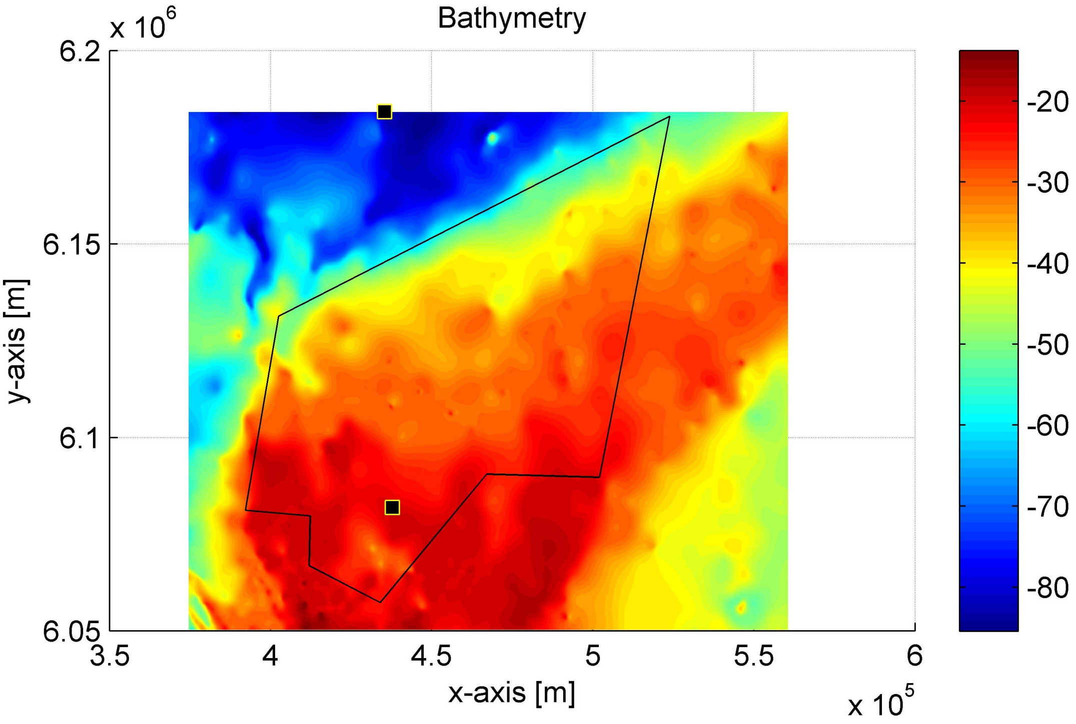

Figure 8.18: The bathymetry used as input in SWAN for the Dogger Bank case

The directional resolution was set to 10 degrees, as recommended by SWAN (2006) for wind seas.

The following physical processes were active during the analysis: bottom friction, surf breaking, refraction, white-capping, triad wave-wave interactions and quadruplet wave-wave interactions. In addition a constant wind was applied. To determine what wind speed to use together with the 50-year sea state, the three largest storms of the hindcast data coming from north during the 53.4 year long hindcast data was evaluated. As recommended by Sverre Haver, the wind speed was set to the average wind speed from 6 hours *before* until three hours *after* the peak significant wave height during each of the three largest storms. This average value was calculated to be $23.3\frac{m}{s}$. The wind speeds used to calculate this mean value is shown in **Figure 8.19**.

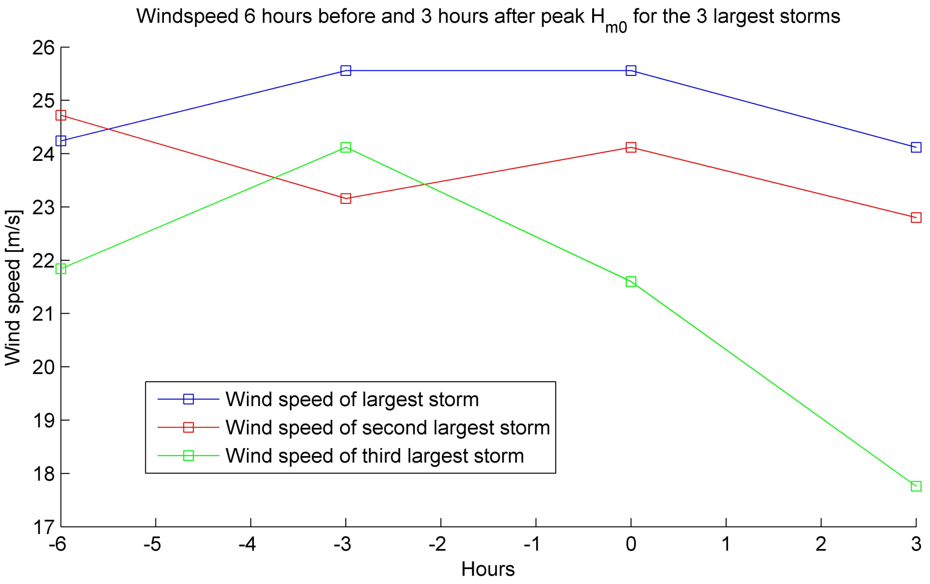

Figure 8.19: The wind speed 6 hours before and 3 hours after peak significant wave height for the three largest storms in the 53.4 year long hindcast data. Time = 0 indicates location of peak significant wave height during the storm.

As the peak frequency of this sea state (T_p=15.68s) is higher than what was used in the test case (T_p=11.25s), the peak frequency will be smaller in this case, compared to the test case. This means that lower frequency f_{low} must be set lower than what was used in the test case, to be able to represent the input spectrum properly. The smallest value accepted by SWAN was f_{low} = 0.025Hz and f_{high} was still set to 1 Hz. The frequency resolution was not specified, so SWAN automatically set the number of frequencies (1+n_{freq})=40 to best satisfy the quadruplet interaction requirement ($\frac{\Delta f}{f} = 0.1$). This resulted in H_{m0}=11.76m and T_p=15.48s which was taken as adequate for this purpose, compared to what was specified in the input file.

From the short crested sea state in the previous section, an optimal spatial grid size of the computational domain was found to be dx=dy=20m. As the computational domain now is *much* larger, such a fine resolution would demand unnecessary large amount of computer memory during the computations. To find out what grid size to use, the grid size was varied from dx=dy=100 m to dx=dy=1000m. The result of how the mesh density affects how the significant wave height varies from the northern to the southern point is shown in **Figure 8.20**.

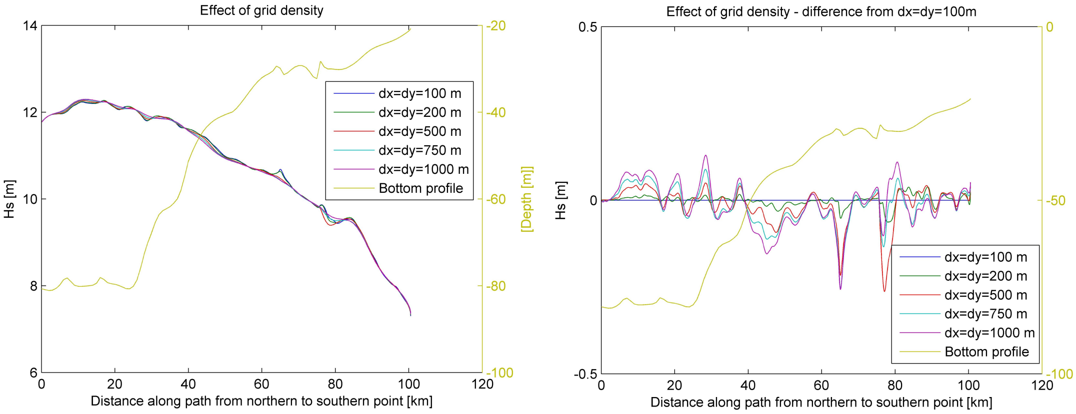

Figure 8.20: (Left:)The effect of mesh density on the significant wave height for the Dogger Bank case along the path from the northern to the southern point in **Figure 8.18**. The water depth is also plotted. (Right:) The difference in significant wave height compared to the finest grid (dx=dy=100m) along the same path.

As seen from **Figure 8.20**, the result deviates very little when comparing dx=dy=100m to dx=dy=1000m. The grid size was then chosen to be dx=dy=500m, as this gave a reasonable computational time.

The spreading of the sea state was chosen by specifying the spreading coefficient to be n=2, as previously mentioned. From **Figure 8.15** it was seen that the significant wave height increased with increasing value of the spreading coefficient, and DNV (2010a) recommends $2 \leqslant n \leqslant 4$ for wind seas. From this it may seem like choosing n=2 is somewhat nonconservative. The Dogger Bank case was run in SWAN with the settings described above, but with a varying n from 2 to 4. The result is shown in **Figure 8.21**.

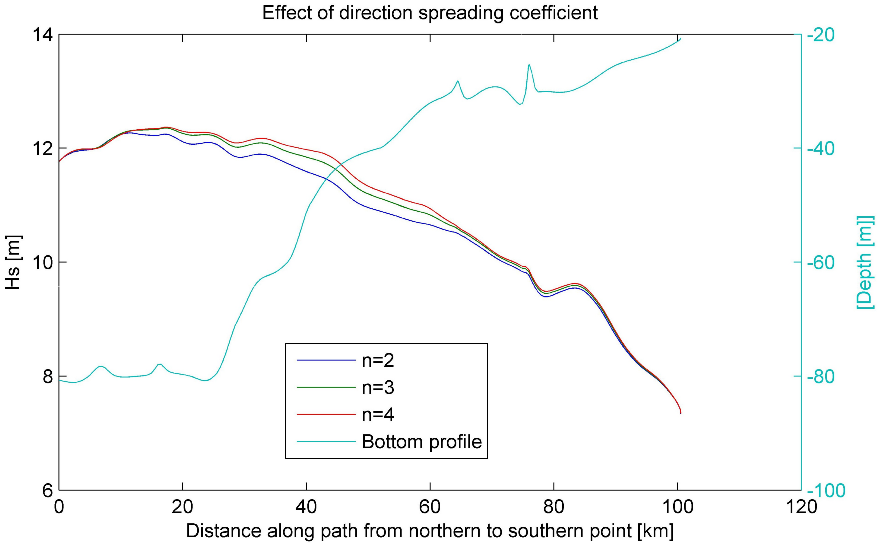

Figure 8.21: The effect of spreading coefficient on H_s for the Dogger Bank case

It is seen from **Figure 8.21** that for the shallower part of the path from north to south, the effect of n is negligible, so setting n=2 is taken as sufficient.

As indicated in **Figure 8.16**, one should check if the width of the computational domain is large enough so that the lateral water-water boundaries influence the result. From **Figure 8.18** it is seen that the output will *not* be taken along the centerline of the domain, so to investigate whether or not the proximity of the lateral boundaries influence the result, a modified bathymetry was constructed. This modified bathymetry was the same as the original, except for that it was made *twice as wide*. This was done by specifying a computational domain twice as wide as the bathymetry in SWAN. By doing this, SWAN assumes that the bottom level *outside* the specified bathymetry is constantly equal to the last specified point, see **Figure 8.22**.

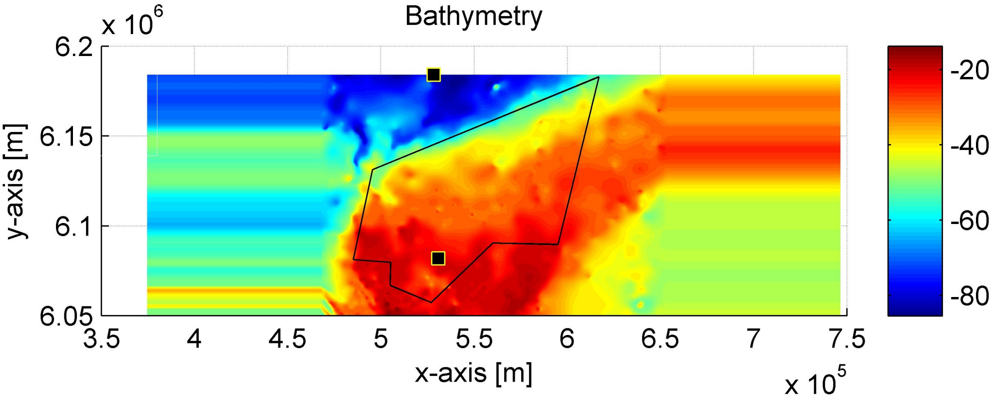

Figure 8.22: The modified bathymetry - twice as wide as the original

The analysis was then run and the result was compared to that obtained with the original width, see **Figure 8.23**. It is seen that towards the shallower part of the computational domain (where output is of interest), the result is not much influenced by the proximity of the lateral boundaries, and the original width was assumed as adequate.

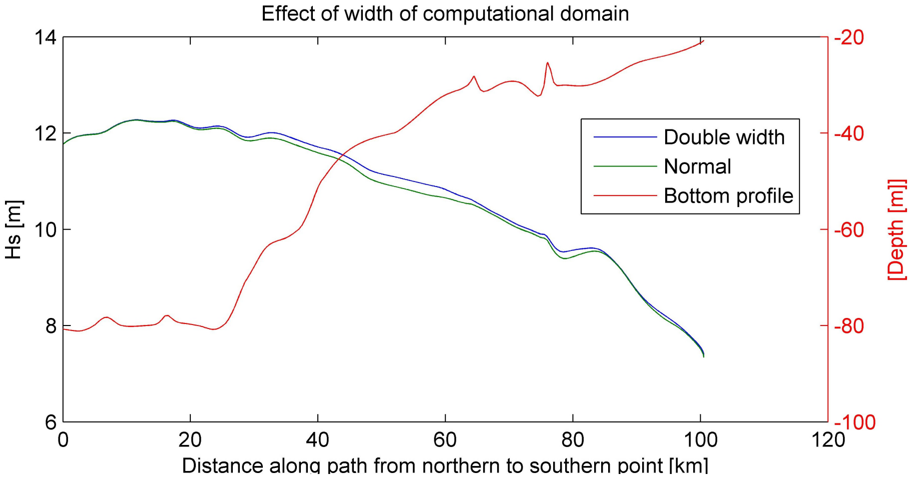

Figure 8.23: Effect of the width of the computational domain on H_s in the Dogger Bank case

The final result of how the significant wave height develops along the path from the northern to the southern point can be seen in **Figure 8.23** with *normal* width of the computational domain, i.e. the green line. The result was also computed in all points of the computational domain, and the contour plot can be seen in **Figure 8.24**.

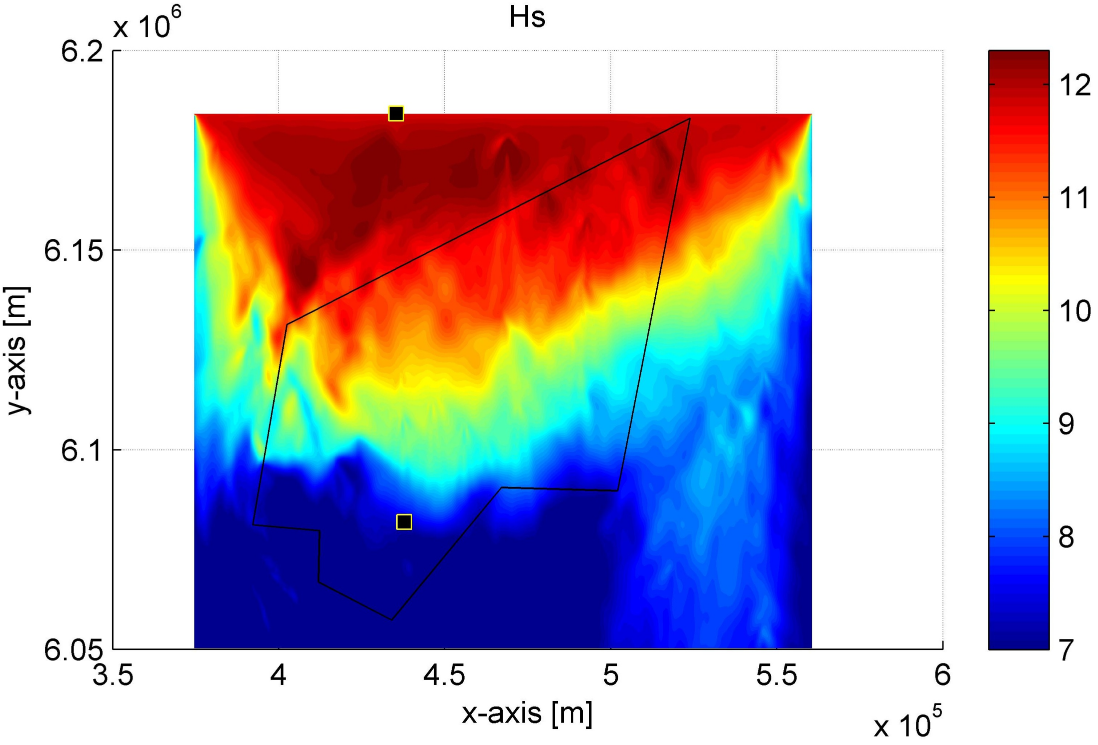

Figure 8.24: The significant wave height over the entire computational domain in the Dogger Bank case

The resulting 50-year sea state obtained at the southern point was found to have significant wave height of $H_{m0,50} = 7.34\text{m}$ and peak period of $T_{p,50} = 15.56\text{s}$.

The input wave spectrum used at the northern boundary (and thus in the northern point) and the resulting wave spectrum in the southern point can be seen in **Figure 8.25**. It is clearly seen that much energy has been dissipated and that energy has been redistributed to higher frequencies, both effects as expected, by comparing the two spectra.

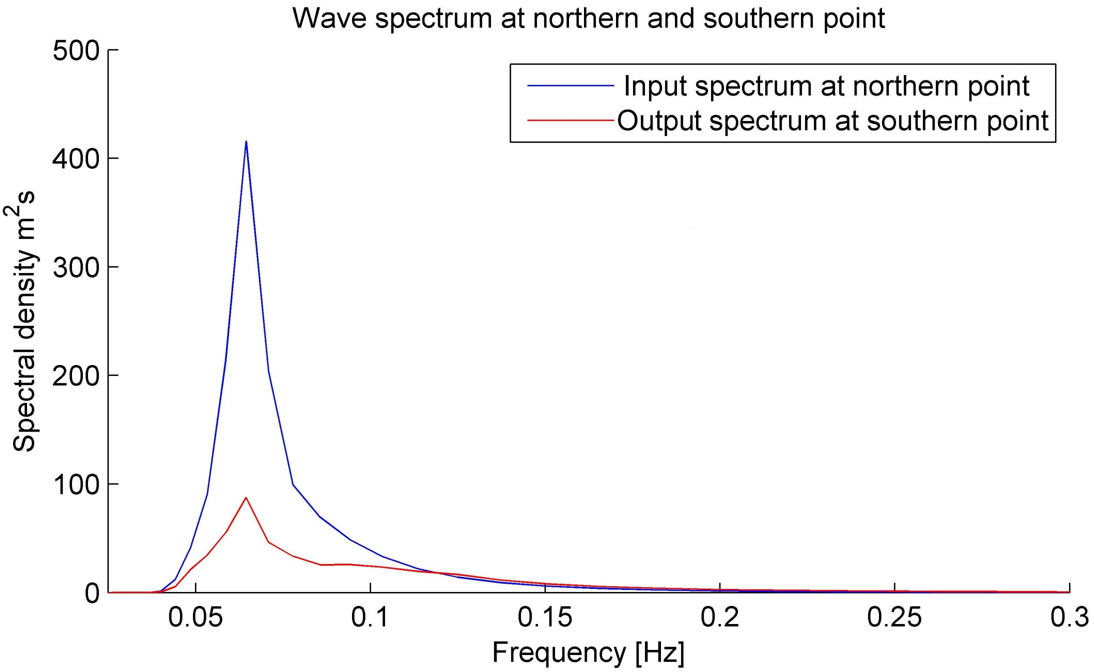

Figure 8.25: Wave spectrum at northern and southern point in the Dogger Bank case

9. Results from SWAN Versus Results from NORA10

As the resulting 50-year sea state was estimated at the southern point, it would be of interest to see how results from SWAN relates to the results from NORA10. To evaluate this, the three largest storms with waves propagating from north (i.e. from 330-15 degrees, as specified in **Figure 7.3**) at the northern point according to NORA10 was simulated in SWAN. The output from SWAN in the southern point was then compared to the corresponding values from NORA10.

The three largest storms in the northern point according to NORA10 are presented in **Table 9.1**.

Table 9.1: Three largest storms at northern point from NORA10

Sea state	H_s [m]	T_p [s]	Mean wave dir [deg]	Wind speed [m/s]	Wind dir [deg]
1	12.00	16.80	346.00	25.56	342.00
2	10.10	15.32	346.00	24.12	345.00
3	10.10	14.64	355.00	21.60	341.00

These three sea states were then simulated in SWAN with the exact same settings as described for the 50-year sea state. As the peak period of these sea states were close to what was used for the 50-year sea state, the input wave spectra were well represented by the same frequency range and resolution. The resulting development of the significant wave height from the northern to the southern point of these three sea states are shown in **Figure 9.1**.

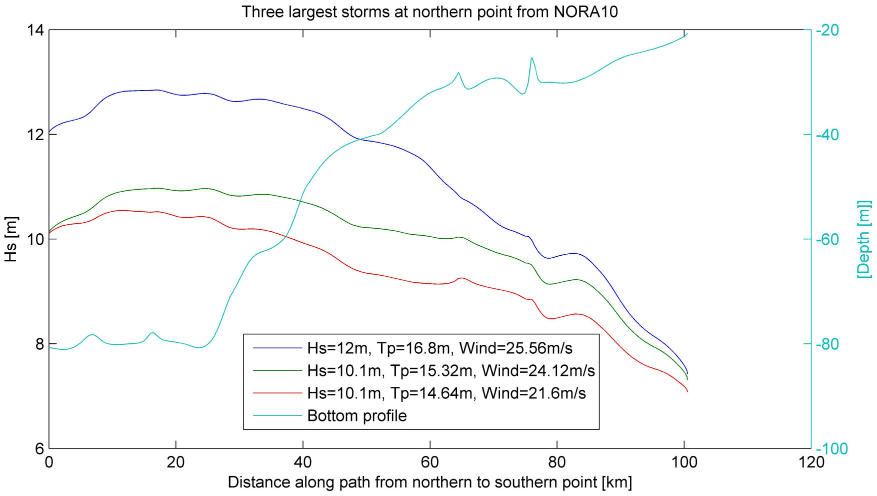

Figure 9.1: The development of the significant wave height of the three largest storms found in the hindcast data at the northern point, analyzed in SWAN

The results from SWAN at the southern point for the three simulated sea states are presented in **Table 9.2**.

Table 9.2: Result from SWAN at southern point when the three largest storm from NORA10 was used as input in northern point

Sea state	Hs [m]	Tp [s]	Mean wave dir [deg]	Wind speed [m/s]	Wind dir [deg]
1	7.42	16.89	355.52	25.56	342.00
2	7.31	15.38	355.74	24.12	345.00
3	7.08	14.64	354.97	21.60	341.00

The corresponding results from the NORA10 data at the southern point are shown in **Table 9.3**.

Table 9.3: Corresponding result from NORA10 at southern point for the three largest storms originating from the northern point

Sea state	Hs [m]	Tp [s]	Mean wave dir [deg]	Wind speed [m/s]	Wind dir [deg]
1	10.20	15.98	352.00	24.00	346.00
2	8.60	15.03	345.00	23.52	339.00
3	8.30	14.45	352.00	21.12	336.00

The percentage deviations from SWAN compared to NORA10 at the southern point are presented in **Table 9.4**.

Table 9.4: Percentage deviations from SWAN compared to NORA10 at the southern point for the three largest storms originating from the northern point

Sea state	Hs [%]	Tp [%]	Mean wave dir [%]	Wind speed [%]	Wind dir [%]
1	-27.25	5.69	1.00	6.50	-1.16
2	-15.00	2.33	3.11	2.55	1.77
3	-14.70	1.31	0.84	2.27	1.49

From **Table 9.4** the suspicion of NORA10 over-predicting the significant wave height in the relatively shallow part of the Dogger Bank Zone compared to SWAN is confirmed. It is seen that for the three largest storms originating from the northern point, the significant wave height at the southern point is about 15-27% smaller when using SWAN compared to NORA10, when the same input is used at the northern point. It is also seen that assuming a constant wind over the entire domain in SWAN is somewhat conservative, as the wind speed is over all smaller at the southern point compared to at the northern point from NORA10. From **Table 9.4** it is indicated that the significant wave height of the 50-year sea state at the southern point found in **Section 8.2.2** is some 15-27% smaller than what would be obtained using the NORA10 hindcast model.

10. Determining the design wave parameters

10.1 The 50-year wave height

The characteristics of the 50-year sea state has been obtained at the area of interest, and the wave height corresponding to a 50-year return period will be estimated from this sea state. To do this, a short term analysis will be performed on the 50-year sea state found in SWAN.

Haver and Winterstein (2009) found that if they compared a consistent long term analysis for the 10^{-2} probability wave crest height at a North Sea site $\hat{c}_{0.01}$, the *most probable* largest crest height, within the 100-year sea state underestimated $\hat{c}_{0.01}$ by about 10%. This was using the *Rayleigh distribution* of wave crests, and the most probable largest wave crest corresponded to

$$F_{c_{\max}|H_{m0}T_p}(c_{\max}|\,H_{m0}T_p) = 0.37 \tag{10.1}$$

They found, however, that the crest height obtained by using a *higher* percentile, i.e.

$$F_{c_{\max}|H_{m0}T_p}(c_{\max}|\,H_{m0}T_p) = 0.85 \tag{10.2}$$

matched very well with the 10^{-2} probability wave crest height found from the consistent long term analysis. This is illustrated in **Figure 10.1**.

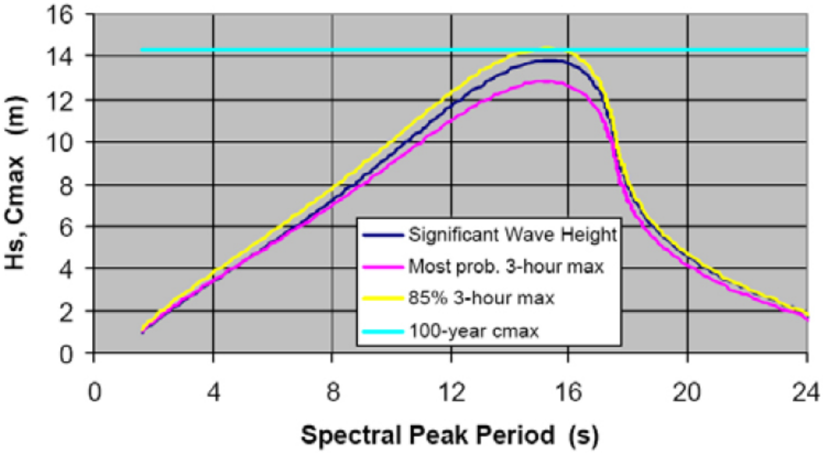

Figure 10.1: The environmental contours, most probable crest height, 0.85-percentile crest height and the 100-year maximum crest height obtained by a long term analysis, Haver and Winterstein (2009)

This result is transferable to estimating the 50-year *wave height* from the 50-year sea state according to Sverre Haver. The distribution of largest wave heights within a sea state is given in Myrhaug (2007) as

$$F_{H_{\max}|H_{m0}T_p}(H_{\max}|\,H_{m0}T_p) = \left[F_{H|H_{m0}T_p}\right]^N \tag{10.3}$$

where $F_{H|H_{m0}T_p}$ is the conditional cumulative probability function of individual wave heights, and N is the number of zero crossings during the duration D of the sea state

$$N = \frac{D[\text{sec}]}{T_z[\text{sec}]} \tag{10.4}$$

D will be the time between each H_{m0} in the hindcast data (3 hours, i.e. 10800 seconds from NORA10 data), and the zero crossing period T_z could be found from the relationship between T_p and T_z depending on which spectrum is assumed. If the JONSWAP spectrum was chosen as wave spectrum of the sea state, the relationship between T_p and T_z is given by DNV (2010a) as

$$\frac{T_z}{T_p} = 0.6673 + 0.05037\gamma - 0.00623\gamma^2 + 0.0003341\gamma^3 \tag{10.5}$$

where γ is the non-dimensional peak shape parameter used as input in the spectrum.

By evaluating **Figure 8.25**, it is seen that the wave spectrum at the southern point no longer has the shape of a typical JONSWAP spectrum, even though the JONSWAP spectrum was used as input at the northern boundary. This is due to the processes described in **Chapter 5**. SWAN, however, has the option of giving T_{m02}, the spectral estimate of the zero crossing period, as output at any point. The spectral estimate of the zero crossing period is given by Myrhaug (2007) as

$$T_{m02} = \sqrt{\frac{m_0}{m_2}} \tag{10.6}$$

where m_0 and m_2 are the zeroth and second moment of the wave spectrum. As the relationship between T_z and T_p is unknown for the wave spectrum at hand, T_{m02} will be used instead of T_z in **Equation 10.4**.

The fractile used (e.g. 0.85) will be larger if the response (here the wave height) is highly nonlinear, where DNV (2010a) recommends a fractile up to 0.9. This means that if the water depth at the site of interest is relatively small compared to the wave height, the surface process is expected to be nonlinear, and it at least won't be nonconservative to assume a fractile of 0.9. No further details on this will be considered.

Next, which short term wave height distribution to use in solving

$$\left[F_{H|H_{m0}T_p}\right]^N = 0.9 \tag{10.7}$$

had to be decided.

10.1.1 What wave height distribution to assume at the site of interest

In the following, various cumulative distributions for the individual wave height will be presented.

Rayleigh distribution

The Rayleigh distribution assumes the instantaneous surface elevation to be a Gaussian, stationary and narrow banded process (energy confined in a narrow range of frequencies), and is assumed conservative in deep water, Myrhaug (2007). The cumulative distribution function is given by

$$F_H\left(H\right) = 1 - \exp\left(-2\left(\frac{H}{H_{m0}}\right)^2\right) \tag{10.8}$$

Rayleigh distribution proposed by Næss

Næss (1985) proposed to correct for the conservative assumption of the wave elevation to be a narrow banded process by bandwidth correcting the Rayleigh distribution. This cumulative distribution function is given by

$$F_H\left(H\right) = 1 - \exp\left(-\left(\frac{H}{\alpha_H H_{m0}}\right)^2\right) \tag{10.9}$$

where α_H is the bandwidth correction factor given by

$$\alpha_H = \frac{1}{2}\sqrt{1-\rho} \tag{10.10}$$

where ρ reflects the bandwidth effects with typical values in the range -0.75 to -0.6. A possible parameterization of ρ as function of the JONSWAP peak parameter γ is given in DNV (2010a) for $(1 \leqslant \gamma \leqslant 10)$

$$\rho = -0.000191\gamma^3 + 0.00488\gamma^2 - 0.0525\gamma - 0.605 \tag{10.11}$$

Forristall distribution

According to DNV (2010a) the empirically based short term wave height distribution is given by the Weibull distribution as

$$F_H\left(H\right) = 1 - \exp\left(-\left(\frac{H}{\alpha_H H_{m0}}\right)^{\beta_H}\right) \tag{10.12}$$

where Forristall in 1978 showed that the shape parameters $\alpha_H = 0.681$ and $\beta_H = 2.126$ based on buoy data from the Mexican Gulf. These values have been found to have a more general applicability than just in the Mexican Gulf.

Forristall also derived a probability distribution for the wave crest height, when the sea surface elevation is modeled by second order theory. Details on this are not given here, but the keen reader is referred to DNV (2010a).

Gluhovski distribution

According to Hameed and Baba (1985) the Gluhovski distribution is given by

$$F_H(H) = 1 - \exp\left(-\frac{\pi}{4\left(1+\frac{\bar{H}/d}{\sqrt{2\pi}}\right)}\left(\frac{H}{\bar{H}}\right)^{\frac{2}{1-\bar{H}/d}}\right) \tag{10.13}$$

where the average wave height $\bar{H}$ according to Goda (2010) is given by

$$\bar{H} = \sqrt{2\pi m_0} = \sqrt{\frac{\pi}{8}}H_{m0} \tag{10.14}$$

This distribution takes the water depth, d, into account, and is according to Hameed and Baba (1985) explaining the distribution of wave heights from deep water to the surf zone. For deep water (i.e. $\left(\bar{H}/d\right) \to 0$) **Equation 10.14** takes the form of the Rayleigh distribution as shown in **Equation 10.8**.

Battjes and Groenendijk distribution

According to DNV (2011) the Battjes and Groenendijk distribution can be used in shallow waters with a constant seabed slope. The distribution is a composite Weibull distribution given by

$$F_H(H) = \begin{cases} 1 - \exp\left(-\left(\frac{h}{h_1}\right)^2\right) & \text{for h} \leqslant \text{h}_T \\ 1 - \exp\left(-\left(\frac{h}{h_2}\right)^{3.6}\right) & \text{for h} > \text{h}_T \end{cases} \tag{10.15}$$

where the *transition height* h_T is given by

$$\text{h}_T = \left(0.35 + 5.8\tan\alpha\right)d \tag{10.16}$$

where α is the slope angle of the sea bed and d is the water depth.

The parameters h_1 and h_2 are valid for $0.05H_{rms} < h_T < 3H_{rms}$ and is given by

$$\frac{h_2}{H_{rms}} = \frac{1}{0.0835\left(\frac{h_T}{H_{rms}}\right)^3 - 0.583\left(\frac{h_T}{H_{rms}}\right)^2 + 1.3339\left(\frac{h_T}{H_{rms}}\right)} \tag{10.17}$$

and

$$\frac{h_2}{H_{rms}} = 1.06 - 0.01532\left(\frac{h_T}{H_{rms}}\right)^2 + 0.083259\left(\frac{h_T}{H_{rms}}\right)^3 - 0.01925\left(\frac{h_T}{H_{rms}}\right)^4 \tag{10.18}$$

where $H_{rms} = 0.6725H_{m0} + 0.2025\frac{H_{m0}^2}{d}$.

Of the five previously mentioned wave height distributions, only the Gluhovski distribution and Battjes and Groenendijk distribution takes the water depth into account and is believed to give reasonable results in intermediate and shallow water. Rayleigh, Næss and Forristall are mainly used in deep water. Solving **Equation 10.7**, using the 50-year significant wave height $H_{m0,50} = 7.34$m and $T_{m02,50} = 8.21s$ from SWAN at the site of interest, where the water depth is $d = 20.69$m, the 50-year wave height using the five mentioned distributions are presented in **Table 10.1**.

Table 10.1: 50-year wave height at the site of interest from different wave height distributions

Rayleigh	Næss	Forristall	Battjes and Groenendijk	Gluhovski
15.9 [m]	14.8[m]	14.4 [m]	11.9 [m]	12.5 [m]

From **Table 10.1** it is seen that deep water wave height distributions over-predict the wave height compared to what is obtained with the Gluhovski distribution and the Battjes and Groenendijk distribution. It will later be shown that, with the wave period band to be assumed, the wave heights obtained from the deep water wave height distributions are larger than the *theoretical largest* wave at that water depth. From this it is seen to be most conservative to choose the result from the Gluhovski distribution, so that the 50-year wave height has been estimated to be $H_{50} = 12.5$m at the site of interest.

10.2 Determining the corresponding wave period

The following calculations have been performed by the self-developed MATLAB script *period_largest_svang.m*.

According to Sverre Haver, Statoil uses the relationship $T_{\frac{1}{3}} = 0.9T_p$ as the wave period of the one third largest waves in a sea state, and varies the wave period in a certain band around this value for the design wave period. It was decided to investigate the relationship between the period of the largest waves in a sea state, and the peak period of the sea state further.

To investigate this relationship, data from 95 time series of the wave elevation for 19 different sea states over a sloping bottom (slope 1:20) from Svangstu (2011) was utilized. The characteristics of the sea states are presented in **Table 10.2**.

Table 10.2: Full scale sea state parameters obtained from time series simulated in Svangstu (2011) at the wave probe located at depth d=67.23m

Sea State	Number of simulations [-]	Mean Measured H_{m0} [m]	Mean measured T_p [s]
1	1	2.1	7.1
2	1	4.1	7.1
3	3	6.0	7.1
4	1	7.5	7.1
5	1	3.2	9.0
6	9	6.3	8.9
7	4	8.7	8.9
8	6	10.8	9.0
9	3	3.8	11.4
10	8	7.5	11.1
11	10	10.5	11.1
12	9	13.1	11.1
13	1	3.1	13.2
14	8	6.3	13.3
15	10	9.2	13.4
16	10	11.9	13.3
17	4	4.6	14.3
18	3	7.8	15.4
19	3	10.3	15.4

From these 95 time series, the significant wave height H_{m0} and spectral peak period T_p was calculated at the locations of 7 wave probes placed at depths ranging from 67.23m to 15m. At each of those 7 locations, the *three largest* wave heights during each time series[1] were found. The wave periods were taken as the time between the wave trough before and after the largest waves were observed, see **Figure 10.2**. The wave periods of the three largest waves are all denoted T_{3max}. This is to increase the number of data points to establish the relationship between T_{3max} and T_p, as for three values T_{3max} in each time series, 285 data points were known.

---

[1] The model scale time span of the *non transient* part of each time series was approximately 2 hours

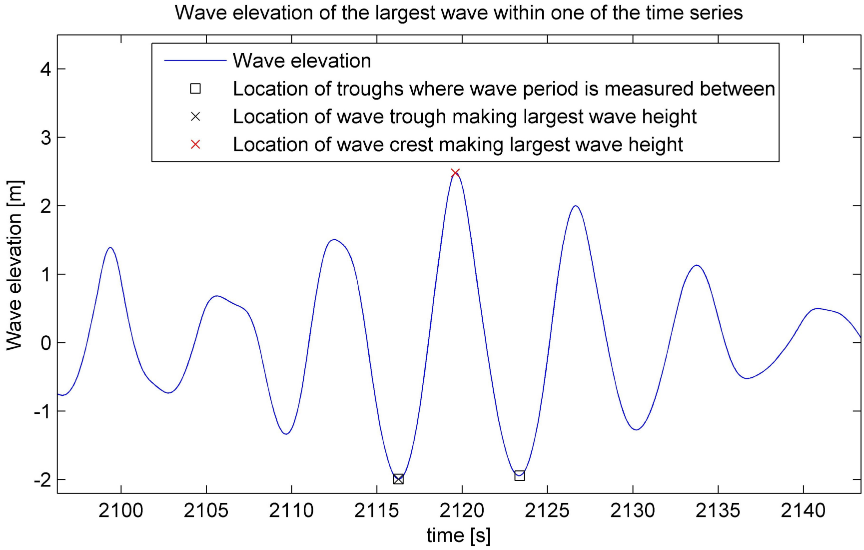

Figure 10.2: How the period of the three largest waves within each time series were found

As the spectral peak period of the sea state in each time series were known, 3 values of the parameter T_{3max}/T_p were found for each of the 95 times described in **Table 10.2**. This non-dimensional parameter was then plotted against the water depth at the location of each wave probe. The result is shown in **Figure 10.3**.

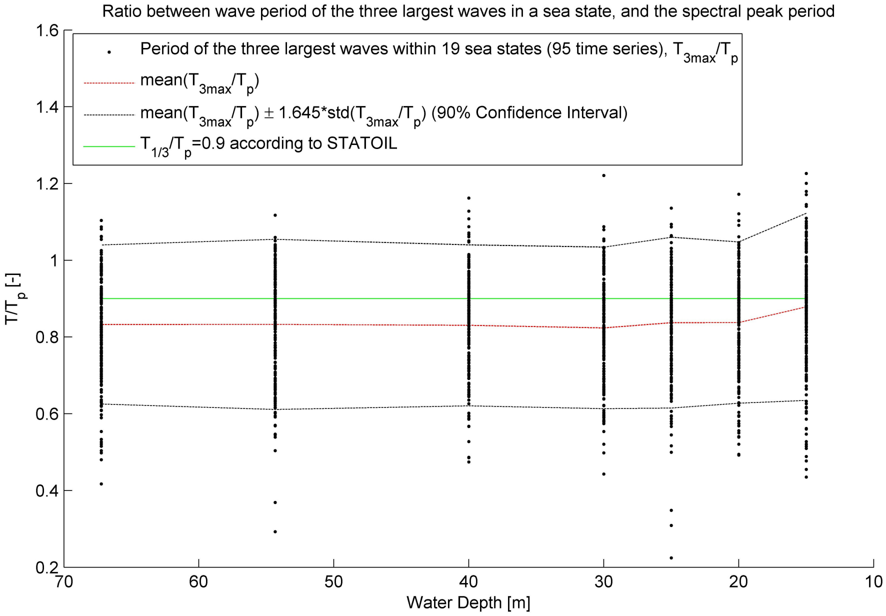

Figure 10.3: Wave period of the three largest waves in 95 time series relative to the spectral peak period of each sea state. The mean value and the 90% confidence interval of T_{3max}/T_p is shown, as well as the constant value of 0.9 used by Statoil

It is seen from **Figure 10.3** that for a water depth of 67-20m the mean value of the parameter T_{3max}/T_p is approximately constant equal to 0.83 and the standard deviation is on average 0.13 for the same depth range. This means that as a 90% confidence interval[2] is given by $mean(\frac{T_{3\max}}{T_p}) \pm 1.645 std(\frac{T_{3\max}}{T_p})$, a 90% confidence interval for the parameter T_{3max}/T_p is given by

$$0.62 \leqslant \frac{T_{3\max}}{T_p} \leqslant 1.05 \tag{10.19}$$

According to Sverre Haver, varying the wave period within the 90% confidence interval given in **Equation 10.19** is sufficient for the cause of this thesis.

As seen from **Figure 10.3** the ratio T_{3max}/T_p increases somewhat in the shallowest area (i.e. $20m < d \leqslant 15m$). This might be due to the fact that waves with shorter period will be steeper, and thus initiate breaking as they travel into sufficiently shallow water, according to the Miche criterion given in **Equation 3.3**. From this it can be reason to believe that some of the largest waves observed before the depth reaches d=15m may already have experienced wave breaking when they reach d=15m. This may in turn lead only the waves with (on average) somewhat *larger* period to "survive" without breaking into the area of 15m water depth.

Adopting the range given in **Equation 10.19**, and having the spectral peak period of the 50-year sea state found in the southern point from SWAN being $T_{p,50}$=15.56s, the 50-year design wave will have a wave height of H_{50}=12.5m and wave period $9.6s \leqslant T_{50} \leqslant 16.3s$.

---

[2] The factor 1.645 is found from taking the inverse cumulative standard normal distribution of $\frac{\alpha}{2}$, i.e. $\Phi(\frac{\alpha}{2})$, where $100(1-\alpha)$ determines the confidence level. For a 90% confidence level, α=0.1

10.3 Investigating how close the estimated 50-year design wave is to wave breaking

Assuming linear wave theory, and using the *modified* Miche's criterion as given in **Equation 3.6** with $\beta = 0.9259$, it can be visualized how close to wave breaking a wave with a given height and period is. By assuming the wave period being either $T_{50,min} = 0.62T_{p,50}$ or $T_{50,max} = 1.05T_{p,50}$, the wave length is known assuming linear theory, and thus the *theoretical maximum* wave height for a given water depth can be calculated. This has been done for the bathymetry along the path from the northern to the southern point in the Dogger Bank Case. In addition the 50-year wave height has been calculated from the Gluhovski distribution and the Battjes and Groenendijk distribution along the same path, using data from the SWAN run. The result is shown in **Figure 10.4**. The result is only shown for a water depth less than 67.23m as the relationship in **Equation 10.19** was based on a water depth less than 67.23m.

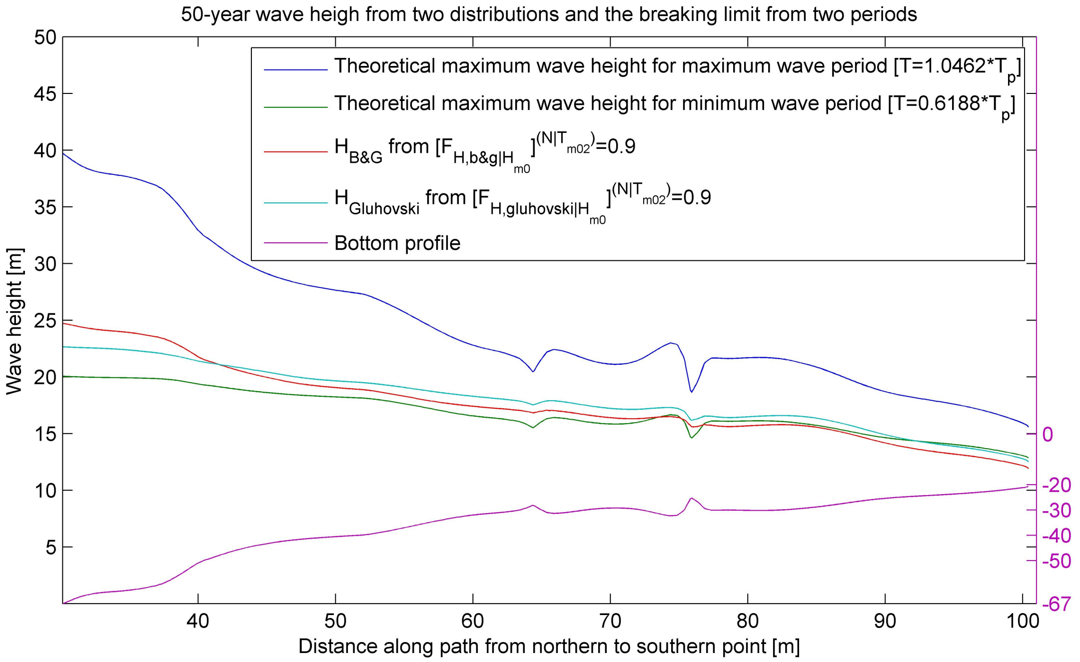

Figure 10.4: Estimated 50-year wave height and theoretical maximum wave height along the path from the northern to the southern point in the Dogger Bank Case

From **Figure 10.4** it is seen that for a water depth less than approximately 50m (occurring at a distance of approximately 40km south of the north point) the Battjes and Groenendijk distribution is less conservative than the Gluhovski distribution. It is also seen that along as the largest wave period of the range in **Equation 10.19** is assumed, the wave height is well below the breaking wave height for all values of the water depth. Assuming the smallest wave period, however, both distributions estimate a wave height which is *larger* than the theoretical largest wave height, as long as the water depth is larger than approximately 25m for the Gluhovski distribution (occurring at a distance of approximately 92km south of the north point), and as long as the water depth is larger than approximately 30m for the Battjes and Groenendijk distribution (occurring at a distance approximately 85km south of the north point). These limits are approximate, and specific for the data used in this analysis.

As mentioned previously, the Rayleigh, Næss and Forristall distribution are all more conservative than the distributions shown in **Figure 10.4**, which would have predicted unphysical large wave heights along the same path as in the figure.

For a water depth less than 25m, both distributions in **Figure 10.4** predict a 50-year wave height less than both breaking limits, although close to the lower breaking limit. This means that the predicted wave heights for this depth range can exist without breaking. Using the Gluhovski distribution, the wave height was found to be 97.4% and 80% of the breaking wave height for the shortest and longest design wave respectively. This is found using linear wave theory and the modified Miche criterion.

11. Determining the Resulting 50-year Design Loads

After determining the design wave parameters, the next step was to determine the loads from the design wave. As mentioned in **Chapter 6**, the offshore wind turbine foundations in mind for the area of interest will consist of jacket structures. These jacket structures will most likely consist of pipe-sectioned beams, so that Morison's equation will be used on each element when calculating the forces and moments on the structure. Instead of a complex jacket structure, the structure was simplified to a circular cylinder with a diameter D=6m, and a length such that it would never be totally submerged while the design wave passed the cylinder. This was done because the forces and moments will be calculated in the same way on this single cylinder as on each of the elements in the jacket structure, using the Morison's equation.

According to Faltinsen (1990), the horizontal force on a circular cylinder can, as long as the wavelength is much larger than the radius of the cylinder, be calculated using Morison's equation. This is done by separating the cylinder into n number of strips, so that the horizontal force on each strip is given by

$$dF_i(z,t) = \rho\pi\frac{D^2}{4}C_M a_{1i}(z,t) + \frac{\rho}{2}C_D D\left|u_i(z,t)\right|u_i(z,t) \tag{11.1}$$

where i indicates which strip is considered, ρ is the fluid mass density, D is the cylinder diameter, C_M is mass coefficient, C_D is the drag coefficient, $a_{1i}(z,t)$ is the horizontal undisturbed fluid acceleration at the midpoint of the strip and $u_i(z,t)$ is the horizontal undisturbed fluid velocity at the center of the strip. The fluid velocity and acceleration is positive in the direction of wave propagation. An illustration of the force on strip i is shown in **Figure 11.1**.

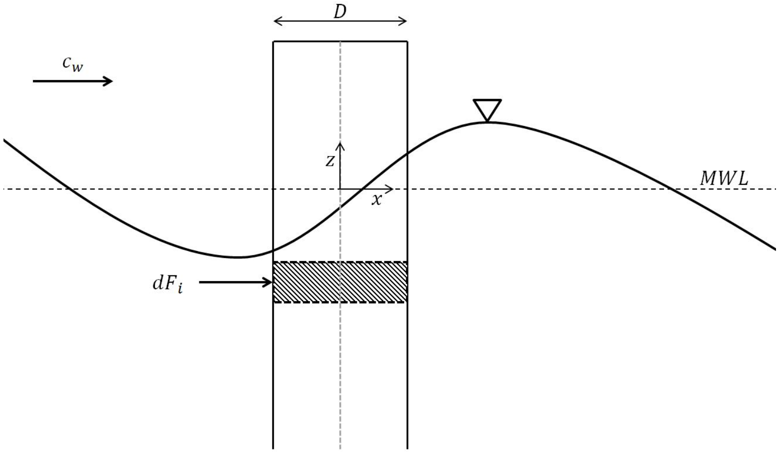

Figure 11.1: An illustration of the force on a strip of a cylinder in the passing of a wave

The total force on the cylinder is found by summing the force on every strip from the sea bed up to the free surface at the center of the cylinder, and can be written on an integral from as shown in **Equation 11.2**

$$
\begin{aligned}
F(t) &= \sum_{n} \left[\rho\pi \frac{D^2}{4} C_M a_{1i}(z,t) + \frac{\rho}{2} C_D D \left| u_i(z,t) \right| u_i(z,t) \right] \\
&= \rho\pi \frac{D^2}{4} C_M \int_{z=-d}^{z=\zeta(t)} a_1(z,t)dz + \frac{\rho}{2} C_D D \int_{z=-d}^{z=\zeta(t)} \left| u(z,t) \right| u(z,t)dz
\end{aligned}
\tag{11.2}
$$

where $\zeta(t)$ is the instantaneous wave elevation at the center of the cylinder and d is the water depth. This total force is often denoted the *base shear*.

The moment about the base of the cylinder, the *overturning moment*, is similarly found from

$$
M(t) = \rho\pi \frac{D^2}{4} C_M \int_{z=-d}^{z=\zeta(t)} a_1\left(z,t\right)\left(z+d\right)dz + \frac{\rho}{2} C_D D \int_{z=-d}^{z=\zeta(t)} \left| u\left(z,t\right) \right| u(z,t)\left(z+d\right)dz \tag{11.3}
$$

In linear theory $a_1 = \frac{\delta u}{\delta t}$, but it is important to remember that this is due to the assumption that the convective acceleration terms $u\frac{\delta u}{\delta x}$ and $v\frac{\delta u}{\delta y}$ are much smaller than the local acceleration $\frac{\delta u}{\delta t}$, Myrhaug (2006). If a nonlinear wave theory is used to calculate the kinematics of the wave, the acceleration term a_1 must be calculated from

$$
a_1 = \frac{Du}{Dt} = \frac{\delta u}{\delta t} + u\frac{\delta u}{\delta x} + v\frac{\delta u}{\delta y} \tag{11.4}
$$

as the convective terms may be comparable with the local term.

To calculate the fluid velocity and acceleration, a proper wave theory must be chosen.

11.1 Selection of appropriate wave theory

As explained in **Chapter 4**, the diagrams shown in **Figure 4.9** and **Figure 4.10** are recommended for use in choosing an appropriate wave theory, when the wave period, wave height and water depth is known, Barltrop et al. (1990). **Figure 4.9** has logarithmic scales, and shows more intervals of the stream function order compared to **Figure 4.10** which has linear scales. This may favor the use of **Figure 4.9**. It might be a tedious job to plot the value of the design wave into the diagram by hand due to small values and logarithmic scaling. To solve this problem, the software ENGAUGE DIGITIZER[1] was used to digitize the plot shown in **Figure 4.9**, so that the design wave parameters could be plotted effortlessly into the diagram using MATLAB. **Figure 11.2** show the result when plotting the design wave with the maximum and minimum wave period found in **Section 10.2**, as well as when varying the wave period within the 90%-confidence interval. The water depth is taken as 20.69m.

---

[1] Freely available from http://digitizer.sourceforge.net/

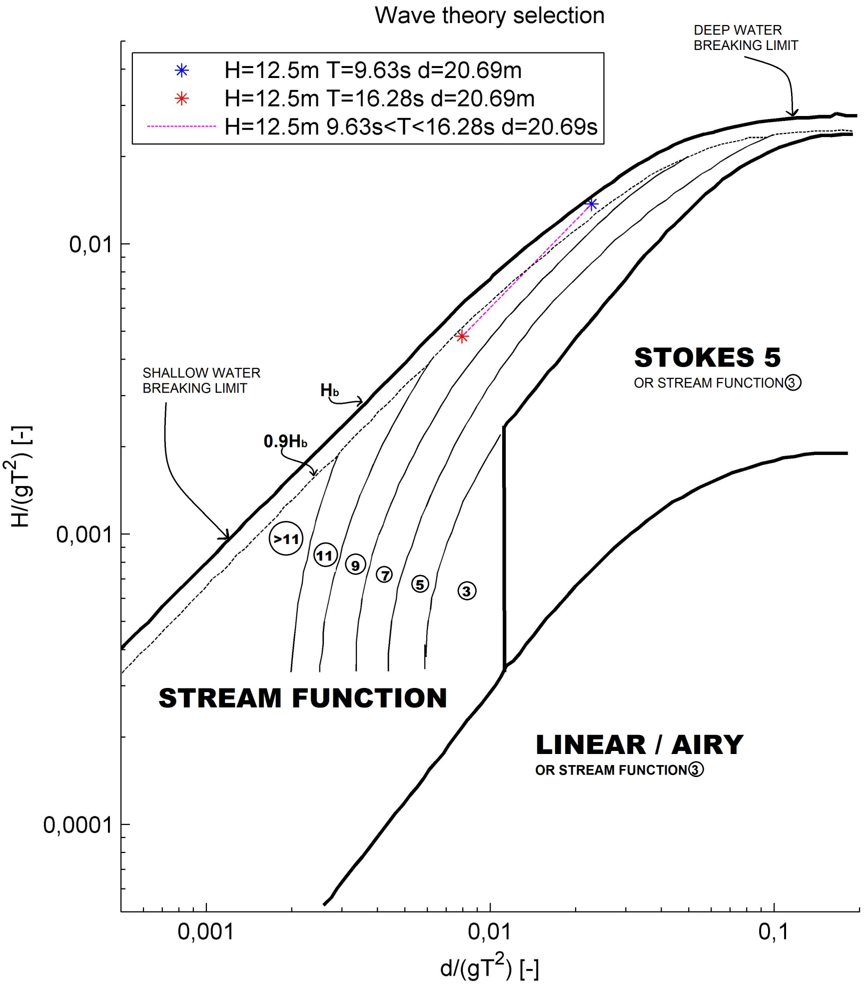

Figure 11.2: The design wave parameters plotted into a digitized version of the wave theory selection diagram proposed by Barltrop et al. (1990)

As seen from figure **Figure 11.2**, the design wave with a period of 16.3s requires the 9^{th} order of the stream function theory, while the design wave with a wave period of 9.6s requires an order larger than 11 of the stream function theory because this wave will be closer to the breaking wave limit. It should be noted that the limits in **Figure 11.2** are approximate, and for the cause of this thesis taken as a guideline.

The data obtained when digitizing the plot has been included in **Appendix D** so that others may plot the same figure as shown in **Figure 11.2** when selecting an appropriate wave theory. These values may be copied from an electronic version of this thesis and pasted into MATLAB or EXCEL etc. The values in the table in **Appendix D** are the x and y values (i.e. values of $d/(gT^2)$ and $H/(gT^2)$) for each of the lines in **Figure 11.2** numbered from 1 to 9 from left to right. It should be noted that the scales are logarithmic.

11.2 Calculating base shear and overturning moment

For both design waves, the stream function wave theory was recommended from **Figure 11.2**. The scope of work says to calculate the forces by using different wave theories, but for the chosen design waves, the stream function wave theory is the only one of interest, and will be the only theory applied. To obtain the kinematics for such a wave, the freely available program *Fourier.exe* by John D. Fenton was integrated into a MATLAB script called *FOCASTREAM*[2] (FOrce CAlculation on a cylinder subjected to a STREAM function wave). Fourer.exe solves the stream function wave using a Fourier approximation method and can be used up to an arbitrary order, and the method provides accurate solutions for waves up to very close to the highest, Fenton (2012). From FOCASTREAM, the user specifies the design wave parameters, cylinder height and diameter, drag and mass coefficient, and for how many length and phase steps the kinematics should be calculated. The kinematics are then obtained by Fourier.exe and used as input when calculating the forces from Morison's equation in FOCASTREAM. Users of FOCASTREAM are recommended to consult the user manual of Fourier.exe, Fenton (2012), when specifying the input parameters.

As recommended by Fenton (2012), one should make sure that an order of the stream wave is chosen such that the last Fourier coefficient is sufficiently small. This is to avoid a high frequency wave apparent on the free surface, and the value is found in the output file *SOLUTION.res* from Fourier.exe. According to Fenton (2012), the last Fourier coefficient of the wave elevation should be less than approximately 10^{-4}. For the design wave H=12.5m and T=16.3s, this resulted in a required order of 14. It is seen that this is higher than what was recommended by **Figure 11.2**, but is what was used in the following analysis. For the design wave H=12.5m T=9.6s the required order was found to be 22. These orders were found from trial and error until the last Fourier coefficient was sufficiently small.

The resulting maximum base shear and overturning moment obtained from FOCASTREAM was compared to the result obtained from DNV's program WAJAC, DNV (2010b), which should perform the same procedure as FOCASTREAM, to verify the result. This is presented in **Figure 11.1** where *design wave 1* is H=12.5m and T=16.3s with stream function order 14, and *design wave 2* is H=12.5m and T=9.6s with stream function order 22. The cylinder diameter was D=6m, the mass coefficient C_M=2 and drag coefficient C_D=0.81.

Table 11.1: Max base shear and overturning moment on a cylinder subjected to two design waves from FOCASTREAM, verified against WAJAC

Program	Design wave	Max Base Shear [MN]	Max Overturning Moment [MNm]
WAJAC	1	3.67	65.64
FOCASTREAM	1	3.67 / +0%	65.93 / +0.4%
WAJAC	2	3.31	61.89
FOCASTREAM	2	3.31 / +0.2%	61.72 / -0.3%

As seen from **Figure 11.1**, the largest base shear and the largest overturning moment appears for the *longest design wave*, i.e. design wave 2. This may be in contrast to what is expected, as according to Sverre Haver one would at least expect the largest overturning moment to appear for design wave 2 if the conditions were *deep water*. So the fact that the least steep wave resulted

---

[2] This MATLAB script, as the other mentioned in this thesis, is written by the author. This specific script is written with a somewhat more extensive use of commenting, so that it may be easier for others to use and possibly continue to improve

in the largest base shear and overturning moment may be a result of the nonlinearity of the wave.

The wave profiles for design wave 1 and 2 is shown in **Figure 11.3**.

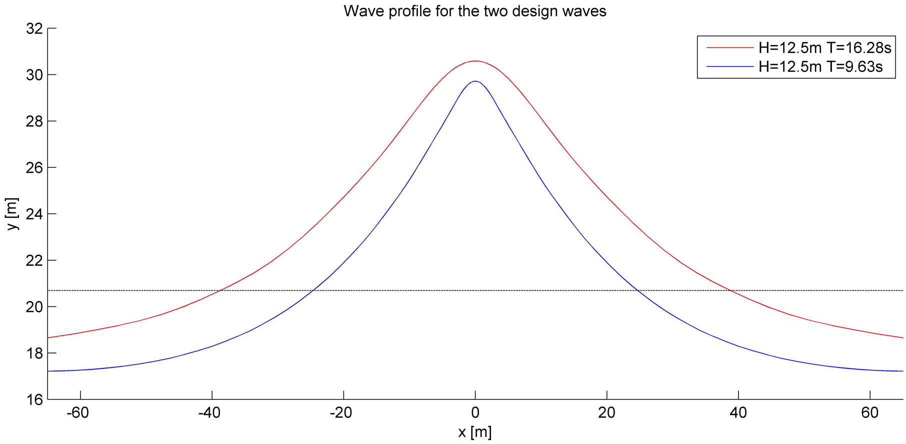

Figure 11.3: The wave profiles of the two design waves

The nonlinear property of the wave that the crest height is *higher* than the trough is *deep* is clearly visible from **Figure 11.3**. It is also seen that the two design waves does not have the same wave elevation or trough depth, but the wave height is the same.

The wave elevation at the time instance of max base shear and max overturning moment for design wave 1 is shown in **Figure 11.4**.

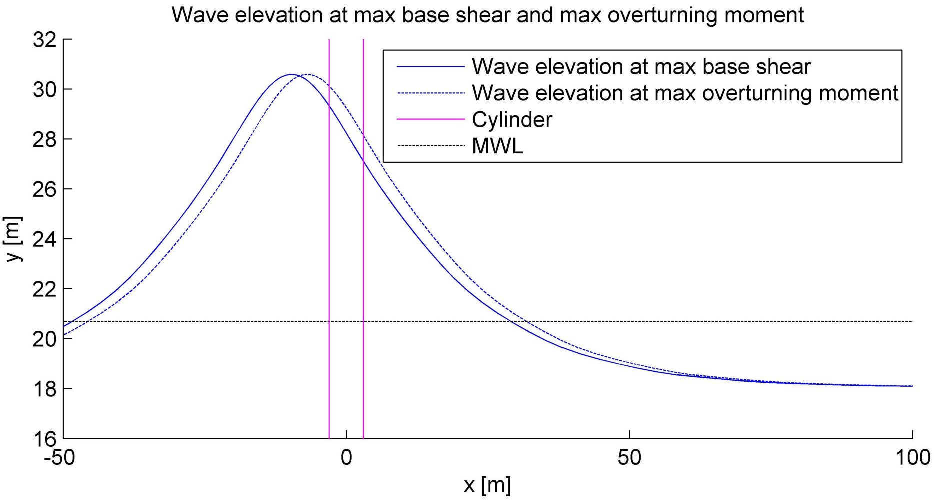

Figure 11.4: Wave elevation at time instance of max base shear and max overturning moment

From **Figure 11.4** it is seen (as the wave is travelling in the positive x-direction) that the max base shear appears *before* the max overturning moment appears. From FOCASTREAM it is found that for design wave 1, the max base shear appears at $\omega t = 6.039$ radians $= 346$ degrees and the max overturning moment appears at $\omega t = 6.109$ radians$= 350$ degrees, where ω is the wave frequency and t is the time elapsed from the first wave crest passes x=0. As the wave period is known, this is equivalent to the max base shear appearing 0.18 seconds before the max overturning moment appears.

11.2.1 Including the effect of slamming

As the design waves are relatively steep, the rate of change of added mass momentum may contribute to the sectional force when the wave hits the cylinder, DNV (2010a). The added mass momentum on a cylinder strip, here denoted by dF_{slam}, is according to DNV (2010a) given by

$$dF_{slam}(z,t) = \frac{d}{dt}\left[A^{2D}(t;z)u\right] = \frac{d}{ds}\left[A^{2D}(s;z)\right]u^2 = \frac{1}{2}\rho C_S D u^2 \tag{11.5}$$

where A^{2D} is the high-frequency limit of the added mass for a 2D cylindrical section as a function the strip submergence $s(t)$ relative to the surface. The relative horizontal velocity between the wave surface and cylinder is denoted u. The *slamming coefficient*, proposed by Campbell and Weynberg (1980), is given by

$$C_S = 5.15\left[\frac{D}{D+19s} + \frac{0.107s}{D}\right] \tag{11.6}$$

The slamming coefficient is plotted for $0 < s < D$ for a cylinder of diameter D=6m in **Figure 11.5**.

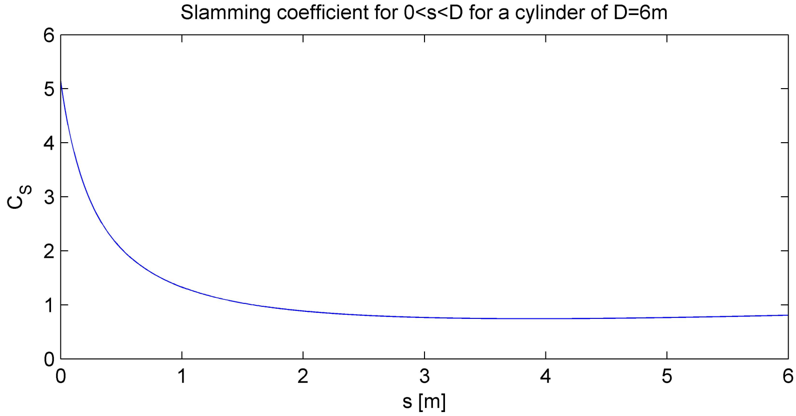

Figure 11.5: Slamming coefficient plotted for $0 < s < D$ for a cylinder of diameter D=6m

At the time instance a strip is "hit" by the wave (i.e. s=0), the slamming coefficient is 5.15, and when the strip is fully submerged the slamming coefficient is 0.81. At the time that the strip is fully submerged, i.e. when s=D, **Equation 11.5** takes the form of the drag contribution of the Morison's equation, with $C_D = C_S = 0.81$. This is why the drag coefficient of the cylinder previously was chosen ass $C_D = 0.81$.

As recommended by DNV (2010a), the forces and moments should be calculated by the classic Morison equation as given in **Equation 11.2 and 11.3** as long as the strip considered is *fully submerged*. For $s < D$ the force and moment contribution should be calculated using **Equation 11.5**. This is interpreted as shown to the left in **Figure 11.6**.

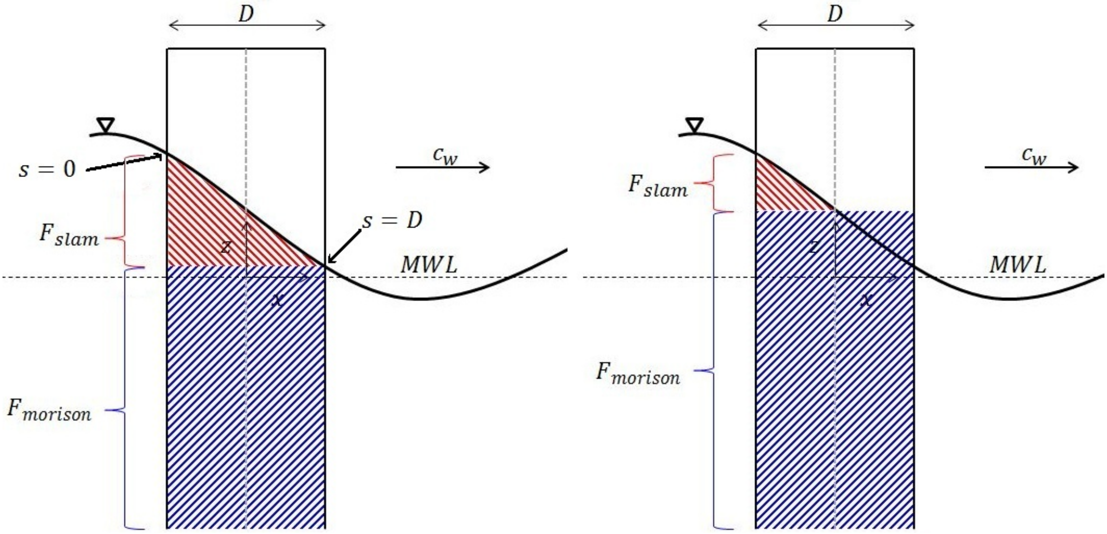

Figure 11.6: (Left:) Over what areas to integrate Morison and slamming force contribution as interpreted from DNV (2010a). (Right:) Over what areas Morison and slamming force contributions were integrated in FORCESLAM

When the procedure as presented in DNV (2010a) (i.e. as shown to the left i **Figure 11.6**) was implemented into FOCASTREAM, the resulting base shear and overturning moment were found to be *less* than what was found using the classical Morison procedure up to the wave elevation at the center of the cylinder. This is obviously wrong, and a considerable effort has been made in figuring out *why the result was wrong*. Unfortunately, without a source of verification, the fault was not found. The only conclusion drawn was that, at each time instance, the force contribution from *Morison* integrated from where $s = D$ to the wave elevation at x=0 had to be *larger* than the force contribution from slamming from where $s = D$ to where $s = 0$. As this force contribution now was *not* taken into account, the resulting base shear and overturning moment became smaller than when slamming was not considered. This means that the slamming contribution is either too small, or that the integration limits from DNV (2010a) was misinterpreted. If the slamming contribution was too small, this means that FOCASTREAM calculates this term incorrectly. A significant amount of time was spent troubleshooting the MATLAB script without success, but due to the amount of time spent on this issue, it was decided to include this in the thesis after all. If nothing else, it may help someone else in figuring this out at a later time.

To try to take the slamming into account, even though the source of this unexpected result was not found, it was determined to assume that the slamming contribution was calculated correctly, and to integrate the force contributions as shown to the right in **Figure 11.6**. The force contribution from Morison was integrated up to the wave elevation at the center of the cylinder, and the force contribution from slamming was integrated from this point and up to where s=0. Please note that this has *not* been verified as a good solution, but it gave better results, and may at least indicate how the effect of slamming may contribute to the base shear and overturning moment. The base shear and overturning moment as function of ωt for design wave 1 (i.e. H=12.5m T=16.28s) obtained from FOCASTREAM is shown in **Figure 11.7**.

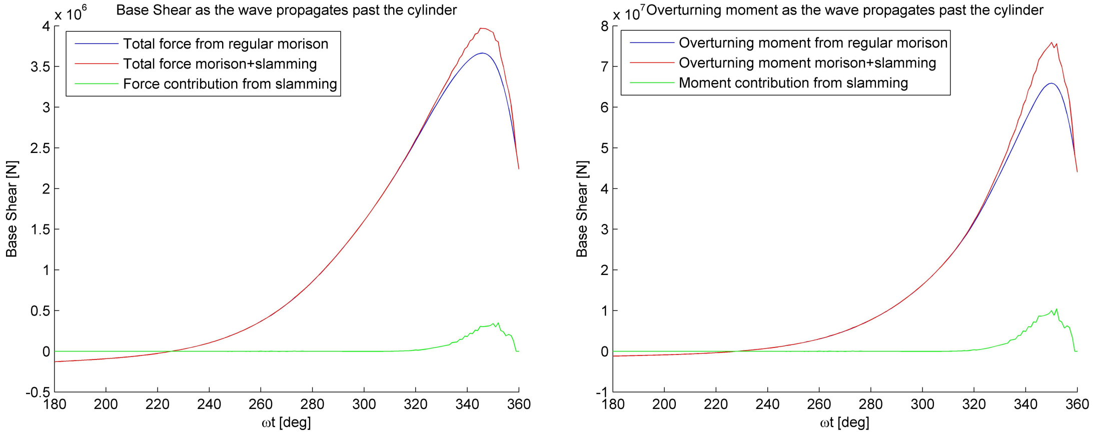

Figure 11.7: Base shear (left) and overturning moment (right) as function of ωt with and without slamming included

It is seen from **Figure 11.7** that for $\omega t < 330$ degrees (i.e. *before* the wave crest reaches the center of the cylinder), the force contribution from slamming grows, and decreases rapidly to zero when the crest reaches the center of the cylinder. As these results have not been verified, the numerical values should not be taken as accurate, but it may at least indicate when the contribution from slamming appears. The total force and overturning moment on the cylinder increases compared to the result form Morison only in this time span. For the rest of the wave cycle, the result is the same as obtained from Morison. When doing the same analysis for design wave 2 (H=12.5 T=9.63s), the increase in base shear and overturning moment due to slamming was *greater* compared to for design wave 1. This may indicate that the effect of slamming increases for increasingly steep waves.

These results should be used with care due to the lack of verification, but they may indicate that for steep waves, one should investigate how large the effect of wave slamming may be.

11.2.2 Loads from a breaking wave

As found in **Section 10.3**, the height of design wave 1 was 80% of maximum wave height, and design wave 2 was 97.4% of the maximum wave height, according to linear wave theory. As the design wave 2 is so close to the breaking limit, it indicates that it is not *unlikely* that a breaking wave may hit the wind turbine foundations at the site of interest. To estimate the forces that may act on a cylinder from a breaking wave, the simplified conservative approach of finding the maximum force from a *plunging* breaker has been performed according to the article by Wienke and Oumeraci (2005).

By using Wagner's method of the impact on a cylinder, Faltinsen (1990), Wienke and Oumeraci (2005) recommends using the formula

$$F_{\max}^{break} = 2\pi\rho\frac{D}{2}c_w^2\lambda\eta_b \tag{11.7}$$

for calculating the maximum horizontal force from a plunging breaker on a vertical cylinder. In **Equation 11.7** c_w is the phase speed of which the front of the breaking wave is assumed to travel with, λ is the *curling factor* and η_b is the breaking crest height, see **Figure 11.8**.

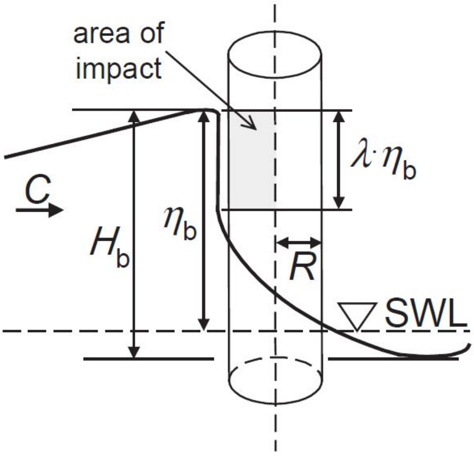

Figure 11.8: Definition sketch of a plunging breaker impacting a vertical cylinder taken from Wienke and Oumeraci (2005)

As seen from **Figure 11.8**, the area of impact is taken as $\lambda\eta_b$, where λ is the curling factor. According to Wienke and Oumeraci (2005), the curling factor is maximum λ_{max}=0.46, and has been used as the value for the curling factor in this analysis.

To calculate the impact force from a plunging breaker, the design wave 2 has been assumed to break, as it is so close to the breaking limit. From FOCASTREAM, the crest height was found to be $\eta_b = 9$m and the phase speed was found to be $c_w = 13.7$m/s. The cylinder diameter was still assumed to be D=6m and the density of sea water was set to $\rho = 1025 kg/m^3$. The resulting impact force was then found to be 15MN.

It is seen that the impact load from the breaking wave is many times larger than the max base shear found using Morison's equation from the two design waves. The duration of the impact from the breaking wave t_1 is, according to DNV (2011), given by

$$t_1 = \frac{13D}{64c_w} \tag{11.8}$$

where D is the cylinder diameter and c_w is the phase speed of the wave. For the breaking wave considered, this results in a duration of impact of t_1= 0.089s.

The dynamic amplification factor DAF (also known as the dynamic load factor DLF) describes the ratio between the maximum dynamic response and the static response of a structure. If load duration is much lower than the natural period of the structure, the inertial forces of the structure will counteract the load and lead to a dynamic reduction of response. By assuming linear structural response, this will reduce the base shear by the same factor.

According to Larsen (2009), DAF varies as a function of the shape and duration of the load as shown in **Figure 11.9**, when the structure is modeled as a single-degree-of-freedom system

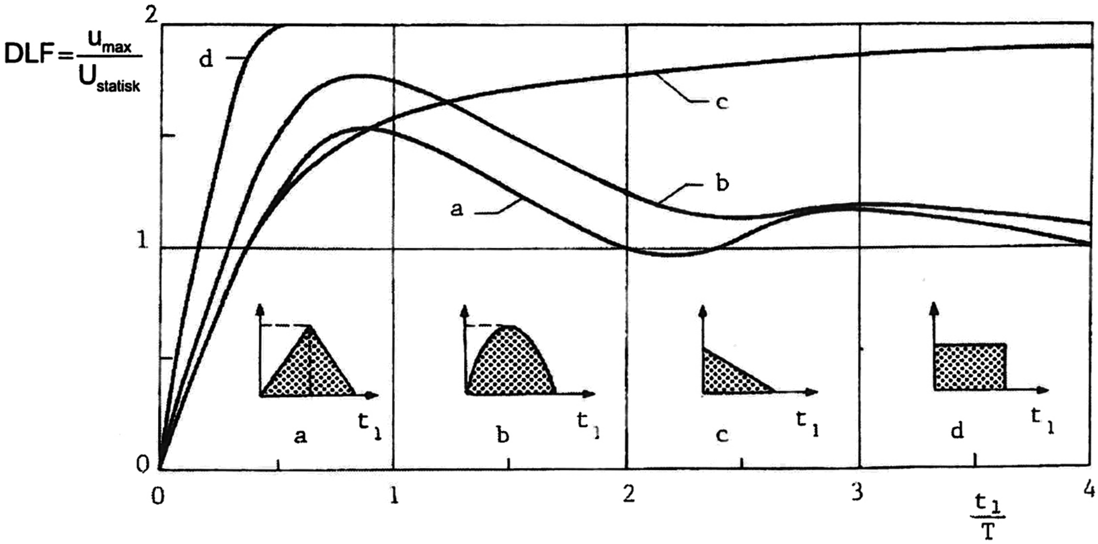

Figure 11.9: DAF as function of the shape (a-e) and duration of the load impulse t_1. T is the natural frequency (hereby denoted as T_n) of the structure of which the load acts upon

From **Figure 11.9** it is seen that for $t_1 < 0.2T_n$, where T_n is the natural period of the structure of which the load acts upon, DAF is approximately proportional to the duration of the load t_1. It can then be shown (the keen reader is referred to Larsen (2009)) that a simplified way to calculate the DAF, for $t_1 < 0.2T_n$, is given by

$$DAF = 2\pi \frac{I}{P_0 T_n} \tag{11.9}$$

where P_0 is the amplitude of the load, and I is the load impulse given by

$$I = \int_0^{t_1} P(t)dt \tag{11.10}$$

where $P(t)$ is the load as function of time.

By making the conservative assumption that the load from the breaking wave is constant in time $P(t) = P_0$ (corresponds to load shape d in **Figure 11.9**), the expression for the simplified DAF becomes

$$DAF = 2\pi \frac{t_1}{T_n} \tag{11.11}$$

According to Nordheim (2012), the requirement of the first natural period of the offshore wind turbine foundation is that it should not coincide with the $1P$ and $3P$ periods. The $1P$ period is the *fundamental rotational period*, which is the time it takes for the rotor to make a complete cycle. The $3P$ period is the *blade passing period*, which is the time it takes between every time a blade passes the wind turbine tower. The period which does not coincide with the $1P$ and $3P$ period range is small, which limits the lowest natural period of the wind turbine foundation to a small natural period range. According to figures provided by Nordheim (2012) and Krokstad (2012), it should be reasonable to assume a natural period of the offshore wind turbine foundation of 3.5s.

This means that the dynamic load factor becomes DAF=0.16 which results in an equivalent static base shear of 0.16×15MN $= 2.4$MN. By assuming that the load acts at $z = \eta_b - \frac{\lambda \eta_b}{2}$, the overturning moment caused by the impact becomes 2.4MN×27.64m=66.4MNm. From these simplified calculations, the impact from a breaking wave gives a base shear and overturning moment of such a magnitude (if compared to the values in **Table 11.1**) that an extensive analysis of the impact of a breaking wave should be performed for the offshore wind turbine foundations in the Dogger Bank Zone.

12. Summary and Conclusions

In this thesis, the effects on regular waves when propagating from deep to shallow water have been investigated, assuming linear wave theory. The effects of shoaling, refraction, reflection and diffraction have been studied. Shoaling was seen to decrease the wavelength, decrease the phase velocity, increase and then decrease the group velocity and decrease and then increase the wave amplitude. Refraction was seen to bend the wave crest so that is it more align with the bottom contours, as given by Snell's law. Reflection occurs due to the presence of a wall, or an abrupt change in water depth, and diffraction occurs due to surface penetrating bodies, or difference in amplitude along the wave crest. Both reflection and diffraction were assumed negligible relative to other mechanisms.

The process of wave breaking was also reviewed. The wave breaking criteria in deep water, corresponding to the steepest possible two-dimensional Stokes wave, resulted in wave breaking for a crest angle below 120 degrees, fluid particle velocity above the phase speed, a downward directed fluid particle acceleration above $g/2$ and a wave steepness above 0.142. It was shown that the Miche criterion describes the breaking criterion from deep to shallow water. Different types of breaking waves were described being spilling, plunging and surging breakers.

Different wave theories and how they satisfy the boundaries of the two-dimensional boundary value problem was reviewed being linear theory, second and higher order Stokes theory, Stream function theory, Solitary wave theory and Cnoidal theory. The relative validity of the different wave theories was assessed and two wave theory selection diagrams were recommended in choosing the appropriate wave theory for the problem at hand.

The effects on the wave spectrum as a sea state travels from deep to shallow water, described by the energy balance equation, has also been addressed. Shoaling was seen to increase the energy of the spectrum, and slightly shift the peak frequency to a lower frequency. The effect of wind was seen to increase the spectral density, and the energy generation was seen to increase with decreasing water depth due to a decrease in wave group velocity. Nonlinear wave-wave interactions were seen to redistribute the energy of the wave spectrum. Quadruplet wave-wave interactions were seen to redistribute energy from the peak frequency band to lower and higher frequencies, and the effect was seen to increase with decreasing water depth. Triad wave-weave interactions were seen to redistribute energy from a smaller frequency band around the peak frequency to approximately twice the peak frequency. Energy dissipation by white-capping was seen to dissipate energy proportional to the initial wave spectrum, and the effect was seen to increase with wave steepness and decreasing water depth. Dissipation by bottom friction was seen to depend on the roughness of the sea bottom and was negligible for high frequencies. The dissipation by surf-breaking was due to the depth induced breaking of waves, and was assumed proportional to the initial wave spectrum.

Two computer models for numerically solving the energy balance equation was briefly mentioned, being Swan and Stwave.

The deterministic design wave method has been assumed adequate for calculating the static extreme loading condition response of the offshore wind turbine foundations. The design wave method implies calculating the base shear and overturning moment by Morison's equation, as the design wave propagates through the model. The design wave parameters should be chosen statistically, corresponding to a return period of 50 years.

As the NORA10 hindcast was believed not to properly take the change in water depth into account at the Dogger Bank Zone, it was impossible to estimate a credible long term distribution of individual wave heights at the location of interest from this data. The hindcast data was, however, believed to yield credible data north of the Dogger Bank Zone, where the water depth was greater. This way a long term analysis could be performed on the data from NORA10 at a point north of the Dogger Bank Zone, by employing the environmental contour method.

The long term distribution of the significant wave height was estimated using both the initial distribution method and the peak over threshold method, assuming the largest waves to propagate from a northerly direction. The initial distribution method, assuming the upper tail of the distribution to be modeled as a Weibull distribution, resulted in a less conservative estimate of the 50-year significant wave height. The 50-year significant wave height north of the Dogger Bank Zone was estimated to be 11.74m. How the duration of the hindcast time series affected the estimated 50-year significant wave height was investigated. Increasing the duration was seen to reduce the variability of the estimated 50-year significant wave height. Estimating the 50-year significant wave height without the largest storm was seen to only reduce it by 3% when the time span of the hindcast was 54.3 years.

The conditional cumulative distribution of the spectral peak period was estimated assuming it to be modeled by the lognormal distribution. The peak of the 50-year environmental contour corresponded to a significant wave height of 11.74m and a spectral peak period of 15.68s, and was taken as the 50-year sea state parameters at the point north of the Dogger Bank Zone.

To investigate how the hindcast data accounted for the change in water depth from the *northern* to the *northern* point, where the *southern* point is a location south in the Dogger Bank Zone, the cumulative probability of the observed sea states and a Q-Q-plot was constructed. It was from both plots observed that the significant wave height was decreased from the northern to the southern point, confirming that the decrease in water depth is taken into account to some extent. By comparing the 30 largest storms in the northern and southern point, it was found that the 30 largest storms in the northern point resulted in 24 of the 30 largest storms in the southern point, where the significant wave height was decreased. The assumption of the worst storms to have a mean wave direction of 330-15 degrees was investigated, and it was found that the 30 largest storms, regardless of direction, had a mean wave direction of 220-15 degrees. By estimating the 50 year significant wave height *including* sea sates with a mean wave direction of 220-15 degrees, it only increased it with 1.53%, which leads to the conclusion of the initial assumption of 330-15 degrees to be sufficient.

To obtain the sea state parameters at the site of interest, the third generation wave model SWAN was used to estimate how the 50 year sea state evolves from the northern to the southern point. To better understand how the wave model works, and how the different physical effects influence the solution, a test case taken from the Master Thesis of Svangstu (2011) was analyzed in SWAN. The test case was a long crested irregular sea state, with a significant wave height of 10.5m and spectral peak period of 11.25s, over a sloping bottom of slope 1:20. The boundary conditions and bathymetry was chosen to match the model test from Svangstu (2011). The size and mesh density of the computational domain, as well as the direction and frequency resolution was chosen from sensitivity analyzes. The results from the SWAN analysis was compared to the results of the model test, and was found to give a significant wave height evolving similar to what was seen in the model tests. When the measured spectrum was used instead of a JONSWAP spectrum, it was seen to result in a smaller significant wave height. This *may* be due to the measured sea state being steeper, resulting in an increased dissipation by white-capping. The evolution of the wave spectrum as function of water depth from SWAN was seen to be close to what was observed from the model tests. The wave spectrum from SWAN, however, was seen to have more energy around a frequency band larger than the peak frequency. This may be because, as the sea state was long crested, quadruplet wave-wave interactions was not possible to model in SWAN, and quadruplet wave-wave interactions are known to redistribute energy from this frequency band.

When investigating the effects of the different physical processes in SWAN for the test case, white-capping was found to be the main source of dissipation for a water depth larger than 22m. For a water depth less than 22m, surf breaking was the main source of dissipation. Dissipation by bottom friction and redistribution by triad wave-wave interaction was seen to have a smaller effect compared to white-capping and surf-breaking. Refraction was negligible due to the nature of the bathymetry.

A short crested version of the test case was analyzed in SWAN. The effect of quadruplet-wave wave interactions was seen to increase the significant wave height. The effect of making the sea state short crested was seen to decrease the significant wave height, and is believed to be due to energy being transported out of the lateral boundaries of the domain. It was seen that if output is not taken along the centerline of the computational domain in a short crested sea state, one should investigate if the proximity of the lateral boundaries affect the solution.

With the knowledge of using SWAN acquired analyzing the test case, the 50-year sea state was simulated in the Dogger Bank case, using the default setting in SWAN. The 50-year sea state estimated at the northern point was combined with a constant wind of 23.3 m/s in the peak direction if the sea state. This wind speed was the average wind speed 6 hours before and 3 hours after the peak significant wave height, within the three worst storms from the hindcast data at the northern point. This resulted in a 50 year sea state at the location of interest characterized by a significant wave height of 7.34m and a spectral peak period of 15.56s.

The three largest storms at the northern point from the hindcast data was run in SWAN for the Dogger Bank case, to be able to say something of how results from SWAN can relate to results from NORA10. It was seen that the resulting significant wave height at the northern point from SWAN was some 15-27% lower than what was found in NORA10.

To obtain the 50 year design wave height, a short term analysis was performed on the 50-year sea state found in SWAN, according to the procedure proposed by Haver and Winterstein (2009). By assuming the individual wave heights to be modeled by the Gluhovski distribution, the 50 year design wave height was found to be 12.5m at the site of interest.

By analyzing 95 time series from model tests in Svangstu (2011), the 90% confidence interval of the ratio of the peak period and wave period of the three largest waves in the sea state was estimated to be $0.62 \leqslant \frac{T_{3\,\max}}{T_p} \leqslant 1.05$. This relationship was assumed to be valid for a water depth range of $67m \leqslant d \leqslant 20m$. From this it was estimated that the wave period of the 50 year design wave would be $9.6s \leqslant T \leqslant 16.3s$. By evaluating only the limiting values of the period range, the longest and shortest wave was found to be 80% and 97.4% of the breaking wave height respectively, assuming linear theory.

By utilizing the wave theory selection diagram, both design waves were found to require the Stream Function wave theory. By evaluating the Fourier coefficients computed by the program Fourier.exe by John D. Fenton, it was seen that the longest and shortest wave required an order of 14 and 22 respectively. By assuming the wind turbine foundation to be modeled by a circular cylinder with a diameter of 6m, the maximum base shear and overturning moment were calculated using Morison's equation. The maximum base shear and overturning moment was found to occur for the *longest* wave, and was 3.67MN and 65.93MN respectively.

It was made a significant effort in trying to calculate the effect of the rate of change of added mass momentum, but the resulting base shear and overturning moment have not been verified. However, the results may indicate that this effect is increased with increasing steepness of the waves. It was also indicated that the effect may only make the resulting base shear and overturning moment deviate from the Morison solution for a short period of time, just before the wave crest hits the cylinder.

The impact of a breaking wave was studied by a simplified and conservative approach of assuming that the steepest of the two design waves would become a plunging breaker, and break immediately in front of the cylinder. The method of Wienke and Oumeraci (2005) was applied to calculate the impact force. By assuming the maximum area of impact, the resulting impact load was found to be 15MN. The duration of the load was found to be 0.089s. By assuming the structure to be modeled as a single-degree-of-freedom system, the dynamic amplification factor was, by a simplified method, calculated to be DAF=0.16. This resulted in an equivalent static base shear and overturning moment from the breaking wave of 2.4MN and 66.4MNm respectively. The shortest 50 year design wave is so close to the breaking criteria, and the base shear and overturning moment of the breaking wave is of such a magnitude that an extensive analysis is recommended to be performed on this topic in the future.

13. Recommendations for Further Work

The following recommendations are based on the work of this thesis:

- As the reason for the significant wave height increasing when turning on quadruplet wave-wave interactions in SWAN was not discovered, this should be further assessed in the future. The reason may be obvious, but apparently not to the author at this time.
- The program FOCASTREAM should preferably be further developed to be able to correctly calculate the forces from slamming, or verify that it *does* as it is programmed today.
- The maximum base shear and overturning moment, as calculated by the Morison's equation using higher order Stream Function theory, should be verified against model tests in the future. Alternatively, or in addition, computational fluid dynamics could be applied in calculating the forces from nonlinear waves on a cylinder.
- The shortest 50 year design wave is so close to the breaking criteria, and the forces from a breaking wave is of such a magnitude, that it is highly recommended that this topic is further investigated in the future. Model tests, possibly in combination with computational fluid dynamics, should be applied in calculating the base shear and overturning moment from a breaking wave impacting the wind turbine foundation.
- The procedure outlined in this thesis has been based on quite some assumptions, such as the location of interest in the Dogger Bank Zone and the geometry of the wind turbine foundation etc. The procedure is, however, transferable to other locations where the water depth changes over a small distance compared to the resolution of the hindcast data, and for other structures such as a frame structured foundation. At least the part of the procedure concerning the design wave load calculation should be performed on a realistic structure geometry in the future.

Bibliography

Barltrop, N. D. P., Mitchell, G. and Attkins, J. (1990). *Fluid Loading on Fixed Offshore Structures: Background to the 4th Edition of Offshore Installations: Guidance on design and construction*, HMSO.

Campbell, I. and Weynberg, P. (1980). Measurement of parameters affecting slamming, *Technical report*, Southampton University.

Cavaleri, L. and Malanotte-Rizzoli, P. (1981). *Shallow water application of the third generation WAM wave model*, J. Geophys. Res.

Dean, R. G. (1965). *Stream Function Representation of Nonlinear Ocean Waves*, Journal of Geophysical Research.

Dean, R. G. (1970). *Relative Validities of Water Wave Theories*, Journal of the Waterways and Harbours Division.

Dean, R. G. (1974). Evaluation and development of water wave theories for engineering application vol. i, *Technical report*, Department of the Army Coastal Engineering Research Center.

Dean, R. G. and Dalrymple, R. A. (1991). *Water Wave Mechanics for Engineers and Scientists*, World Scientific.

DNV (2010a). *DNV-RP-C205 Environmental Conditions And Environmental Loads.*

DNV (2010b). *SESAM User Manual Wajac.*

DNV (2011). *DNV-OS-J101 Design of Offshore Wind Turbine Structures.*

Faltinsen, O. M. (1990). *Sea Loads on Ships and Offshore Structures*, Cambridge University Press.

Fenton, J. D. (2012). *Use of the program FOURIER for steady waves.*

Goda, Y. (2010). *Random Seas and Design of Maritime Structures*, Wold Scientific.

Hameed, T. S. S. and Baba, M. (1985). *Wave Height Distribution in Shallow Water*, Pergamon Press Ltd.

Haver, S. K. (2011a). Overview of mechanisms involved in modifying waves from deep water to shallow water (draft), *Technical report*, Statoil.

Haver, S. K. (2011b). Prediction of characteristic response for design purposes, (preliminary version), *Technical report*, Statoil.

Haver, S. and Nyhus, K. (1986). *A Wave Climate Description for Long Term Response Calculations*, Proceedings of the Fifth International Offshore Mechanics and Arctic Engineering Symposium.

Haver, S. and Winterstein, S. (2009). *Environmental Contour Lines: A Method for Estimating Long Term Extremes by a Short Term Analysis*, Society of Naval Architects and Marine Engineers.

Holthuijsen, L. H. (2007). *Waves in Oceanic and Coastal Waters*, Cambridge University Press.

Krokstad, J. R. (2012). *Statiol Developments AS, Powerpoint presentation, 28th March.*

Larsen, C. M. (2009). *TMR4180 MARIN DYNAMIKK*, Institutt for Marin Teknikk.

Leira, B. J., Moan, T., Haver, S. and Spidsøe, N. (2010). *Stochastic Theory of Sealoads - Probabilistic Modeling and Estimation*, Institutt for Marin Teknikk.

Méhauté, B. L. (1976). *An Introduction to Hydrodynamics and Water Waves*, Springer-Verlag.

Miles, J. W. (1957). *On the generation of surface waves by shear flows*, J. Fluid Mech.

Myrhaug, D. (2006). *TMR4230 - OCEANOGRAPHY: Wind, Waves*, Institutt for Marin Teknikk.

Myrhaug, D. (2007). *TMR4180 MARIN DYNAMIKK: Uregelmessig Sjø*, Institutt for Marin Teknikk.

Næss, A. (1985). *The joint crossing frequency of stochastic processes and its application to wave theory*, Journal of Applied Ocean Research.

Nordheim, K. (2012). *Statiol, Email correspondence, 8th June.*

Pettersen, B. (2007). *TM4247 - MARIN TEKNIKK 3: Hydrodynamikk*, Institutt for Marin Teknikk.

Reistad, M. (2011). *The Norwegian Institute of Meteorology, Email correspondence, 7th Nov.*

Sarpkaya, T. and Isaacson, M. (1981). *Mechanics of Wave Forces on Offshore Structures*, Van Nostrand Reinhold Company.

Soulsby, R. (1997). *Dynamics of Marine Sands*, Thomas Telford Publications.

Svangstu, E. (2011). An investigation of wave conditions and wave induced loads for design of wind turbine foundations at 15 40m depth., *Technical report*, NTNU.

Svendsen, I. A. (2006). *Introduction to Nearshore Hydrodynamics*, World Scientific.

SWAN (2006). *SWAN User Manual for SWAN Cycle III version 40.85*, The SWAN team.

SWAN (2011). *SWAN Scientific and Technical Documentation for SWAN Cycle III version 40.85*, The SWAN team.

Wienke, J. and Oumeraci, H. (2005). Breaking wave impact force on a vertical and inclined slender piletheoretical and large-scale model investigations, *Technical report*, Coastal Engineering.

Winterstein, S. R. (2011). Modelling of shallow water surface elevation process, *Technical report*, Statoil Internal Report.

Appendices

A. Expression for shoaling coefficient derived

The expression for the shoaling coefficient is, as given in **Equation 2.22**:

$$\frac{\zeta_a}{\zeta_{a0}} = K_{sh} = \sqrt{\frac{c_{g0}}{c_g}}$$

The expression for the deep water group velocity is obtained from combining the equation of group velocity in arbitrary water (**Equation 2.14**) and the deep water dispersion relation:

$$c_{g0} = \frac{1}{2}\frac{\omega_0}{k_0} = \frac{1}{2}\frac{g}{\omega_0} \tag{A.1}$$

By inserting **Equation A.1 and 2.14** into the expression for the shoaling coefficient, it can be expressed as

$$K_s = \sqrt{\frac{\frac{1}{2}\frac{g}{\omega_0}}{\left[\frac{2kd}{\sinh(2kd)} + 1\right]\frac{1}{2}\frac{\omega}{k}}} \tag{A.2}$$

As proven in **Section 2.1**, the frequency is constant, which means $\omega_0 = \omega$ and the shoaling coefficient simplifies to

$$K_s = \sqrt{\frac{g}{\left[\frac{2kd}{\sinh(2kd)} + 1\right]\frac{\omega^2}{k}}} \tag{A.3}$$

The dispersion relation in arbitrary water can be expressed by $\frac{\omega^2}{k} = g\tanh(kd)$, which inserted in **Equation A.3** results in the shoaling coefficient as a function of *normalized water depth kd*

$$K_s = \left(\left[\frac{2kd}{\sinh(2kd)} + 1\right]\tanh(kd)\right)^{-0.5} \tag{A.4}$$

B. Scatter diagram

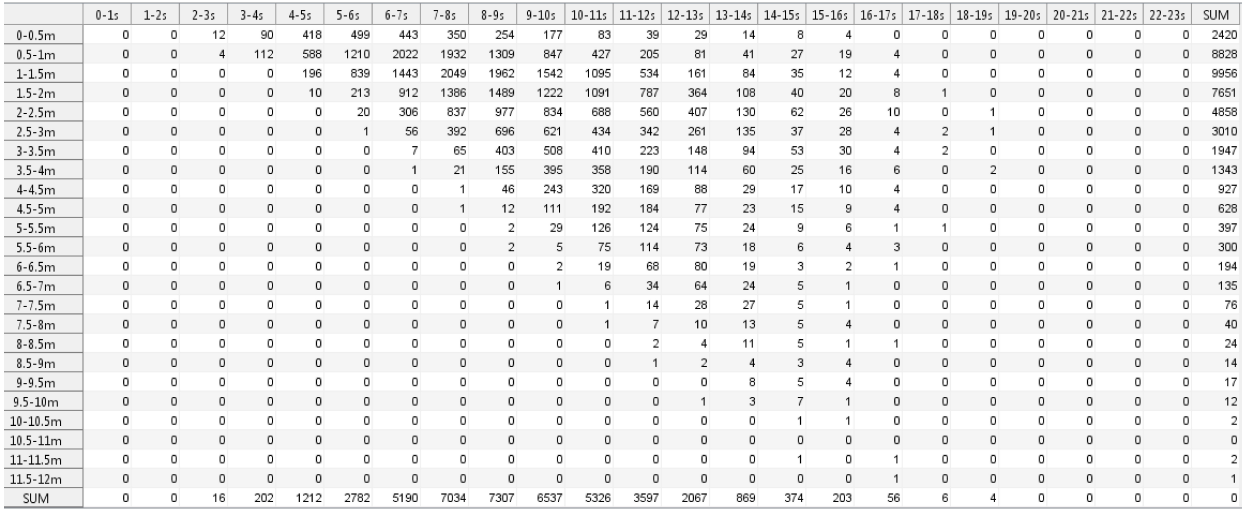

	0-1s	1-2s	2-3s	3-4s	4-5s	5-6s	6-7s	7-8s	8-9s	9-10s	10-11s	11-12s	12-13s	13-14s	14-15s	15-16s	16-17s	17-18s	18-19s	19-20s	20-21s	21-22s	22-23s	SUM
0-0.5m	0	0	12	90	418	499	443	350	254	177	83	39	29	14	8	4	0	0	0	0	0	0	0	2420
0.5-1m	0	0	4	112	588	1210	2022	1932	1309	847	427	205	81	41	27	19	4	0	0	0	0	0	0	8828
1-1.5m	0	0	0	0	196	839	1443	2049	1962	1542	1095	534	161	84	35	12	4	0	0	0	0	0	0	9956
1.5-2m	0	0	0	0	10	213	912	1386	1489	1222	1091	787	364	108	40	20	8	1	0	0	0	0	0	7651
2-2.5m	0	0	0	0	0	20	306	837	977	834	688	560	407	130	62	26	10	0	1	0	0	0	0	4858
2.5-3m	0	0	0	0	0	1	56	392	696	621	434	342	261	135	37	28	4	2	1	0	0	0	0	3010
3-3.5m	0	0	0	0	0	0	7	65	403	508	410	223	148	94	53	30	4	2	0	0	0	0	0	1947
3.5-4m	0	0	0	0	0	0	1	21	155	395	358	190	114	60	25	16	6	0	2	0	0	0	0	1343
4-4.5m	0	0	0	0	0	0	0	1	46	243	320	169	88	29	17	10	4	0	0	0	0	0	0	927
4.5-5m	0	0	0	0	0	0	0	1	12	111	192	184	77	23	15	9	4	0	0	0	0	0	0	628
5-5.5m	0	0	0	0	0	0	0	0	2	29	126	124	75	24	9	6	1	1	0	0	0	0	0	397
5.5-6m	0	0	0	0	0	0	0	0	2	5	75	114	73	18	6	4	3	0	0	0	0	0	0	300
6-6.5m	0	0	0	0	0	0	0	0	0	2	19	68	80	19	3	2	1	0	0	0	0	0	0	194
6.5-7m	0	0	0	0	0	0	0	0	0	1	6	34	64	24	5	1	0	0	0	0	0	0	0	135
7-7.5m	0	0	0	0	0	0	0	0	0	0	1	14	28	27	5	1	0	0	0	0	0	0	0	76
7.5-8m	0	0	0	0	0	0	0	0	0	0	1	7	10	13	5	4	0	0	0	0	0	0	0	40
8-8.5m	0	0	0	0	0	0	0	0	0	0	0	2	4	11	5	1	1	0	0	0	0	0	0	24
8.5-9m	0	0	0	0	0	0	0	0	0	0	0	1	2	4	3	4	0	0	0	0	0	0	0	14
9-9.5m	0	0	0	0	0	0	0	0	0	0	0	0	0	8	5	4	0	0	0	0	0	0	0	17
9.5-10m	0	0	0	0	0	0	0	0	0	0	0	0	1	3	7	1	0	0	0	0	0	0	0	12
10-10.5m	0	0	0	0	0	0	0	0	0	0	0	0	0	0	1	1	0	0	0	0	0	0	0	2
10.5-11m	0	0	0	0	0	0	0	0	0	0	0	0	0	0	0	0	0	0	0	0	0	0	0	0
11-11.5m	0	0	0	0	0	0	0	0	0	0	0	0	0	0	1	0	1	0	0	0	0	0	0	2
11.5-12m	0	0	0	0	0	0	0	0	0	0	0	0	0	0	0	0	1	0	0	0	0	0	0	1
SUM	0	0	16	202	1212	2782	5190	7034	7307	6537	5326	3597	2067	869	374	203	56	6	4	0	0	0	0	0

C. Derivation of linear velocity potential

Using the method of separation of variables and write the velocity potential as

$$\phi = F(z)G(x - ct) \tag{C.1}$$

where c is the phase speed of the propagating wave.

Substituting this into the Laplace equation, we get

$$\begin{aligned} \frac{\delta^2 \phi}{\delta x^2} &= \frac{\delta^2 \phi}{\delta z^2} \\ -\frac{\ddot{G}}{G} &= \frac{F^{''}}{F} = k^2 \end{aligned} \tag{C.2}$$

where $\ddot{G} = \frac{\delta^2 G(kx - \omega t)}{\delta x^2}$ and $F^{''} = \frac{\delta^2 F(z)}{\delta z^2}$. This gives us two ordinary differential equations:

$$\ddot{G} + Gk^2 = 0 \tag{C.3}$$

$$F^{''} - Fk^2 = 0 \tag{C.4}$$

The solution of the characteristic equation for **Equation C.3 and C.4** respectively is

$$\gamma = \pm\sqrt{-k^2} \tag{C.5}$$

$$\gamma = \pm\sqrt{k^2} \tag{C.6}$$

A non-trivial solution is obtained for $k^2 > 0$, which yields the following solutions for **Equation C.3 and C.4**:

$$G = A_1 \sin(k(x - ct)) + A_2 \cos(k(x - ct)) \tag{C.7}$$

$$F = A_3 e^{kz} + A_4 e^{-kz} \tag{C.8}$$

The wave elevation is expressed in **Equation 4.15** as

$$\zeta = -\frac{1}{g}\left(\frac{\delta \phi}{\delta t}\right)_{z=0} = -\frac{1}{g}\left(F\frac{\delta G}{\delta t}\right)_{z=0} \tag{C.9}$$

The time t is defined as zero when a wave crest passes through x=0. This means that $\left(\frac{\delta \zeta}{\delta x}\right) = 0$ or

$$\left(\frac{\delta \zeta}{\delta x}\right)_{x=z=t=0} = -\frac{1}{g}\left(F\frac{\delta^2 G}{\delta t dx}\right)_{x=z=t=0} = 0 \tag{C.10}$$

From this we get that

$$\left(\frac{\delta^2 G}{\delta t dx}\right)_{x=z=t=0} = 0 \;\rightarrow\; A_2 = 0 \tag{C.11}$$

Which means that **Equation C.3** takes the form

$$G = A_1 \sin(k(x - ct)) \tag{C.12}$$

According to Svendsen (2006) we can conveniently call A_3 and A_4 in **Equation C.8** for

$$A_3 = \frac{A+B}{2} A_4 = \frac{A-B}{2} \tag{C.13}$$

which gives us **Equation C.8** on the form

$$\begin{aligned} F &= \frac{A+B}{2} e^{kz} + \frac{A-B}{2} e^{-kz} \\ &= A\frac{e^{kz} + e^{-kz}}{2} + B\frac{e^{kz} - e^{-kz}}{2} \\ &= A\cosh(kz) + B\sinh(kz) \end{aligned} \tag{C.14}$$

Using the bottom boundary condition given in **Equation 4.5**, we get that

$$\left(\frac{\delta\phi}{\delta z}\right)_{z=-d} = \left(G\frac{\delta F}{\delta z}\right)_{z=-d} = 0 \tag{C.15}$$

A non-trivial solution then yields that

$$\left(G\frac{\delta F}{\delta z}\right)_{z=-d} = -Ak\sinh(kd) + Bk\cosh(kd) = 0 \tag{C.16}$$

which gives

$$A = B\frac{\cosh(kd)}{\sinh(kd)} \tag{C.17}$$

Inserting **Equation C.17** into the expression for F we get

$$F = \frac{B}{\sinh(kd)}\left[\cosh(kd)\cosh(kz) + \sinh(kd)\sinh(kz)\right] \tag{C.18}$$

which by the hyperbolic addition theorem becomes

$$F = B\frac{\cosh(k(z+d))}{\sinh(kd)} \tag{C.19}$$

By inserting the expressions for F and G into the **Equation C.1**, and using **Equation 2.7** for the expression of the phase speed, the expression for the velocity potential becomes

$$\phi(x,z,t) = C\frac{\cosh(k(z+d))}{\sinh(kd)}\sin(kx - \omega t)) \tag{C.20}$$

where $C = B + A_1$.

By inserting the expression for the velocity potential into the dynamic free surface condition we get the expression for the wave elevation:

$$\begin{aligned} \zeta &= -\frac{1}{g}\frac{\delta\phi}{\delta t} \text{ on } z = 0 \\ \zeta(x,t) &= \frac{\omega C}{g\tanh(kd)}\cos(kx-\omega t) = \zeta_a\cos(kx-\omega t) \end{aligned} \tag{C.21}$$

where we can see that the wave amplitude is $\zeta_a = \frac{\omega C}{g\tanh(kd)}$. From this we can substitute C into **Equation C.20** and get the final expression for the linearized velocity potential

$$\phi = \frac{\zeta_a g}{\omega}\frac{\cosh(k(z+d))}{\cosh(kd)}\sin(kx-\omega t)) \tag{C.22}$$

D. Wave theory selection diagram data

1		2		3		4		5	
$d/(gT^2)$	$H/(gT^2)$	$d/(gT^2)$	$H/(gT^2)$	$d/(gT^2)$	$H/(gT^2)$	$d/(gT^2)$	$H/(gT^2)$	$d/(gT^2)$	$H/(gT^2)$
4.87650E-04	3.91106E-04	4.87270E-04	3.20099E-04	1.98630E-03	3.34755E-04	2.50770E-03	3.34755E-04	3.37108E-03	3.37688E-04
5.14721E-04	4.15660E-04	5.18969E-04	3.43166E-04	2.00474E-03	3.71691E-04	2.50804E-03	3.52740E-04	3.37207E-03	3.78232E-04
5.48188E-04	4.41748E-04	5.52712E-04	3.64704E-04	2.02325E-03	4.05565E-04	2.55399E-03	3.84887E-04	3.37307E-03	4.23643E-04
5.83830E-04	4.69474E-04	5.78168E-04	3.84244E-04	2.04193E-03	4.42527E-04	2.57758E-03	4.19964E-04	3.40421E-03	4.62252E-04
6.21769E-04	4.94613E-04	6.15739E-04	4.04819E-04	2.06078E-03	4.82857E-04	2.57816E-03	4.58238E-04	3.43565E-03	5.04380E-04
6.62217E-04	5.30255E-04	6.55773E-04	4.30227E-04	2.07981E-03	5.26862E-04	2.60197E-03	5.00000E-04	3.49859E-03	5.50347E-04
6.98979E-04	5.63544E-04	7.04748E-04	4.65258E-04	2.09902E-03	5.74878E-04	2.64964E-03	5.45568E-04	3.53090E-03	6.00503E-04
7.44426E-04	5.98915E-04	7.50569E-04	4.94460E-04	2.13748E-03	6.27270E-04	2.69813E-03	5.90119E-04	3.59559E-03	6.55231E-04
7.92827E-04	6.36505E-04	7.99370E-04	5.25494E-04	2.17659E-03	6.78494E-04	2.74756E-03	6.43900E-04	3.66139E-03	7.08737E-04
8.44375E-04	6.76454E-04	8.66834E-04	5.73245E-04	2.19669E-03	7.40329E-04	2.79790E-03	7.02582E-04	3.76205E-03	7.73328E-04
8.99275E-04	7.18911E-04	9.23194E-04	6.09225E-04	2.25708E-03	8.07799E-04	2.87482E-03	7.66613E-04	3.83098E-03	8.43806E-04
9.57745E-04	7.64032E-04	9.83219E-04	6.47462E-04	2.31950E-03	9.36909E-04	2.95379E-03	8.29215E-04	3.93621E-03	9.12712E-04
1.02002E-03	8.11986E-04	1.04722E-03	7.00192E-04	2.38327E-03	1.02229E-03	3.00791E-03	9.04786E-04	4.04443E-03	9.95892E-04
1.08634E-03	8.62949E-04	1.12531E-03	7.37674E-04	2.42688E-03	1.10578E-03	3.09054E-03	9.78671E-04	4.19295E-03	1.07722E-03
1.14664E-03	9.17125E-04	1.19848E-03	7.83973E-04	2.49360E-03	1.20655E-03	3.17551E-03	1.06786E-03	4.30813E-03	1.16518E-03
1.22119E-03	9.74687E-04	1.27649E-03	8.47820E-04	2.56216E-03	1.31651E-03	3.26273E-03	1.15506E-03	4.46643E-03	1.27137E-03
1.30059E-03	1.03586E-03	1.37168E-03	8.93205E-04	2.63254E-03	1.42402E-03	3.38262E-03	1.26033E-03	4.63045E-03	1.37519E-03
1.36050E-03	1.09136E-03	1.44782E-03	9.49280E-04	2.70485E-03	1.54030E-03	3.47554E-03	1.36325E-03	4.75764E-03	1.48749E-03
1.44895E-03	1.15986E-03	1.56996E-03	1.02656E-03	2.77922E-03	1.68068E-03	3.60317E-03	1.47458E-03	4.97677E-03	1.60896E-03
1.54316E-03	1.23266E-03	1.67204E-03	1.09099E-03	2.90742E-03	1.86612E-03	3.73549E-03	1.59499E-03	5.15953E-03	1.74035E-03
1.64344E-03	1.29866E-03	1.78075E-03	1.15947E-03			3.87275E-03	1.74035E-03	5.39716E-03	1.88247E-03
1.75029E-03	1.38017E-03	1.87967E-03	1.24304E-03			4.01496E-03	1.88247E-03	5.59536E-03	2.03619E-03
1.84746E-03	1.46682E-03	2.00181E-03	1.30960E-03			4.16240E-03	2.03619E-03	5.85307E-03	2.20247E-03
1.96758E-03	1.55888E-03	2.13197E-03	1.39179E-03			4.35411E-03	2.20247E-03	6.12251E-03	2.36163E-03
2.09551E-03	1.65672E-03	2.27066E-03	1.49209E-03			4.51390E-03	2.36163E-03	6.40450E-03	2.55448E-03
2.23175E-03	1.76070E-03	2.41830E-03	1.58574E-03			4.72180E-03	2.55448E-03	6.69948E-03	2.76309E-03
2.37686E-03	1.87121E-03	2.57553E-03	1.68526E-03			4.93928E-03	2.76309E-03	7.00788E-03	2.96277E-03
2.53140E-03	1.98865E-03	2.84333E-03	1.82241E-03			5.16677E-03	2.98872E-03	7.33065E-03	3.20471E-03
2.69598E-03	2.11347E-03	3.00127E-03	1.95376E-03			5.40462E-03	3.20471E-03	7.73717E-03	3.43630E-03
2.87127E-03	2.24612E-03	3.34363E-03	2.18763E-03			5.65355E-03	3.46640E-03	8.16623E-03	3.68463E-03
3.05796E-03	2.38709E-03	3.56103E-03	2.32494E-03			6.24189E-03	4.02043E-03	8.61908E-03	3.95091E-03
3.25678E-03	2.53692E-03	3.79243E-03	2.44943E-03					9.09704E-03	4.23643E-03
3.46853E-03	2.69614E-03	4.03928E-03	2.64891E-03					9.60129E-03	4.50314E-03
3.69405E-03	2.86536E-03	4.30176E-03	2.79075E-03					1.01337E-02	4.82857E-03
3.89912E-03	3.04525E-03	4.62287E-03	2.99182E-03					1.07920E-02	5.17752E-03
4.15263E-03	3.23638E-03	4.83579E-03	3.15211E-03					1.13905E-02	5.55168E-03
4.42263E-03	3.43951E-03	5.15020E-03	3.34995E-03					1.21301E-02	5.90119E-03
4.71018E-03	3.65538E-03	6.00114E-03	3.81659E-03					1.28025E-02	6.27270E-03
5.01643E-03	3.88481E-03	6.33450E-03	4.09168E-03					1.36338E-02	6.66761E-03
5.34277E-03	4.16475E-03	6.74635E-03	4.34849E-03					1.45194E-02	7.14946E-03
5.63936E-03	4.42622E-03	7.18524E-03	4.66185E-03					1.53242E-02	7.59956E-03
6.00603E-03	4.70402E-03	8.75831E-03	5.64475E-03					1.64663E-02	8.07799E-03
6.39653E-03	4.99926E-03	9.32745E-03	5.94701E-03					1.73790E-02	8.58655E-03
6.81242E-03	5.31304E-03	1.00234E-02	6.32017E-03					1.85075E-02	9.12712E-03
7.65812E-03	6.00099E-03	1.04847E-02	6.60104E-03					1.97093E-02	9.70172E-03
8.15604E-03	6.37763E-03	1.11660E-02	6.95450E-03					2.09891E-02	1.03125E-02
8.68603E-03	6.71913E-03	1.18920E-02	7.39099E-03					2.23520E-02	1.09617E-02
9.33409E-03	7.14074E-03	1.30108E-02	7.92325E-03					2.38035E-02	1.16518E-02
9.94064E-03	7.52310E-03	1.38563E-02	8.34751E-03					2.55774E-02	1.23854E-02
1.02130E-02	7.78951E-03	1.57151E-02	9.18505E-03					2.69946E-02	1.30508E-02
1.08767E-02	8.20661E-03	1.67369E-02	9.76153E-03					2.90063E-02	1.38724E-02
1.16882E-02	8.72156E-03	1.79850E-02	1.02841E-02					3.08891E-02	1.46177E-02
1.24477E-02	9.18857E-03	1.91537E-02	1.08348E-02					3.31904E-02	1.54030E-02
1.33764E-02	9.76513E-03	2.05821E-02	1.14147E-02					3.56631E-02	1.62306E-02
1.43739E-02	1.02879E-02	2.21169E-02	1.20258E-02					3.83200E-02	1.71026E-02
1.53080E-02	1.08387E-02	2.33439E-02	1.26699E-02					4.11739E-02	1.78649E-02
1.64495E-02	1.14190E-02	2.50847E-02	1.33481E-02					4.46388E-02	1.86612E-02
1.76762E-02	1.20302E-02	2.69554E-02	1.40627E-02					4.97179E-02	2.00098E-02
1.88248E-02	1.26744E-02	2.92263E-02	1.48152E-02						
2.02287E-02	1.33529E-02	3.14058E-02	1.56083E-02						
2.17372E-02	1.40677E-02	3.37467E-02	1.63012E-02						
2.33582E-02	1.48207E-02	3.62633E-02	1.71738E-02						
2.51001E-02	1.56141E-02	3.93171E-02	1.79360E-02						
2.69709E-02	1.63072E-02	4.58024E-02	1.92257E-02						
2.87235E-02	1.71804E-02	4.96578E-02	1.99047E-02						
3.11435E-02	1.80998E-02	5.38378E-02	2.06078E-02						
3.34648E-02	1.89034E-02	5.83696E-02	2.13356E-02						
3.62830E-02	1.97423E-02	6.55935E-02	2.20879E-02						
3.89874E-02	2.06187E-02	7.17504E-02	2.24728E-02						
4.22692E-02	2.13469E-02	7.77848E-02	2.28647E-02						
4.42115E-02	2.19105E-02	8.13563E-02	2.32648E-02						
4.79330E-02	2.26844E-02	8.81926E-02	2.32617E-02						
5.19661E-02	2.32819E-02	9.39044E-02	2.32593E-02						
5.68458E-02	2.38949E-02	1.01805E-01	2.38720E-02						
6.16266E-02	2.43116E-02	1.11358E-01	2.40773E-02						
6.74135E-02	2.49516E-02	1.21806E-01	2.42844E-02						
7.30832E-02	2.53867E-02	1.27390E-01	2.42826E-02						
7.99431E-02	2.58291E-02	1.39343E-01	2.44914E-02						
8.74470E-02	2.62791E-02	1.59399E-01	2.44860E-02						
9.39522E-02	2.65059E-02	1.72799E-01	2.46969E-02						
1.02768E-01	2.67339E-02	1.89000E-01	2.44791E-02						
1.10412E-01	2.69646E-02								
1.20772E-01	2.71965E-02								
1.32100E-01	2.71925E-02								
1.44494E-01	2.74264E-02								
1.58046E-01	2.74223E-02								
1.65309E-01	2.81463E-02								
1.79187E-01	2.76565E-02								
1.95993E-01	2.76524E-02								

6		**7**		**8**		**9**	
$d/(gT^2)$	$H/(gT^2)$	$d/(gT^2)$	$H/(gT^2)$	$d/(gT^2)$	$H/(gT^2)$	$d/(gT^2)$	$H/(gT^2)$
1.12068E-02	3.34755E-04	5.87737E-03	3.43630E-04	4.37199E-03	3.37688E-04	2.58681E-03	5.26862E-05
1.11633E-02	2.36163E-03	5.88030E-03	4.16317E-04	4.37358E-03	3.88259E-04	2.75479E-03	5.60031E-05
1.11627E-02	2.32079E-03	5.93177E-03	3.78232E-04	4.41396E-03	4.23643E-04	2.88160E-03	6.00503E-05
1.14683E-02	2.42424E-03	5.98831E-03	4.62252E-04	4.45472E-03	4.62252E-04	3.04140E-03	6.43900E-05
1.22130E-02	2.57686E-03	6.04360E-03	5.04380E-04	4.49585E-03	5.04380E-04	3.35768E-03	7.27526E-05
1.28903E-02	2.76309E-03	6.15433E-03	5.50347E-04	4.57823E-03	5.50347E-04	3.54379E-03	7.73328E-05
1.36051E-02	2.96277E-03	6.21116E-03	6.00503E-04	4.66200E-03	5.95289E-04	3.74031E-03	8.29215E-05
1.43593E-02	3.14929E-03	6.38178E-03	6.49541E-04	4.70505E-03	6.49541E-04	3.94773E-03	8.89140E-05
1.51555E-02	3.37688E-03	6.49915E-03	7.27526E-04	4.83440E-03	7.08737E-04	4.16664E-03	9.53395E-05
1.59960E-02	3.62092E-03	6.67783E-03	7.93830E-04	4.96720E-03	7.66613E-04	4.39770E-03	1.02229E-04
1.70347E-02	3.84887E-03	6.86126E-03	8.58655E-04	5.10376E-03	8.36479E-04	4.64157E-03	1.09617E-04
1.79793E-02	4.12702E-03	7.04989E-03	9.36909E-04	5.29118E-03	9.04786E-04	4.94308E-03	1.17539E-04
1.89763E-02	4.42527E-03	7.30878E-03	1.01342E-03	5.43665E-03	9.87244E-04	5.21720E-03	1.26033E-04
2.00287E-02	4.74507E-03	7.50955E-03	1.09617E-03	5.58599E-03	1.06786E-03	5.50639E-03	1.33968E-04
2.11388E-02	5.04380E-03	7.78549E-03	1.19607E-03	5.73944E-03	1.15506E-03	5.81174E-03	1.43649E-04
2.25120E-02	5.40830E-03	7.99935E-03	1.29375E-03	5.95020E-03	1.24939E-03	6.07928E-03	1.54030E-04
2.37598E-02	5.74878E-03	8.36778E-03	1.39939E-03	6.16884E-03	1.36325E-03	6.41626E-03	1.63727E-04
2.50774E-02	6.16423E-03	8.75319E-03	1.51367E-03	6.39537E-03	1.47458E-03	6.83305E-03	1.75560E-04
2.64675E-02	6.55231E-03	9.07441E-03	1.62306E-03	6.63022E-03	1.59499E-03	7.14760E-03	1.88247E-04
2.81868E-02	7.02582E-03	9.49236E-03	1.75560E-03	6.93560E-03	1.72524E-03	7.54397E-03	2.01851E-04
2.97492E-02	7.46814E-03	9.92956E-03	1.89896E-03	7.19029E-03	1.86612E-03	7.96231E-03	2.16438E-04
3.13989E-02	8.00784E-03	1.03867E-02	2.03619E-03	7.45433E-03	2.01851E-03	8.32866E-03	2.30064E-04
3.31401E-02	8.58655E-03	1.08651E-02	2.20247E-03	7.79766E-03	2.18334E-03	8.86968E-03	2.46690E-04
3.49770E-02	9.12712E-03			8.15680E-03	2.36163E-03	9.36133E-03	2.62221E-04
3.72483E-02	9.70172E-03			8.53230E-03	2.53230E-03	9.88045E-03	2.81171E-04
3.96670E-02	1.03125E-02			8.92528E-03	2.73909E-03	1.04284E-02	3.01490E-04
4.18667E-02	1.10578E-02			9.33614E-03	2.93704E-03	1.09084E-02	3.23278E-04
4.45843E-02	1.16518E-02			9.76615E-03	3.17688E-03	1.14111E-02	3.52740E-04
4.74793E-02	1.23854E-02			1.03077E-02	3.40646E-03	1.20428E-02	3.65264E-04
5.05624E-02	1.31651E-02			1.07825E-02	3.68463E-03	1.27103E-02	3.88259E-04
5.38456E-02	1.39939E-02			1.13804E-02	3.95091E-03	1.34155E-02	4.19964E-04
5.73421E-02	1.48749E-02			1.20115E-02	4.23643E-03	1.41591E-02	4.46403E-04
6.16141E-02	1.56741E-02			1.25644E-02	4.54259E-03	1.49443E-02	4.78664E-04
6.56150E-02	1.66609E-02			1.32609E-02	4.82857E-03	1.57730E-02	5.13256E-04
7.05018E-02	1.74035E-02			1.39966E-02	5.22287E-03	1.67972E-02	5.45568E-04
7.57542E-02	1.83385E-02			1.47724E-02	5.55168E-03	1.77283E-02	5.79914E-04
8.21290E-02	1.91559E-02			1.57320E-02	5.95289E-03	1.88799E-02	6.21823E-04
8.82437E-02	1.98360E-02			1.66040E-02	6.32765E-03	1.99264E-02	6.60971E-04
9.56696E-02	2.07202E-02			1.76822E-02	6.72602E-03	2.12204E-02	7.02582E-04
1.03718E-01	2.14559E-02			1.88304E-02	7.14946E-03	2.25983E-02	7.46814E-04
1.12441E-01	2.20247E-02			2.00532E-02	7.59956E-03	2.40657E-02	7.93830E-04
1.22995E-01	2.26086E-02			2.13553E-02	8.07799E-03	2.56284E-02	8.43806E-04
1.33340E-01	2.32079E-02			2.27420E-02	8.58655E-03	2.72926E-02	8.96929E-04
1.45852E-01	2.36163E-02			2.44368E-02	9.12712E-03	2.90642E-02	9.45116E-04
1.58108E-01	2.36163E-02			2.57914E-02	9.70172E-03	3.09507E-02	9.95892E-04
1.72941E-01	2.38232E-02			2.74661E-02	1.03125E-02	3.32566E-02	1.04940E-03
1.89162E-01	2.38232E-02			2.95124E-02	1.08665E-02	3.57350E-02	1.11546E-03
				3.14280E-02	1.14503E-02	3.80537E-02	1.16518E-03
				3.37694E-02	1.20655E-02	4.08888E-02	1.22778E-03
				3.59623E-02	1.28251E-02	4.39350E-02	1.29375E-03
				3.86415E-02	1.35141E-02	4.76311E-02	1.33968E-03
				4.15193E-02	1.41165E-02	5.11785E-02	1.39939E-03
				4.46135E-02	1.50052E-02	5.54853E-02	1.46177E-03
				4.79362E-02	1.56741E-02	6.01531E-02	1.51367E-03
				5.15075E-02	1.65162E-02	6.52137E-02	1.56741E-03
				5.53448E-02	1.74035E-02	7.06999E-02	1.62306E-03
				6.00022E-02	1.81793E-02	7.73362E-02	1.66609E-03
				6.44724E-02	1.91559E-02	8.38405E-02	1.71026E-03
				6.92740E-02	2.00098E-02	9.08917E-02	1.75560E-03
				7.51036E-02	2.09017E-02	9.94211E-02	1.78649E-03
				8.14237E-02	2.18334E-02	1.07783E-01	1.83385E-03
				8.82737E-02	2.26086E-02	1.17894E-01	1.84992E-03
				9.91985E-02	2.38232E-02	1.27807E-01	1.88247E-03
						1.39797E-01	1.89896E-03
						1.51544E-01	1.89896E-03
						1.65758E-01	1.89896E-03
						1.81304E-01	1.89896E-03